Laboratory Study of Angular Momentum Transport in a Rotating Shear Flow

Ethan Schartman

A DISSERTATION

PRESENTED TO THE FACULTY

OF PRINCETON UNIVERSITY

IN CANDIDACY FOR THE DEGREE

OF DOCTOR OF PHILOSOPHY

RECOMMENDED FOR ACCEPTANCE

BY THE DEPARTMENT OF

ASTROPHYSICAL SCIENCES

APRIL 2008

Abstract

The MagnetoRotational Instability (MRI) is widely accepted to be responsible for the angular momentum transport in accretion disks which power some of the most luminous objects in the universe. Conditions for instability to the MRI in ideal MHD are: 1) an angular velocity which decreases with radius and 2) a weak ambient magnetic field which allows the exchange of momentum between radially-separated fluid elements. The MRI has not been conclusively detected in the laboratory. Subcritical Hydrodynamic Instabilities have also received renewed interest for application to cool circumstellar disks which may be too poorly ionized to generate the MRI. Reports of purely hydrodynamic turbulence in subcritical flows lack transport measurements to support the hypothesis that angular velocity shear undergoes a spontaneous transition. A small aspect-ratio, wide gap circular-Couette experiment capable of operation at Reynolds number in excess of 10^6 is constructed to investigate these two mechanisms of angular momentum transport. The apparatus consists of two concentric co-rotating cylinders. To minimize the effect of the cylinder end caps, they are divided into nested differentially rotatable rings. Water and a water-glycerol mix are used as working fluids to study angular momentum transport in quasi-Keplerian flows and its scaling with Reynolds number. When the end rings speeds are optimized, large-scale advective transport due to the vertical boundaries is eliminated. The resulting flow is an excellent approximation to the ideal circular-Couette profile. Measurement of the $r - \phi$ component of the Reynolds stress using Laser Doppler Velocimetry shows no indication of a subcritical instability. Pure hydrodynamic turbulence is an unlikely mechanism to transport angular momentum in accretion disks.

Acknowledgements

and Professor Jeremy Goodman.

This work is dedicated to my first teachers, my parents: David and Laura.

Contents

List of Figures

vii

Chapter 1

Introduction

1.1   Accretion Disks

The angular momentum of gravitationally-interacting matter forms a centrifugal barrier to the infall of that matter on to its center of mass. For gaseous matter this barrier is believed to give rise to a gravitationally-bound disk structure. If the gas continues to evolve by radiating its angular momentum and falling on to the center of mass, the system is called an *accretion disk*. The accretion disk is a central element to theories of star formation, interacting binaries, and Active Galactic Nuclei (AGN). In star formation, the accretion disk is an intermediate stage between the initial condensation of a diffuse cloud and a fully evolved solar system such as our own, see Figure: 1.1. In interacting binaries the transfer of matter from one object to the other is governed by the rate of infall from the accretion disk which is invariably formed. The disk is therefore dynamically important to systems such as Cataclysmic Variables, Type I supernovae and the x-ray luminosity of Black Holes.

When the mass of an accretion disk is much less than that of the central object
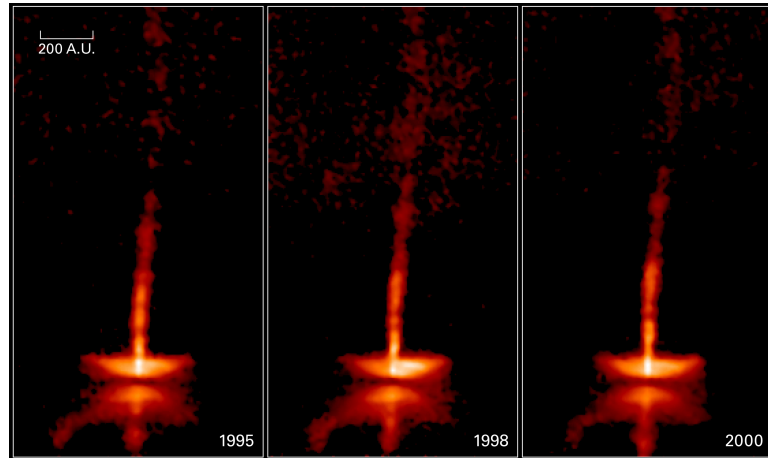
Figure 1.1: Hubble Space Telescope (WFPC2) image of the protostellar disk and jet of Herbig Haro 30. A new star is concealed by the accretion disk from which it was formed. The disk is the dark band, light from the star is scattered by gas above and below the plane of the disk. Photo credit: NASA and A. Watson (Instituto de Astronomía, UNAM, Mexico)
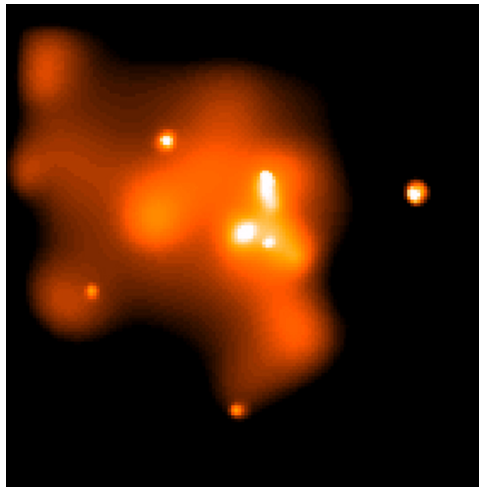
Figure 1.2: Chandra ACIS X-ray image of the disk surrounding the supermassive black hole, Sag A*, at the center of the Milky Way. Sag A* is the largest circular white spot near the image center. The frame is 10 light years on a side. Photo credit: NASA/MIT/PSU

the effects of self-gravity can be neglected and radial pressure gradients are non-existent. The orbital motion of the components of the disk is then entirely due to the gravitational potential of the central object. The angular velocity of the components follow the Keplerian rotation profile:

$$\Omega \propto r^{-3/2}, \tag{1.1}$$

and the disk is *Keplerian*. If the disk makes contact with the accreting object a boundary layer which does not follow the Keplerian profile may form [Lynden-Bell and Pringle, 1974]. This situation occurs in certain circumstellar disks and un-magnetized neutron stars.

The orbital speeds of a Keplerian disk are supersonic $R\Omega(R) \gg c_s$, where R is the radius and c_s is the sound speed. Hydrostatic equilibrium[Balbus and Hawley, 1998] yields a vertical (parallel to the rotation axis) scale height for the disk:

$$H = \frac{c_s}{\Omega}. \tag{1.2}$$

Therefore the disk is thin.

Abbreviated review of angular momentum transport

Accretion disks are transient structures. Disk lifetimes range from 10^8 years for AGNs to 10^5 years for star formation[Lin and Papaloizou, 1996]. The time between events in Cataclysmic Variables may be of order one week. The dissipation of angular momentum causes the orbits of disk components to acquire a spiral nature. This discussion of the accretion process uses cylindrical coordinates (r, ϕ, z) and follows Shakura and Sunyaev[Shakura and Sunyaev, 1973]. In steady accretion, the mass passing through a radius, r, of the disk is:

$$\dot{M} = 2\pi\Sigma r v_r = constant, \tag{1.3}$$

where v_r is an average radial velocity ($v_r \ll r\Omega$) and $\Sigma = \int \rho dz$ is the vertically-integrated density of the disk.

The torque on infalling particles is:

$$\Sigma \frac{d(\Omega r^2)}{dt} = -\Sigma v_r \frac{\partial(\Omega r^2)}{\partial r} = -\frac{1}{r}\frac{\partial(r^2 W_{r\phi})}{\partial r}, \tag{1.4}$$

where d/dt is the convective derivative and $W_{r\phi} \equiv \langle u_r u_\phi - u_{A,r} u_{A,\phi} \rangle$ is the vertically-integrated stress tensor containing both hydrodynamic and MHD stress. The MHD stress has been written in terms of the Alfén speed, $u_A^2 = B^2/4\pi\rho$.

Using the constancy of $\dot{M}$ and $v_r < 0$, integration of Equation 1.4 gives:

$$\dot{M}\Omega r^2 = -2\pi r^2 W_{r\phi} + constant. \tag{1.5}$$

Defining, r_i, as the inner radius of the disk where $W_{r\phi} = 0$ we determine the constant of integration. Finally, using the Keplerian profile, Equation: 1.1 we arrive at:

$$\dot{M}\Omega \left(1 - \sqrt{\frac{r_i}{r}}\right) = 2\pi W_{r\phi}. \tag{1.6}$$

All but a fraction ($\sim \sqrt{r_i/r_o}$) of the initial angular momentum of a particle is radiated before it reaches the inner edge of the disk (the outer edge of the accretion disk is r_o).

The need for a turbulent stress

Laminar particulate viscosity can be quickly eliminated as the source of $W_{r\phi}$. Consider the viscous timescale $\tau_{visc} \sim L^2/\nu$ where L is a characteristic size and ν is the kinematic viscosity. For $\nu \sim 10^5 cm^2/s$ and $L \sim 10^{10} cm$ [Balbus, 2003] the timescale is about 3×10^7 which is orders of magnitude too great to explain the variability seen in some interacting binary systems.

Accretion disks feature a positive radial gradient of angular momentum and are therefore stable to Rayleigh's centrifugal instability.

Correlated fluctuations are required to transport the angular momentum, but finding an instability to produce them remained elusive for more than two decades. Accretion disks featuring large degrees of ionization and magnetic fields are pervasive in astrophysics, therefore a turbulent magnetic field may produce the required correlations. Also, terrestrial experience is that high Reynolds number shear flow undergoes a non-linear turbulent transition. But no satisfactory mechanism was known. Therefore determination of $W_{r\phi}$ proceeded on phenomenological grounds, wrapping the details of the turbulence into a dimensionless parameter, α.

Shakura and Sunyaev [Shakura and Sunyaev, 1973] argued that the magnitude of turbulent velocities is bounded by the sound speed, c_s. Velocities in excess of the sound speed would develop shocks and rapidly dissipate to subsonic speeds. Therefore, the turbulent stress should scale as:

$$W_{r\phi} = \alpha \Sigma c_s^2, \tag{1.7}$$

where $\alpha \leq 1$. Hueso and Guillot[Hueso and Guillot, 2005] estimate that $10^{-4} \leq \alpha \leq 0.1$ based on observations of protoplanetary systems.

Subsonic fluctuations also imply that the turbulence is largely incompressible. Hersant *et al* [Hersant et al., 2005] provides estimates of the Mach number for observed circumstellar disks and finds $Ma < 0.1$ Accretion disks are are highly ionized, except possibly for the quiescent phase of CVs or certain protostellar disks.

The α model is sometimes also arrived at by an "eddy viscosity" argument[Balbus and Hawley, 1998] which gives $\nu_T = \alpha c_s H$, where H is the scale-height of the disk and corresponds to the size of the largest eddy which will "fit" within the disk at some radius R, where $H \ll R$. Using a turbulent viscosity, ν_T,

the closure relation[Speziale, 1991] is:

$$W_{r\phi} = -\nu_T r \frac{\partial \Omega}{\partial r}. \tag{1.8}$$

By far the most promising candidate instability is the MagnetoRotational Instability (MRI) in which hydrodynamically stable displacements are destabilized by the presence of a weak ambient magnetic field. Other instabilities have been studied but none have demonstrated a comparable capacity to generate the correlated fluctuations required of outward angular momentum transport. Some of these mechanisms include the Papaloizou-Pringle instability, hydromagnetic wind, stratorotational instability, and Subcritical Hydrodynamic Instability. Recent work by Richard and Zahn [Richard and Zahn, 1999] and Richard [Richard, 2001] renewed interest in Subcritical Hydrodynamic Instability for application to cold protoplanetary disks which may be too poorly ionized for the MRI.

1.2   MagnetoRotational Instability

The stability of circular-Couette flow of conducting fluid in the presence of a magnetic field was first investigated by Velikhov [Velikhov, 1959] and Chandrasekhar [Chandrasekhar, 1960]. Its potential relevance to astrophysics was not appreciated until the work of Balbus and Hawley[Balbus and Hawley, 1991]. Since the work of Balbus and Hawley the MagnetoRotational Instability (MRI) has been the subject of numerous analytical and numerical investigations, Reviews of that work can be found in Balbus and Hawley [Balbus and Hawley, 1998] and Balbus [Balbus, 2003]. Simulations of Keplerian disks show that the turbulent stress produced by the MRI is consistent with the observational requirements of α models (Equation: 1.7). It is now widely believed to be the most important source of angular momentum transport in accretion disks.

The MRI is a powerful local, linear instability. The conditions for instability in the ideal MHD limit are simply that angular velocity be a decreasing function of radius and that a sufficiently weak magnetic field be present. To illustrate the instability consider an inviscid, perfectly conducting plasma in orbit around a central mass, Figure: 1.3. Angular momentum is an increasing function of radius, whereas angular velocity is decreasing. By the *frozen flux* theorem [Freidberg, 1987] two fluid elements which are threaded by a magnetic field line at any time will remain threaded by the same field line for all times. If the fluid elements are initially at the same radius but become radially displaced from each other, the field line must "stretch" to accommodate the motion. The Maxwell stress in the magnetic field then acts like a spring connecting the elements. As the inward-displaced element acquires a larger angular velocity it is decelerated by the stretching magnetic field. This deceleration causes it to lose angular momentum and hence be fall further inward, reinforcing the initial displacement. In contrast, the outward-displaced element will be accelerated by the tension in the magnetic field. The acceleration will increase its angular momentum causing it to move to larger radii and smaller angular velocity.

Consider a rotating shear flow in cylindrical coordinates, (r, ϕ, z). If an axial equilibrium magnetic field $\mathbf{B} = \mathbf{B_0}\hat{\mathbf{z}}$ is present and the mean flow is described by $v_r = v_z = 0, v_\phi = r\Omega(r)$, then linearization of the ideal MHD equations leads to the dispersion relation for the MRI [Balbus and Hawley, 1998]:

$$\omega^4 - \omega^2 \left[\kappa^2 + 2\left(\mathbf{k} \cdot \mathbf{u_A}\right)^2 \right] + \left(\mathbf{k} \cdot \mathbf{u_A}\right)^2 \left(\left(\mathbf{k} \cdot \mathbf{u_A}\right)^2 - 2q\Omega^2 \right) = 0, \qquad (1.9)$$

where the perturbations take the form $exp(-i\omega t + i\mathbf{k} \cdot \mathbf{r})$, $q \equiv -\partial \ln \Omega / \partial \ln r$ is the local exponent of the mean angular velocity, and the epicyclic frequency is $\kappa \equiv r^{-3}\partial l^2/\partial r = 2\Omega^2(2 - q)$. The Rayleigh criterion for centrifugal instability is $\kappa^2 < 0$, or $q > 2$.
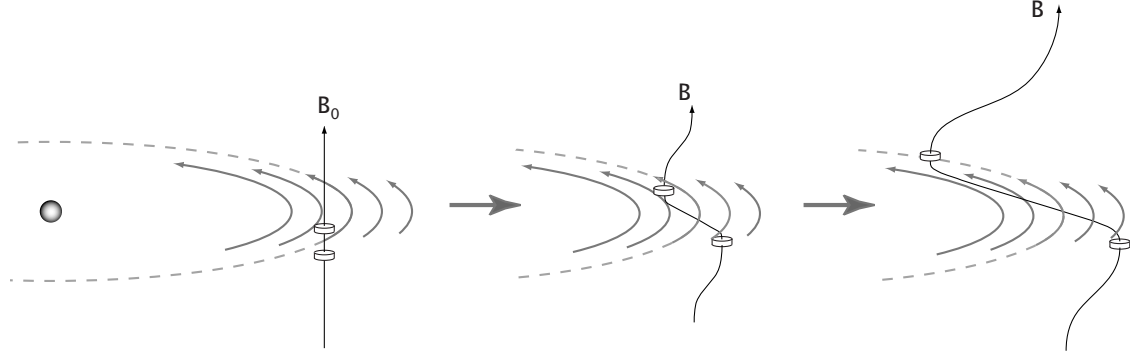
Figure 1.3: A qualitative picture of the mechanism of MRI. Angular momentum is transported "up" a positive gradient by the stretching of a magnetic field line threading fluid elements which are radially displaced from their equilibrium.

This dispersion relation yields the following properties of the MRI:

- For $q > 0$, the presence of an arbitrarily weak magnetic field yields unstable solutions which persist in the limit $B_0 \to 0$: no magnetic field is too weak to be dynamically unimportant.

- The fastest growth rate for any B_0 is:

$$|\omega_{max}| = \left|\frac{1}{2}q\Omega\right|$$

- The perturbations generated by the MRI must remain confined to the disk which implies that there is a minimum k parallel to B_0. There is a maximum magnetic field above which the instability is suppressed:

$$(\mathbf{k} \cdot \mathbf{u_A})^2 > 2q\Omega^2$$

- In the linear regime the instability is incompressible.

The ideal MHD version of the MRI is an appropriate approximation for the high-temperature accretion disks which form around black holes and other

highly energetic astrophysical systems. For some circumstellar disks, the plasma may be too poorly ionized to employ the perfect conductivity approximation. When resistivity and viscosity are taken into account[Sano and Miyama, 1999], instability is no longer produced in the $B_0 \to 0$ limit. Resistivity may allow the magnetic field to diffuse back to its equilibrium position before significant growth occurs. Similarly, viscous effects may damp the perturbations.

1.3 Subcritical Hydrodynamic Instability

Stability to linear perturbations does not guarantee the absence of turbulence in shear flow. Laminar pipe flow, for example, is linearly stable to small perturbations for all Reynolds numbers [Eckhardt et al., 2007]. However, careful experimental precautions must be exercised to achieve a laminar pipe flow at $Re \sim 10^4$. At higher Reynolds numbers, residual fluctuations in the flow will always trigger a transition to turbulence. In contrast, for deliberately large perturbations, the turbulent transition can be triggered for $Re \sim 10^3$. The coexistence of laminar and turbulent regimes is a hallmark of a *sub-critical* (also known as *bypass* or *finite-amplitude*) transition to instability. Another characteristic of sub-critical turbulence is intermittency: a point in the flow will exhibit laminar motion until a sufficiently large perturbation triggers turbulence which then subsides or is swept away from the observation point.
In addition to pipe flow, sub-critical transition is observed in plane Poiseuille and plane Couette flow. A transition is also observed in cyclonic circular-Couette flow where the inner cylinder is at rest. Based on this it has been conjectured that a sufficiently large gradient in angular velocity will produce a sub-critical transition.
Zeldovich [Zeldovich, 1981] was the first to apply measurements from cyclonic

circular-Couette flow to develop a model for a turbulent viscosity.His analysis did not include the work of Wendt, and does not fit the combined data of Taylor and Wendt. Richard and Zahn[Richard and Zahn, 1999] use the results of both Wendt and Taylor to develop their closure. Longaretti [Longaretti, 2002] derives an eddy viscosity from a phenomenological argument which arrives at a result which differs from that of Richard and Zahn by a factor of 6.

The closure model of Richard and Zahn proceeds from the observations of Taylor and Wendt (see Section: 2.1.2) that a transition to turbulence occurs in laminar cyclonic circular-Couette flow when the Reynolds number exceeds a critical value, Re_c. According to the data of Figure: 2.6, when the ratio of gap width, $d = r_2 - r_1$, to the average radius $\tilde{r}$, $d/\tilde{r} > 1/20$, Re_c increases like $(d/\tilde{r})^2$, therefore they arrive at:

$$Re_c = 6 \times 10^5 \left(\frac{d}{\tilde{r}}\right)^2. \tag{1.10}$$

The turbulent viscosity becomes independent of the gap width and is then determined only by the local shear:

$$\nu_t = \beta r^3 \left|\frac{d\Omega}{dr}\right| \tag{1.11}$$

Hueso and Guillot [Hueso and Guillot, 2005] estimate that to explain protoplanetary rates of accretion $\beta \sim 10^{-5}$.

Richard and Zahn attempt to connect the cyclonic instability of Wendt and Taylor to the quasi-Keplerian regime through a profile measurement made by Wendt [Wendt, 1933] at the Rayleigh criterion for centrifugal instability: $\Omega_1 r_1^2 = \Omega_2 r_2^2$. No torque data was available for flows with both cylinders in rotation, but the profile shows an increase in angular momentum with radius and a flattening of the angular velocity profile from the ideal circular-Couette solution. Using two-component Laser Doppler Velocimetry (see Section: 3.5.1, the angular momentum transport due to Subcritical Hydrodynamic Instability can be directly

measured. To do this, we equate the Reynolds stress (the hydrodynamic component of $W_{r\phi}$) to a viscous flux for which the viscosity follows the prescription of Equation: 1.11:

$$2\pi\rho r^2 \langle v_r' v_\phi' \rangle = -2\pi\rho\nu_t r^3 \frac{\partial\Omega}{\partial r}. \tag{1.12}$$

If the velocity components of the diagnostic are aligned with the radial and azimuthal directions, the left-hand side can be measured directly.

1.4   Need for laboratory experiment

After the rediscovery and astrophysical application of the MagnetoRotational Instability by Balbus and Hawley, much analytic and numerical work has followed. That effort has shown it to be the only instability known to be capable of producing and sustaining the stress required for astrophysically relevant angular momentum transport, see the reviews the reviews by Balbus and Hawley[Balbus and Hawley, 1998] and Balbus [Balbus, 2003]. Unlike many other instabilities of astrophysical importance, such as Kelvin-Helmholtz and Rayleigh-Taylor, the MRI has not been conclusively demonstrated on Earth. Though its existence is not questioned by astrophysicists, production of the MRI in the laboratory would provide a useful verification of the theory. Of greater importance, however, is that a study of the linear growth phase and saturation of the instability would provide much needed physical insights and useful benchmarks against which to compare the codes used to simulate astrophysical systems.

The MRI does not depend on the mechanism by which a flow is maintained. In the ideal MHD limit, Equation 1.9, the instability requires only a radially-decreasing angular velocity and the presence of a weak ambient

magnetic field. Shear flows with the required angular velocity gradients are easily produced by Taylor-Couette experiments in which a fluid is confined between two concentric spinning cylinders. By employing a liquid metal as the working fluid it may be possible for the flow to interact with an applied magnetic field to produce the MRI. Figure: 1.4 outlines such an experiment.
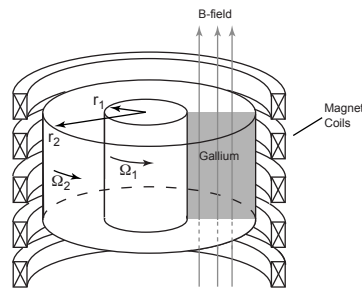
Figure 1.4: A rotating shear flow in a liquid gallium alloy is established between two concentric co-rotating cylinders of radii r_1 and r_2. Appropriate choice of cylinder speeds Ω_1, Ω_2 establishes an angular velocity profile which is linearly stable by the Rayleigh criterion but may become unstable to the MRI in the presence of an applied axial magnetic field. The magnetic field is produced by solenoidal coils which surround the flow.

The volume between the cylinders is filled with a liquid gallium alloy. The inner (outer) cylinder has a radius $r_1(r_2)$ and angular velocity Ω_1 (Ω_2). If the speeds of the cylinders are chosen such that $\Omega_1 > \Omega_2$ and $r_1^2\Omega_1 < r_2^2\Omega_2$, the flow will be linearly hydrodynamically stable, but may be destabilized by the application of a uniform axial magnetic field. Liquid metals are viscous and resistive, and the experimental geometry must have caps at the vertical boundaries. To determine if there is a reasonable expectation that the MRI could be observed in a feasible laboratory experiment, Ji *et al*[Ji et al., 2001] performed a linear stability analysis based the properties of a liquid gallium alloy and an apparatus geometry where the height of the apparatus,$\approx 0.1m$, is comparable to the gap between the cylinders, $r_2 - r_1 \approx 0.1$ m. The results of that analysis showed that an applied

magnetic field of order $1kG$ could produce MRI when the Magnetic Reynolds number satisfies:

$$Re_m \equiv \frac{VL}{\eta} \sim 1, \tag{1.13}$$

where V and L are a characteristic velocity and length of the flow. For the PRINCETON MRI EXPERIMENT , $L = \tilde{r} = (r_2 - r_1)/2$ is the mid-radius of the cylinder gap, and $V = (\Omega_1 - \Omega_2)\tilde{r}^2$. Because the magnetic Prandtl number $P_m = \nu/\eta \sim 10^{-6} \ll 1$, the Reynolds number of the flow must be quite large:

$$Re \equiv \frac{VL}{\nu} \sim 10^6. \tag{1.14}$$

The proposed Reynolds number of the experiment exceeds the estimate by Richard and Zahn of the critical Reynolds number for subcritical hydrodynamic turbulence. Therefore, a laboratory study of the MRI is a *a fortiori* study of subcritical hydrodynamic instability as well.

A wide variety of flow regimes are accessible through the choice of cylinder speeds, these regimes are diagrammed in Figure: 1.5 for co-rotating cylinders. The specific angular momentum is $l = r^2\Omega$. When $\partial\Omega/\partial r > 0$, $\partial l/\partial r > 0$ the flow is linearly stable and said to be *cyclonic*. When the angular velocity is constant $\partial\Omega/\partial r = 0$ no shear is available to drive non-linear hydrodynamic turbulence, nor the MRI and the flow is *solid body*. The flow is *anti-cyclonic* when $\partial\Omega/\partial r < 0$ and is unstable to the ideal MHD version of the MRI. Anti-cyclonic flow can be divided in to two sub-categories. If $\partial l/\partial r > 0$ the flow is hydrodynamically linearly stable. It is this regime that is relevant to Keplerian disks and is therefore known as *quasi-Keplerian* flow. When $\partial l/\partial r < 0$ the flow is linearly unstable by the Rayleigh criterion and is called *centrifugally unstable* flow.

A liquid metal laboratory experiment cannot ever directly access the physics of an accretion disk. For a protoplanetary disk $Re \geq 10^{12}$[Hueso and Guillot, 2005] and the six orders of magnitude separating the Reynolds numbers of laboratory and
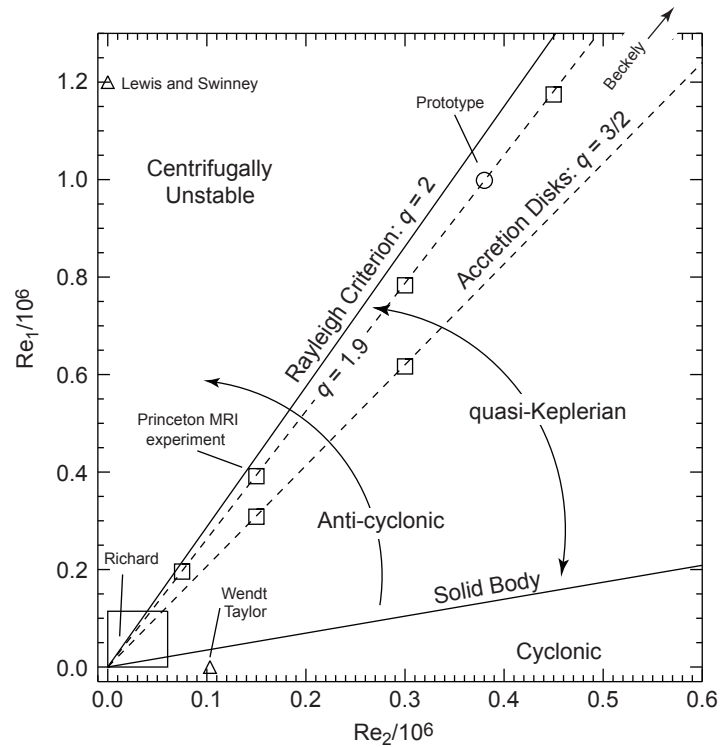
Figure 1.5: Regimes of rotating shear flow accessible to circular-Couette flow between concentric spinning cylinders of radii r_1 and r_2. Axes are Reynolds numbers based on the speed of the cylinders, $Re_{1,2} = \Omega_{1,2}r_{1,2}(r_2 - r_1)/\nu$. Cyclonic flow features radially-increasing gradients of angular momentum and velocity. Solid body rotation is the constant angular velocity state. Anti-cyclonic flow has a radially-decreasing angular velocity. In anti-cyclonic flow the angular momentum may either increase or decrease with radius: quasi-Keplerian refers to the former case and includes the $q = 3/2$ profile of Keplerian accretion disks. When the angular momentum gradient is negative, the anti-cyclonic flow is linearly unstable according to the Rayleigh criterion. Also plotted are Reynolds number for select experiments discussed in Section: 2.1.2. *Adapted from Figure: 2 of [Ji et al., 2006].*

astrophysical systems cannot be significantly reduced. Accretion disks do not have the well defined boundaries of laboratory experiments. Furthermore, the Keplerian angular velocity profile is supported by gravity whereas lab flows are driven by viscous or perhaps Lorentz forces. Therefore the effect of saturation will have very different signatures: in a disk matter is transported radially inward leaving the mean angular velocity unchanged while in the laboratory the angular velocity profile will be modified while the mass is conserved. Finally, small scale magnetic fields are damped by the low conductivity of liquid metals. At a $Re_m \sim 1$, this restricts the MRI induced fields to approximately the size of the experiment. In contrast, the magnetic Reynolds numbers and conductivities of accretion disks are so large that magnetic fields are important at all scales. In contrast, simulations have no difficulty modeling gravitationally supported flow, nor large conductivities. While modeling turbulence at high Reynolds number is beyond the capability of the codes, powerful insight in to the physics of accretion disks can be achieved through the complimentary properties of experiment and simulation. To take advantage of the collaborative possibilities with numerical work, development of simulations of the PRINCETON MRI EXPERIMENT has occurred alongside the development and operation of the experiment. The thesis by Liu [Liu, 2007] details axisymmetric simulations of the MRI search with the PRINCETON MRI EXPERIMENT . Collaboration with researchers led by Fausto Cattaneo at the University of Chicago is also ongoing.

1.5   Outline of the present work

The remaining chapters are organized as follows.

Chapter: 2 provides a brief derivation of the Couette profile developed between concentric spinning cylinders of infinite vertical extent. Non-ideal effects due to

the presence of vertical boundaries are discussed. These effects are the *Ekman circulation* and formation of Stewartson layers. Ekman circulation is a poloidal circulation cell driven by the no-slip conditions present at the cylinder ends. The circulation is an advective angular momentum transport mechanism which may cause significant deviation from the ideal mean azimuthal velocity profile. In rapidly rotating flows velocity discontinuities at the end caps may propagate vertically in to the fluid bulk giving rise to a Stewartson layer. The Stewartson layer may be subject to non-axisymmetric instability. Previous experiments from the cyclonic, quasi-Keplerian and centrifugally unstable flow regimes are reviewed. The experiments include work related to Sub-critical Hydrodynamic Instability: Taylor and Wendt in the cyclonic regime and Richard in the quasi-Keplerian regime. A brief summary of analytic and numerical investigations of magnetized circular-Couette flow follows. Selected experiments are briefly discussed: the stabilization of centrifugally unstable flows by large magnetic fields and the report of MagnetoRotational Instability in a spherical-Couette flow.

Chapter: 3 provides a thorough introduction to the mechanical design and operation of the Princeton MRI experiment. To achieve the Reynolds number required of a search for the MagnetoRotational Instability the maximum speed of the inner cylinder (radius of $r_1 = 0.076m$) is $4000rpm$ and that of the outer cylinder (radius $r_2 = 0.203m$) is $533rpm$. At these speeds the pressure generated by rotation of the Gallium alloy is ~ 25 atmospheres. In addition the end caps of the experiment are segmented to allow differential rotation, thereby reducing the Ekman circulation. The unique mechanical challenges required to achieve successful operation are described. During hydrodynamic experiments Laser Doppler Velocimetry is used to obtain a non-invasive diagnostic of flow velocity and fluctuations. The principle of operation of Laser Doppler Velocimetry is

reviewed in order to understand how the mechanical design decisions of the experimental apparatus impact the calibration and precision of the technique. Next, a review of the magnet system which will be used to provide the excitation field during MHD experiments and the magnetic pick-up coils which will be used for the initial diagnostics when the experiment is filled with the Gallium alloy. The electrically noisy environment created by the drive motors and magnet bus current required the development of a custom amplifier-filter array for the pick-up coil signals. The design and performance of that amplifier will be briefly reviewed.

Hydrodynamic experiments with water and a water-glycerol mix are presented in Chapter: 4. Evaluation of the split-ring design is presented, included mean profile control and scaling with Reynolds number. Detailed measurement of the local angular velocity exponent indicates that advective transport driven by large-scale Ekman circulation may be eliminated by choice of end ring speeds. Residual vertical transport allows the gradient of angular velocity profile to exceed the Rayleigh criterion without exciting centrifugal instability. At Reynolds numbers above the transition threshold proposed by Richard and Zahn we use two-component Laser Doppler Velocimetry to directly measure the $r - \phi$ component of the stress tensor. We find no indication of a sub-critical transition to turbulence, nor the predicted levels of transport.

Chapter: 5 contains a summary and discussion. Technical issues associated with the realization of a high-Reynolds number, liquid metal compatible circular-Couette experiment are reviewed. Novel reduction of vertical transport of angular momentum is achieved through disruption of Ekman circulation. In contrast to previous work we found no evidence of sub-critical hydrodynamic instability. The implication for angular momentum transport in accretion disks is discussed. Based on terrestrial experience with the scaling of turbulent friction in

pipe flow we argue that a purely hydrodynamic turbulence we provide limits its relevance to astrophysical systems. Implications for MRI experiments are discussed.

1.5.1 Notation used in this work

The PRINCETON MRI EXPERIMENT has a great deal of mechanical flexibility in the production of a target Reynolds number. We developed an *ad hoc* naming convention to distinguish operational configurations. These names often overlap with names of physical properties we wish to produce in the flow. To avoid confusion the configuration names are presented in a `fixed width` font. For example, the `Ekman` configuration features the end caps of the experiment co-rotating with the outer cylinder in order to produce a profile which is dominated by the advective transport of angular momentum through Ekman circulation.

Chapter 2

Circular-Couette flow

2.1 Circular-Couette Flow (unmagnetized)

The term *circular-Couette flow* describes the flow of an incompressible fluid confined between nested rotating cylinders, see Figure: 2.1. The flow was first investigated by Couette[Couette, 1888] and Mallock[Mallock, 1888] in the late 19th century as a means of measuring the viscosity of liquids. When the outer cylinder rotates at a slower rate than the inner, such that $\partial l/\partial r < 0$, *Taylor-Couette flow* is obtained. Named in honor of G. I. Taylor[Taylor, 1923] who predicted and experimentally confirmed that viscosity delays the onset of Rayleigh's centrifugal instability to finite Reynolds number. For typical Taylor-Couette experiments the Reynolds number at the onset of instability is

$Re_c = (\Omega_1 - \Omega_2)_c(r_2 - r_1)(r_2 + r_1)/2\nu \sim 100$. Taylor-Couette flow has since been demonstrated to be accessible to both detailed theoretical investigation and precise experiment and has therefore become one of the most widely-studied problems in classical fluid dynamics[Tagg, 1994].

For a fluid confined between cylinders of infinite height and without axial gradients, angular momentum is only transported radially. Following the

19
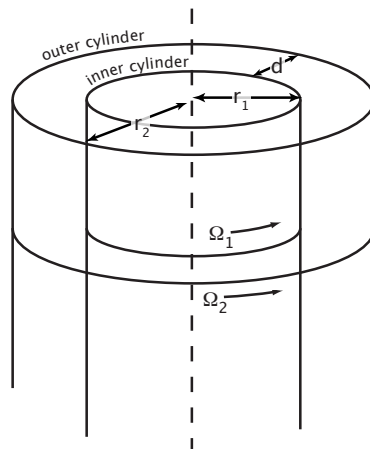
Figure 2.1: A fluid of kinematic viscosity ν, is confined between two infinitely tall cylinders. The cylindrical coordinates are r, ϕ, z. The radius of the inner (outer) cylinder is r_1 (r_2), the gap width is $d = r_2 - r_1$. The rotation speed of the inner (outer) cylinder is Ω_1 (Ω_2), and $\Delta\Omega = \Omega_1 - \Omega_2$. The Reynolds number of the flow is defined as $Re = \Delta\Omega d\tilde{r}/\nu$, where $\tilde{r}$ is some characteristic radius. In this thesis, $\tilde{r} = (r_2 + r_1)/2$. Because Taylor-Couette flow is often studied with a stationary outer cylinder, the Reynolds number is routinely defined as $Re_1 = \Omega_1 r_1 d/\nu$ [Tagg, 1994]. For physically realizable experiments, the cylinder height is h, and the aspect ratio is $\Gamma = h/d$. *Sketch after Figure: 1 of [Taylor, 1923]*

derivation in [Guyon et al., 2001], in cylindrical geometry with coordinates r,ϕ and z, the constant radial flux of angular momentum is written:

$$\frac{\partial}{\partial r}\left(r^2\sigma_{\phi r}\right) = 0, \tag{2.1}$$

where $\sigma_{\phi r}$ is the r-ϕ component of the viscous stress tensor:

$$\sigma_{\phi r} = \nu\left(\frac{1}{r}\frac{\partial v_r}{\partial r} + \frac{\partial v_\phi}{\partial r} - \frac{v_\phi}{r}\right). \tag{2.2}$$

The $W_{r\phi}$ of Section: 1.4 represents turbulent stresses due hydrodynamic and MHD instabilities. In the non-magnetized case, $W_{r\phi}$ may be approximated by replacing η in Equation: 2.2 by a turbulent viscosity, η_t, see the discussion of subcritical hydrodynamic instability in Section: 1.3. Writing $v_\phi = r\Omega(r)$, with the condition that $v_r \equiv 0$, a solution of Equation:2.1 in powers of r gives:

$$\Omega(r) = a + \frac{b}{r^2}. \tag{2.3}$$

In terms of the rotation speeds of the cylinders, $\Omega_{1,2}$, non-slip boundary conditions give for the constants a and b:

$$a = \frac{\Omega_2 r_2^2 - \Omega_1 r_1^2}{r_2^2 - r_1^2}, \qquad b = \frac{(\Omega_1 - \Omega_2)\,r_2^2 r_1^2}{r_2^2 - r_1^2}. \tag{2.4}$$

The centrifugal force generated by the fluid's azimuthal velocity is balanced by the pressure gradient:

$$\rho r\Omega^2 = \nabla P = \frac{\partial P}{\partial r} \tag{2.5}$$

2.1.1 Finite height effects

All physically realizable circular-Couette experiments have a finite cylinder height, h. Rigid plates typically form the vertical boundaries, though Wendt did use a free surface at the upper end of his experiment. The rigid plates impose non-slip boundary conditions on the fluid adjoining them. The influence of the boundaries is never completely negligible even for very large aspect ratios ($\Gamma > 100$ in Taylor's work[Taylor, 1936], see also [Tagg, 1994]).

Ekman circulation

At the interface of the bulk flow and viscous layer which rigidly rotates with the cylinder end cap, the bulk flow is decelerated by the boundary while the pressure remains vertically constant, see Figure: 2.2. This force imbalance is compensated by a radial inflow. At the inner cylinder the radial flow becomes axial and is accelerated as it spirals up the cylinder. In large aspect ratio devices, the Ekman layer may detach from the inner cylinder before reaching the midplane [Coles, 2006]. In small aspect ratio devices such as our current and prototype experiments, the Ekman layer from each end cap is expected to reach the midplane and then form a radial jet. Note that when the end caps rotate faster than the bulk, the end cap flow is radially outward.

A derivation of the laminar Ekman layer can be found in the appendix of [Kageyama et al., 2004], the results are quoted here. In the limit of small departures from solidbody rotation the thickness of the Ekman layer is:

$$\delta_{Ekman} = \sqrt{\frac{\nu}{\Omega}}. \tag{2.6}$$

For the high Reynolds number shear flows investigated here and in the prototype experiment, the departure from solidbody rotation is not "small". Therefore, Kageyama *et al* develop an Ekman layer thickness based upon small departures from circular-Couette flow:

$$\delta_{Ekman} = \sqrt{\frac{2\nu}{\bar{\kappa}}}, \qquad \bar{\kappa} = 2\left(\frac{r_2^4\Omega_2^2 - r_1^4\Omega_1^2}{r_2^4 - r_1^4}\right), \tag{2.7}$$

where $\bar{\kappa}$ is a *characteristic* value for the epicyclic frequency.

The torque exerted by the two end caps on the bulk flow is:

$$\Gamma = 4\pi\rho \int_{r_1}^{r_2} \kappa\delta_{Ekman}r^3 \left(\Omega_{cap} - \Omega_{bulk}\right) dr. \tag{2.8}$$
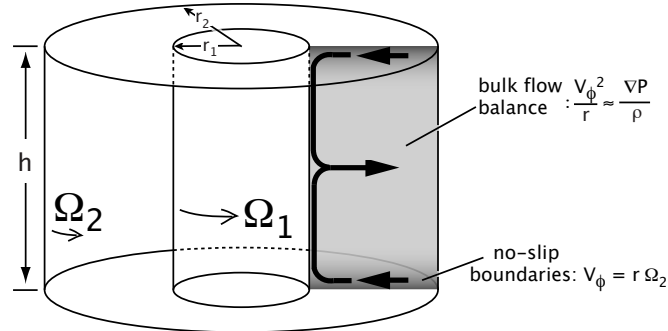
Figure 2.2: Ekman circulation driven by end caps co-rotating with the outer cylinder. As a fluid element in the bulk flow adjacent to the end cap is decelerated by the viscous boundary layer. Because the pressure remains approximately constant across the boundary layer, the element experiences a radially-inward force. Ultimately the drag of the end cap establishes a poloidal Ekman cell which advects angular momentum out of the bulk flow.

Stewartson layers

The Taylor-Proudman theorem[Greenspan, 1968] is arrived at by considering the Navier-Stokes equations in a frame rotating about the z-axis at a frequency Ω:

$$\frac{\partial \mathbf{v}}{\partial t} + \mathbf{v} \cdot \nabla \mathbf{v} + 2\boldsymbol{\Omega}\hat{\mathbf{z}} \times \mathbf{v} = -\nabla \frac{\mathbf{P}}{\rho} + \nu \nabla^2 \mathbf{v}. \tag{2.9}$$

If the Coriolis force dominates the advective terms (the small Rossby-number limit), the advective term can be neglected. Similarly, if viscosity is dominated by the Coriolis force (small Ekman-number limit) the viscous term can be neglected. With these limits, taking the curl of Equation: 2.9 we arrive at the Taylor-Proudman theorem:

$$\frac{\partial}{\partial t} (\nabla \times \mathbf{v}) = 2\Omega \frac{\partial}{\partial z} \mathbf{v}. \tag{2.10}$$

Motions that are slow with respect to Ω become independent of z. Stewartson[Stewartson, 1957] investigated theoretically the motion of a fluid confined inside a rapidly rotating cylinder where co-axial disks nested in the end

caps of the cylinders rotate differentially with respect to the cylinder. In accordance with the Taylor-Proudman theorem, he found that the velocity discontinuity of the boundary propagated vertically in to the bulk flow. This discontinuity is now known as a *Stewartson layer*. At large differential rotation the Stewartson layer becomes subject to non-axisymmetric instability [Hollerbach, 2003] similar to Kelvin-Helmholtz instability. Stewartson layers have been observed for the co-axial disks mounted in cylinder end caps[Hide and Titman, 1967] and for a disk suspended by a thin rod in the bulk of a fluid contained in a cylinder[Früh and L., 1999].

Hollerbach and Fournier[Hollerbach and Fournier, 2004] predicted that the formation of Stewartson layers in the new apparatus would cause profiles of azimuthal velocity which would be unfavorable for the production of the MagnetoRotational Instability or complicate its observations with Kelvin-Helmholtz instabilities.

2.1.2   Previous hydrodynamic experiments

This section briefly reviews experiments performed in circular-Couette flows which are linearly stable by the Rayleigh criterion. A brief chronology of Taylor-Couette experiments is included. In addition, the work of Lewis and Swinney is also summarized. Their experiments were performed in fully-developed turbulence in high Reynolds number centrifugally unstable flow. Salient parameters of the experiments reviewed are included in Table: 2.1.

Brief history of Taylor-Couette experiments

This short review of work in Taylor-Couette flow follows that of Tagg [Tagg, 1994]. Liquid flow developed between rotating concentric cylinders was first

investigated by Couette [Couette, 1888] and Mallock [Mallock, 1888] as means of measuring viscosity. Rayleigh [Rayleigh, 1916] proved that rotating inviscid fluids are linearly unstable when the angular momentum is a decreasing function of radius. In 1923,Taylor [Taylor, 1923] performed an axisymmetric linear stability analysis for the case in which the viscosity is non-zero. He determined that viscosity delays the onset of centrifugal instability and that instability proceeds through super-critical transitions in the flow which produce *Taylor vortices*. He then experimentally confirmed the existence of this instability.

The transition to turbulence in Taylor-Couette flow proceeds through a series of steady-state bifurcations as eigenmodes become destabilized with changes in cylinder speeds. The bifurcations produce easily visualized changes to the flow as vortices are added or subtracted or as azimuthal mode number increases or decreases. The progression to the "fully-developed" turbulent state proceeds as the discrete spectrum of axial and azimuthal wave numbers changes to a continuous one by broadening of the spectral lines. The process is gradual and reversible as Reynolds number is increased.

Coles [Coles, 2006] performed a detailed study of the transitions between states, finding more than 70 transitions in a speed range up to ten times the Reynolds number of the first transition. An example map of the state transitions observed by Coles is shown in Figure: 2.3, as is a photograph of "wavy vortex" flow. Flow states accessible by fixing the outer cylinder speed and then slowly increasing the inner cylinder speed are diagrammed in Figure: 2.4.

The Taylor-Couette flow provides an important research tool for the study of super critical transition. Quasi-Keplerian and cyclonic flow have been the subject of far less investigation due their linear stability.
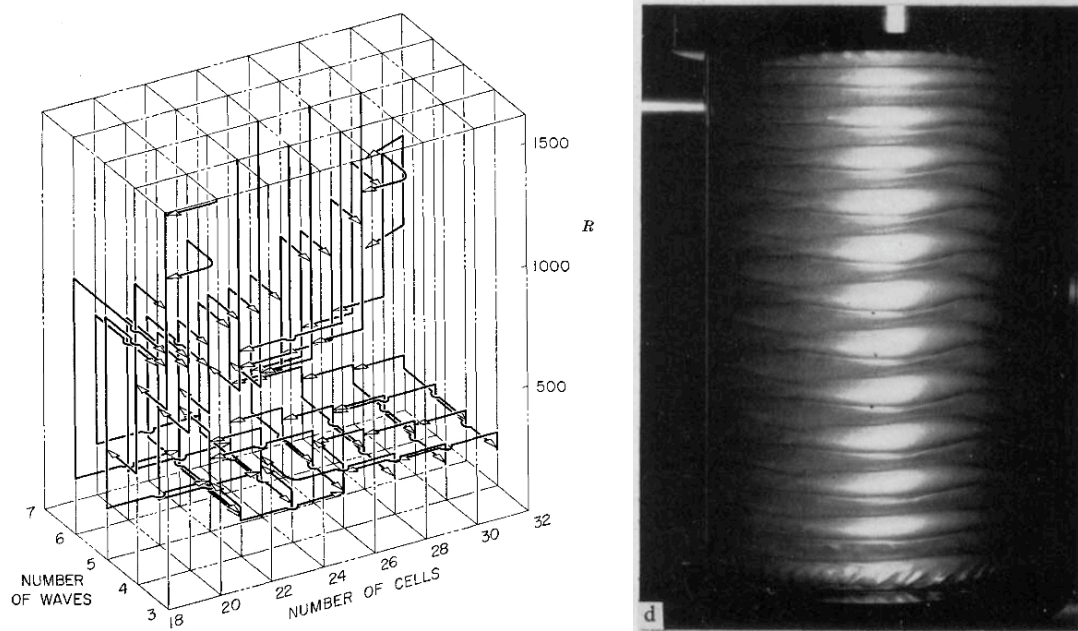
Figure 2.3: Left: Observed transitions for doubly-periodic Coutte flow where the outer cylinder is at rest. "Number of cells" refers to circulation cells in the axial direction, or axial wavenumber. "Number of waves" corresponds to azimuthal mode number. "R" is the Reynolds number. Right: Example of 24-cell, Transition from 5-wave to 4-wave, 24-cell flow. Note presence of Ekman effects are restricted to the one or two cells closest to the end caps. From Coles [Coles, 2006]
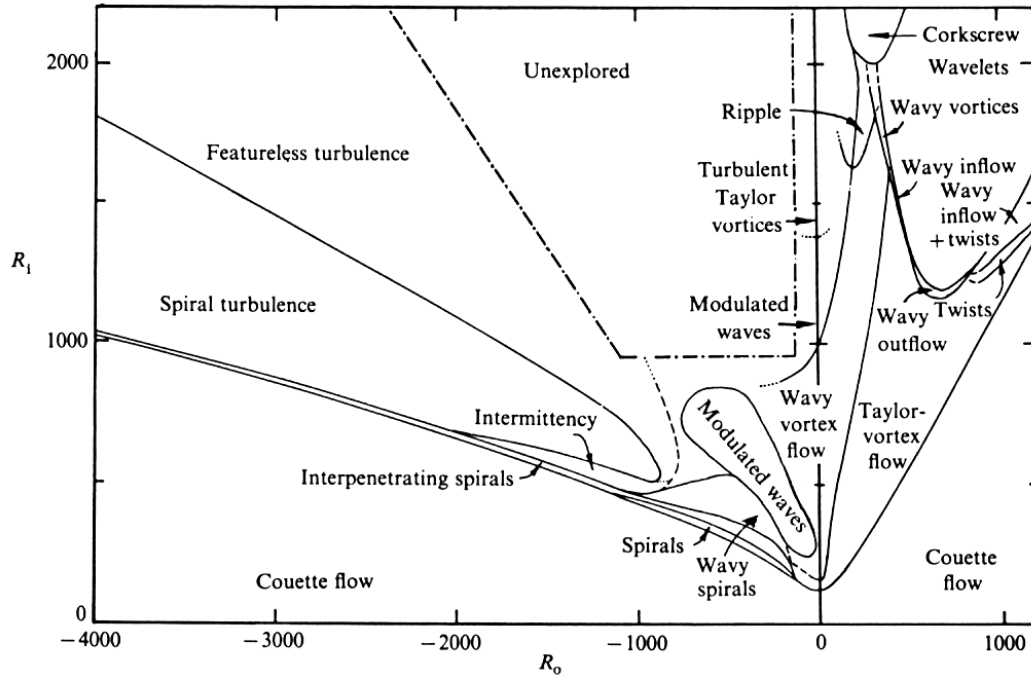
Figure 2.4: Flow states produced in Taylor-Couette flow. From Andereck *et al*[Andereck et al., 1986]

Table 2.1: Parameters of circular-Couette experiments used to investigate turbulent flow. Abbreviations for the *Regimes* are: Cyc: cyclonic, qK: quasi-Keplerian, CU: centrifugally unstable (by Rayleigh's criterion). Quasi-Keplerian and centrifugally unstable flows are subclasses of anti-cyclonic flow. Γ is the aspect ratio and d is the gap width. Some of Coles' work was performed with counter-rotating cylinders which is indicated by the sign of the Re. *N.b.* Beckley defines his Reynolds number using $Re = r_1^2 \Omega_1 / \nu$

Experimenter	Γ	$d(mm)$	$Re_{max} \times 10^4$	Regime
Taylor[1]	770–100	1–9	10	Cyc
Wendt[2]	8.5–42	10–47	10	CU, qK, Cyc
Coles[3]	15	6.3	±0.1	CU
Lewis & Swinney[4]	11.5	61	100	CU
Beckley[5]	2	150	438	qK, Cyc
Richard[6]	25	15	6	qK, Cyc
Prototype[7]	1	111	100	qK

Fully developed turbulence in the centrifugally unstable regime: Lewis and Swinney

A large body of experimental work exists for Taylor-Couette flow, which is not relevant to the problem of angular momentum transport in accretion disks. However, one experiment is summarized here: that of Lewis and Swinney[Lewis and Swinney, 1999]. Their work measures properties of a rotating shear flow in the presence of fully developed turbulence. The turbulence is driven by Rayleigh's centrifugal instability and so is of little use to the study of accretion disks. Prior to the PRINCETON MRI EXPERIMENT , no detailed measurement of transport was made in quasi-Keplerian flow. Therefore the work of Lewis and Swinney provides some useful insights about a saturated state of hydrodynamic turbulence. Furthermore, observations of the MagnetoRotational Instability have been claimed for a Rayleigh-unstable (spherical-Couette) flow and Lewis and Swinney's work is particularly relevant when weighing those claims.

They extend the earlier work of Lathrop *et al* [Lathrop et al., 1992] and Smith and Townsend[Smith and Townsend, 2006] who demonstrated that for a stationary outer cylinder in the range $7.2 \times 10^3 < Re < 1.2 \times 10^5$ the radial profile of the flow is characterized by an inviscid core region bounded by thin boundary layers at the cylinder walls. The outer cylinder is at rest so the global angular momentum gradient must be negative. The negative gradients are confined to these two shear layers. In the inviscid core, the angular momentum slightly increases with radius but is nearly constant: they approximate the flow by $v_\phi r / (r_1^2 \Omega_1) \approx 1/2$, indicating that the bulk flow relaxes to a state close to that of marginal centrifugal stability. However, it appears that marginal stability is approached asymptotically. The increase of angular momentum in the bulk decreases with Re . At $Re \sim 10^4$ the change is 10%, at 10^5 it is 2%. An advective transport that is disrupted at higher

Reynolds number could account for this behavior.

Lewis and Swinney use buoyant particles which migrate to low pressure regions to visualize structures within the flow. They observed stable turbulent Taylor vortices which persist up to the highest Reynolds number examined, though for $Re > 10^5$ they drift axially and their number is not well-defined.
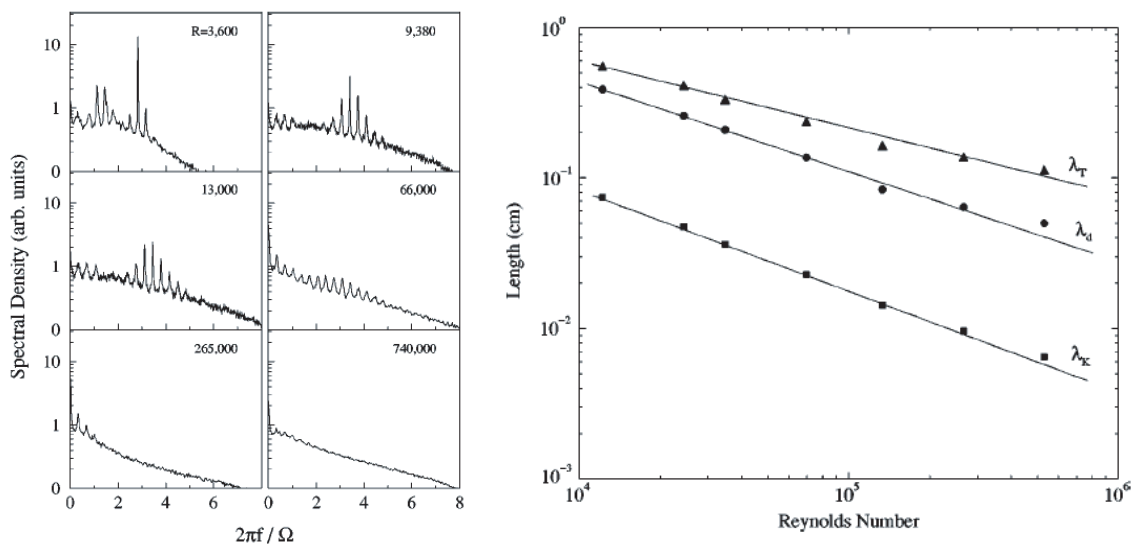
Figure 2.5: Left: Velocity power spectra measured by Lewis and Swinney[Lewis and Swinney, 1999] in a centrifugally unstable flow. The measurement was performed on the mid-radius of the apparatus, just above the mid-height. All peaks are close multiples of the lowest frequency. The frequency has been normalized to the rotation frequency of the inner cylinder. Right: Scaling of Kolmogorov (λ_K, squares), Taylor (λ_T, triangles) and dissipation (λ_d, circles) scales. The separation of scales is too small to allow the formation of an inertial range.

From data provided by hot film probes at the mid-radius of their apparatus detected the presence of azimuthal traveling waves, see Figure: 2.5. The power spectra reveal the presence of multiple modes which are multiples of the lowest frequency. The waves are detectable up to the highest Reynolds numbers used in the experiment, and above $Re \sim 10^4$ they have a nearly constant velocity. That

angular wave speed is calculated by dividing the frequencies of the dominant peaks by the mode number and averaging, and is found to be roughly equal to that of the mean flow at the mid-radius:

$$\text{wave angular speed} \sim \frac{\Omega_1 r_1^2}{2\tilde{r}^2}. \tag{2.11}$$

Finally, Lewis and Swinney measure the Kolmogorov, Taylor and dissipation length scales of the turbulence. Their data is reproduced in the right panel of Figure: 2.5. The scale separation is insufficient to allow the formation of an inertial range. Extrapolating to Reynolds numbers produced in the hydrodynamic experiments of the PRINCETON MRI EXPERIMENT , $Re \sim 10^6$, the Kolmogorov scale is $\approx 4 \times 10^{-5}$ m.

Turbulence in the cyclonic regime: Wendt and Taylor

The works of Wendt [Wendt, 1933] and Taylor [Taylor, 1936] remain the most precise measurements of fluid torque in the turbulent cyclonic regime. Parameters for the two experiments are listed in Table: 2.1. The aspect ratio used by Taylor is far greater than that of Wendt. Taylor's end caps were fixed to the outer cylinder, and velocity measurements indicate that near the inner cylinder, boundary layer effects still produce a large deviation from the ideal circular-Couette solution, Equation: 2.3. In contrast, Wendt used a split end-cap at the base of his experiment, with one half of the cap fixed to the inner cylinder, and other half fixed to the outer. In addition, the upper surface of the experiment was a free surface with no cap. This produced a speed dependent aspect ratio, but was overall less impacted by Ekman circulation.

At sufficiently large Reynolds number Taylor and and Wendt observe turbulent transitions within their cylconic circular-Couette flows. In the left panel of Figure: 2.6 the transition Reynolds number is plotted against the experiment gap width.
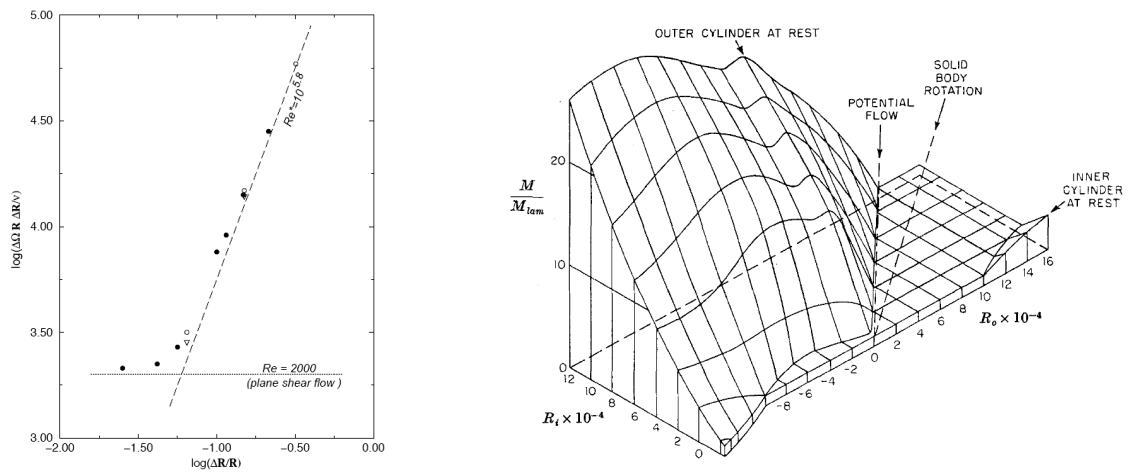
Figure 2.6: Left: Reproduced from [Richard and Zahn, 1999] Dependence of transition Reynolds number on aspect ratio. Filled circles are Taylor's data [Taylor, 1936], Open circles are Wendt [Wendt, 1933]. Horizontal dashed line is the transition Reynolds number for plane Couette flow, dashed line is proposed gradient Reynolds number. Right: Figure reproduced from Coles[Coles, 2006]. Wendt's measurements of torque in laminar and turbulent regimes. Height of surface represents the ratio of measured torque to theoretical laminar torque. Reynolds numbers of cylinders are computed using $Re_{i,o} = \Omega_{i,o} r_{i,o}^2 \nu^{-1}$, subscript refers to inner (outer) cylinder.

2.1.3 Experiments in the quasi-Keplerian regime

Richard

Until the work of Richard[Richard, 2001], there were no experimental observations of turbulent transition in the quasi-Keplerian regime. Using an apparatus developed by Prigent *et al* [Prigent and Dauchot, 2000] Richard sought to connect the turbulent torque measurements of Wendt and Taylor's cyclonic flows to the quasi-Keplerian regime.

Parameters for the experimental apparatus can be found in Table:2.1. The end caps are divided in to two nested rings which can be fixed to the cylinders in two ways: 1) both rings fixed to the outer cylinder, or 2) the rings are "Split" with the inner ring fixed to the inner cylinder and the outer ring fixed to the outer cylinder. After demonstrating that the first option produces flow profiles heavily influenced by Ekman circulation (similar to Taylor) the `Split` configuration is adopted.

The explored Reynolds numbers and observations of turbulence are reproduced in Figure: 2.7.

Using Kalliroscope[Dominguez-Lerma et al., 1985] Richard explored the stability boundary for flows in his apparatus in both the cyclonic and quasi-Keplerian regimes. The inner cylinder was painted with a fluorescent paint which glowed for some time after a UV light source was turned off. A CCD oriented radially measured a flux emitted by the paint and transmitted through the Kalliroscope flakes suspended in the fluid. The Kalliroscope flakes align with the local fluid shear. In the laminar state the flakes align with the rotation axis and therefore block the transmission of light from the inner cylinder. When a transition occurs, the flakes realign and light may be transmitted.

In the cyclonic regime, the transitions observed by Wendt and Taylor are
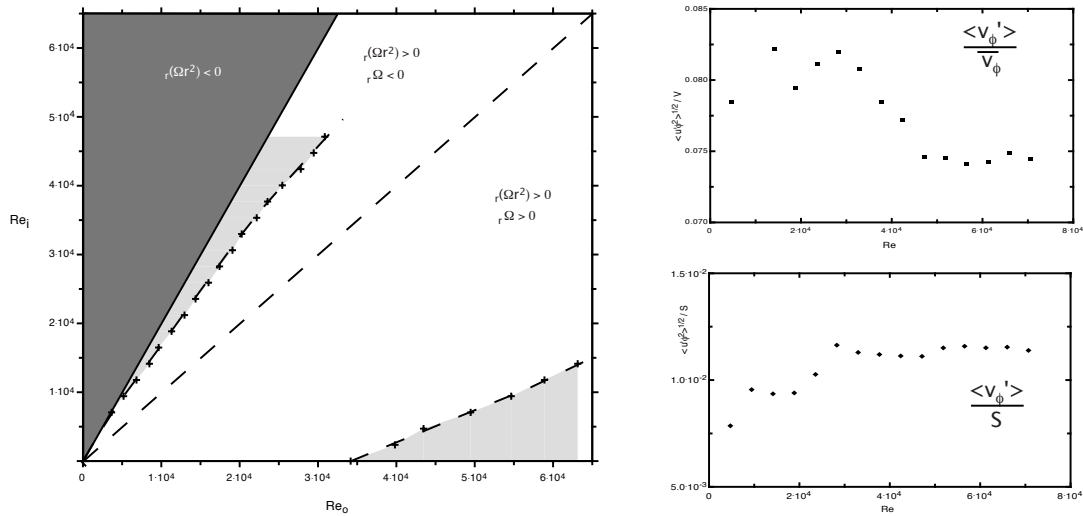
Figure 2.7: Left: Reynolds numbers explored by Richard. Dark gray region is linearly-unstable by Rayleigh's criterion.The other regions are linearly-stable. In the light gray regions Richard observes a turbulent transition. The observations involve qualitative flow imaging with Kalliroscope and velocity measurements using Laser Doppler Velocimetry. Right: RMS fluctuation levels in azimuthal velocity for cyclonic flow. The top panel is normalized by mean azimuthal velocity, the bottom is normalized by radial shear of the profile: $S \equiv r\partial\Omega/\partial r$.

reproduced and a hysteresis in transition Reynolds number is observed: in scanning from the laminar state to turbulence the transition occurs at a higher Reynolds number than when scanning down in Reynolds number from the turbulent state to the laminar one. Such hysteresis is characteristic of sub-critical transitions (see Section: 1.3). However, no information is provided about the level of fluctuations nor their origin. Visualization studies by Schultz-Grunow[Schultz-Grunow, 1959] indicate that surface defects may drive the transition.

Azimuthal velocity and fluctuation levels were measured using Laser Doppler Velocimetry (see Section:3.5.1), LDV. A transition in fluctuation levels is observed in the cyclonic regime, as can be seen in the right panels of Figure: 2.7. In the right panel, the upper figure presents fluctuations in azimuthal velocity normalized to the mean velocity, which is the definition of turbulent intensity used by Lewis and Swinney (see Section: 2.1.2).

In the quasi-Keplerian regime a transition is also observed using the Kalliroscope. In this case, a difference in transition Reynolds number could not be determined when scanning from the laminar to turbulent state or vice versa. Richard does not provide fluctuation levels versus Reynolds number in the quasi-Keplerian regime. Transport is inferred from deviation of mean flow profile from non-turbulent state. *(need to double check the private communication with Burin here)*

Beckley

Beckley [Beckley, 2002] constructed a large gap, small aspect-ratio circular-Couette apparatus to study MHD dynamo and MRI activity. The apparatus is capable of operating in both cyclonic and anti-cyclonic regimes at Reynolds numbers in excess of 10^6, see Table:2.1. The end caps of the apparatus are fixed to the outer cylinder. He performed an angular momentum transport

measurement in water for stable anti-cyclonic flow. The measured scaling of applied motor torque versus Reynolds number indicate that the advection via Ekman pumping is the dominant transport mechanism in the apparatus.

To date the experiment has not reported any MHD measurements.

Prototype of the PRINCETON MRI EXPERIMENT

The need to maximize the probability of producing the MagnetoRotational Instability in the PRINCETON MRI EXPERIMENT while minimizing the required volume of GaInSn placed a severe constraint on the aspect ratio of the apparatus, $\Gamma \sim 1$. For such a small aspect ratio, the boundary layers must have a significant impact on the mean flow profile. A prototype experiment [Kageyama et al., 2004] was developed to investigate the hydrodynamic properties of a $\Gamma \sim 1$ device using water. The kinematic viscosity of water and GaInSn are nearly equal ($\nu_{GaInSn}/\nu_{water} \approx 0.3$) so the results could be expected to also hold for the liquid metal.

The apparatus was constructed with both end caps fixed to the outer cylinder. The caps and outer cylinder were made of Acrylic. Azimuthal velocity was measured using Particle Tracking Velocimetry. Reflective particles entrained in the flow were imaged with a CCD. Azimuthal velocity of the particles was measured by dividing the distance the particle moved in a single image by the image exposure time. The results for a flow at $Re \sim 10^6$ are reproduced in Figure: 2.8. The measured velocity is compared to the ideal circular-Couette profile as well as a 2-D code developed to simulate the flow in the experiment.

The observed profile and its agreement with the simulation demonstrates that this experimental setup would be unsuitable for producing an unambiguous detection of the MRI. There are two reasons for this: first, the sharp drop in velocity at the inner cylinder surface indicates that that region of the flow is unstable by the

Rayleigh criterion to centrifugal instability. The interaction of this unstable region with an applied magnetic field could be difficult to distinguish from effects produced by the MRI. Second, the velocity profile is significantly flattened compared to the ideal circular-Couette profile over the bulk of the experiment volume. Production of the MRI in a liquid metal is a balance between growth produced by shear in the angular velocity and stabilization due to viscosity and resistivity. The low shear bulk flow is therefore likely to be stable to the MRI.
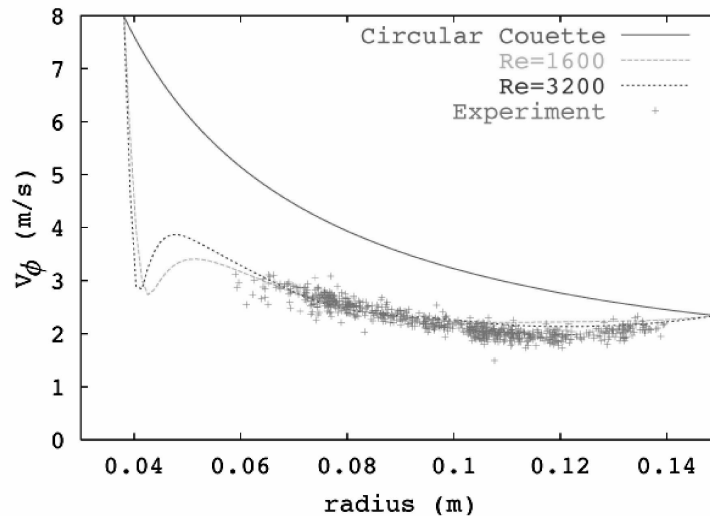
Figure 2.8: Mean velocity profile measurement and simulation of low aspect ratio prototype experiment with end caps fixed to the outer cylinder. From: [Kageyama et al., 2004]

Analysis of the simulation prediction of boundary layer thickness motivated a new prescription for the Ekman layer thickness, see Section: 2.1.1. Application of this estimate of Equation: 2.7 for δ_{Ekman} to the spin-down time of the flow yielded good agreement with the measurement.

2.2 Magnetized circular-Couette Flow

2.2.1 Prior experiments on magnetized rotating shear flow

This section briefly reviews existing and proposed magnetized experiments in rotating liquid metal shear flow. The focus is primarily on circular-Couette experiments but does include a discussion of the results from the University of Maryland's spherical-Couette liquid Sodium experiment, in which an observation of the MRI has been claimed.

Donnelly and Ozima

Donnelly and Ozima [Donnelly and Ozima, 1960][Donnelly and Ozima, 1962] confirmed the theoretical predictions of Chandrasekhar [Chandrasekhar, 1953] and Niblett [Niblett, 1958] that a centrifugally unstable circular-Couette flow of mercury can be stabilized by a large magnetic field. Their apparatus featured a very narrow gap width of 2.0mm between cylinders of radii $r_1 = 18.0$mm and $R_2 = 20.0$mm and height 100.0mm. The outer cylinder was held fixed by a torsion wire which was used for torque measurement. At their maximum Reynolds number, $\approx 3 \times 10^3$, the field required for stabilization was $\approx 14kG$. The stabilization of the centrifugally unstable flow in the PRINCETON MRI EXPERIMENT is possible only when operating very near the Rayleigh stability limit, but is otherwise impossible: our Reynolds number are 10^3 larger, gap width is > 60 times that of Donnelly and Ozima, and our largest applied magnetic field is only 5kG.

Maryland MagnetoRotational Instability observation

A group at the University of Maryland [Sisan et al., 2004] claim to have observed the MagnetoRotational Instability in a spherical Couette flow. They observe non-axisymmetric fluctuations in the radial magnetic field, B outside the spheres which vary with applied field strength and Reynolds number. Azimuthal velocity, as measured by ultrasonic doppler velocimetry shows a similar oscillation. An excess of torque transmitted to the outer sphere is also measured. The reported applied magnetic field amplitudes are too small to suppress the MagnetoRotational Instability.

Significant details of the experiment make it difficult to attribute the observed results solely to the MagnetoRotational Instability. Figure: 2.9 reproduces two figures from the experiment. The first of these figures is a velocity measurement of the flow in the absence of an applied field. The second displays as a function of applied field the induced radial magnetic field measured outside the outer sphere and the excess torque required to drive the inner sphere. Each of these figures will be discussed in turn.

The specific angular momentum measured by the Maryland group is an increasing function of radius, see the left panel of Figure: 2.9. However, the outer sphere is at rest and $Re > 10^5$ so we expect the flow to be in a state of fully developed turbulence. Because angular momentum is the source of free energy for centrifugal instability the bulk of the flow should relax to a profile of near-constant angular momentum, bounded at the walls by an unstable boundary layer. This type of profile was measured by Lewis and Swinney, see Section: 2.1.2. At least one unstable boundary layer must exist in this experiment: the angular momentum of the outer sphere is identically zero and the profile must transition to that value when it reaches the outer sphere. Because the bulk flow is not close

to saturation, a radial advection must be present to transport the angular momentum required to maintain the outer unstable layer. Evidence of the return flow can be seen interior to the tangent cylinder radius (the vertical projection of the inner sphere's radius): the angular velocity increases radially above the constant $30 rad/s$ of the inner sphere and axle.

Inertial waves [Greenspan, 1968] can be excited by turbulent boundary layers [Townsend, 1980]. If inertial waves are responsible for the azimuthal waves observed by Lewis and Swinney, a similar phenomena may be in operation in this experiment. Sisan hints that hydrodynamic oscillations are present, stating "Smaller turbulent fluctuations are also observed in the magnetic field in the base state, due to interactions between the fluid turbulence and the Earth's relatively weak field..."

In right panel of Figure: 2.9 an excess of torque is required to drive the inner sphere when the oscillating radial field turns on. The shear layer ultimately couples the flow to the boundary so in the absence of a detailed understanding of that layer, it is premature to attribute the secular increase in torque to the action of the MagnetoRotational Instability.

This discussion is rather speculative, but does serve to highlight the difficulties of interpreting results that arise from a background flow which is not well-characterized. It also highlights the truly unique experimental opportunities that arise from the design of the Princeton MRI apparatus. By choosing the speeds of the end-rings we will able to fine-tune transport induced by the boundaries.

Helical MRI: the PROMISE experiment

Hollerbach and Rüdiger [Hollerbach and Rüdiger, 2005] citeRudiger:2005 discovered that the presence of toroidal as well as axial component to the applied magnetic field produced an MRI-like mode. The threshold for instability is
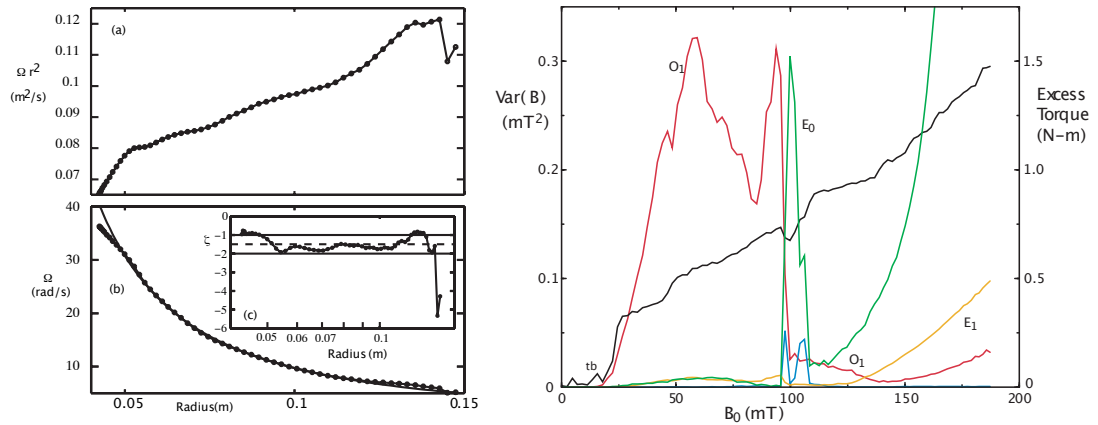
Figure 2.9: Reproduced from Sisan *et al* [Sisan et al., 2004]. Left figure: specific angular momentum (a), angular velocity (b) and local mean exponent of angular velocity (*inset*). *n.b.* $\zeta = \partial \ln \Omega / \partial \ln r$ is opposite in sign to q employed here. The velocity is measured along a chord in the r-ϕ plane and passes near ($\sim 1cm$) the rod supporting the inner sphere. Right figure: Induced B_r and excess torque versus applied field. Red and orange reflect fluctuations from their means. The "E_0" state showed significant mean amplitude: squared-average of the mean is green, variance is blue.

significantly smaller than is predicted for a purely azimuthal magnetic field. The PROMISE experiment in Potsdam has claimed to observe the Helical `MRI` in a circular-Couette flow[Stefani et al., 2006]. The apparatus consists of Copper cylinders of radii, $r_1 = 40, r_2 = 80$ mm and axial extent $h = 400$ mm. The top end cap of the cylinder is stationary to allow the use of Ultrasonic Doppler Velocimetry. The bottom end cap rotates with the outer cylinder. The Ekman circulation generated by the end caps is asymmetric about the apparatus midplane. The applied magnetic field is of order 100 G. At $Re \sim 10^3$ they observe an axial traveling wave with frequency $\omega/\Omega_1 = 0.15$, wavelength 6 cm and phase velocity 0.7 mm/s.

There is some debate over whether this instability is related to the MRI at all. Simulations by Liu[Liu, 2007], [Liu et al., 2006a] indicate the disturbances are a weakly destabilized inertial oscillation excited by the Ekman circulation, and are in excellent agreement with the PROMISE observations. They also find that the effect is absent in the case where the end caps of the experiment are insulating. Unlike the standard version of the MRI presented in Section: 1.2, the helical MRI features a slow growth rate which is unlikely to make it relevant to accretion disks. Lakhin and Velikhov [Lakhin and Velikhov, 2007] estimate the growth rate to be $\sim \sqrt{\Omega}$ and also interpret the mode as a weakly destabilized inertial oscillation rather than MRI.

PRINCETON MRI EXPERIMENT

Ji *et al* performed an axisymmetric WKB analysis of a proposed liquid gallium circular-Couette experiment with small aspect ratio and wide gap geometry that later evolved in to the present PRINCETON MRI EXPERIMENT apparatus. They found instability to the MRI for $Re_m \sim 1$ and applied magnetic field $B_z \sim 5$ kG. The most unstable modes found in this analysis have wavelengths greater than

the gap width and cylinder height. Based on this, they note that the WKB analysis should not be trusted *a priori*. They extend the analysis using a global linear code with periodic vertical boundary conditions. Their findings agreed well with the results of the WKB analysis. A plot of regions of instability to the MRI is reproduced from [Ji et al., 2004] in Figure: 2.10. Three regions are shown. Region I is always unstable but can be stabilized by a suitably strong magnetic field, as Donnelly and Ozima demonstrated. Region II is the portion of the quasi-Keplerian regime that can be destabilized by an applied magnetic field. Stability curves are shown for the first five axial mode numbers. Region III is always stable.

Liu [Liu, 2007] adapted the ZEUS 2-D axisymmetric compressible MHD code to simulate MRI in the PRINCETON MRI EXPERIMENT . He found that the MRI could be destabilized by flows as low as 45% of the experiment design maximum of $Re_{max} = 2 \times 10^7$. The simulations of at the largest Reynolds number yet achieved in the experiment, 60% of Re_{max}, show the MRI has a linear phase in which the radial magnetic field growing at $\partial B_r/\partial t \sim 1\,\mathrm{G/s}$ followed by saturation at $B_r \sim 1\,\mathrm{G}$. The saturated state of the MRI is an inward-directed radial jet at the midplane with a reconnection layer at the center of the jet. The inward flow of the jet is opposite to that produced by Ekman circulation.

Goodman and Ji: results of global stability code confirm prior earlier results. Several axial modes should become unstable for Princeton MRI Experiment, see Figure: 2.10.

Liu *et al*[Liu et al., 2006b] ZEUS-2D simulation of Princeton MRI experiment shows good agreement with linear analyses for growth phase of the `MRI` . Nonlinear saturation occurs through an in-flow jet (opposite sense to Ekman circulation) at the mid-plane of the experiment. Radial speed of the jet $\sim Re_m^{-1/2}$.
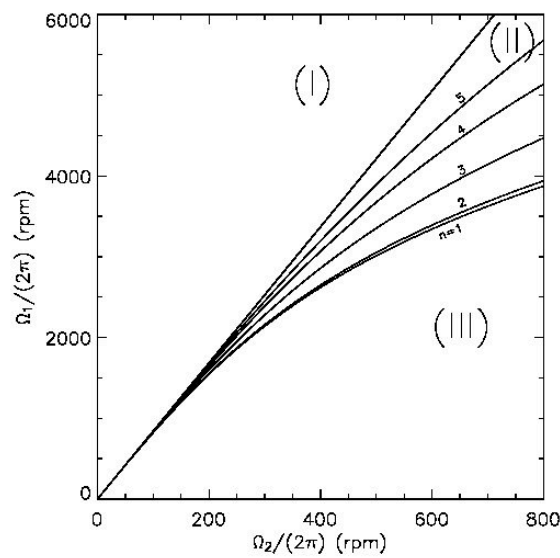
Figure 2.10: MagnetoRotational Instability axial mode number which are expected to become unstable in the presence of an axial magnetic field. From [Ji et al., 2004]. Region I is linearly unstable by the Rayleigh criterion as well as MRI unstable. Stability can be restored by sufficiently large applied magnetic field. Region II is linearly stable but can become unstable to the MRI for particular values of the applied field. Region III is always stable to the MRI.

Reconnection layer forms within the jet.

Other proposed MRI experiments

Noguchi *et al* performed a study of MRI stability based on the New Mexico $\alpha - \omega$ dynamo experiment, see section: 2.1.3 for a description. The analysis models the effect of the Ekman circulation as a background turbulence. They conclude the flow is more unstable to MRI than PRINCETON MRI EXPERIMENT . In initial MHD experiments the Sodium formed an emulsification with the a mineral oil used to heat the Sodium and prevent it from contacting the seals (*unpublished*). The experiment is awaiting a solution to this technical difficulty.

Velikhov's [Velikhov et al., 2006] performed a stability analysis for a $q = 2$ rotating liquid Sodium shear flow driven by radial current. He estimates the critical Reynolds number to be as low as 10^4. The radial currents required to drive the azimuthal flow may produce a toroidal field component which is itself unstable.

Chapter 3

Experimental Apparatus

The design of the PRINCETON MRI EXPERIMENT is constrained by the need to maximize the magnetic diffusion time of the experiment so that it is longer than the MRI growth time while minimizing the quantity of GaInSn owing to the metal's expense. This optimization results in a circular-Couette experiment of wide gap and low aspect ratio. Experiments[Kageyama et al., 2004] with a prototype of this geometry demonstrated that the influence of the cylinder end-caps produces a mean flow profile significantly altered by angular vertical momentum transport, see Section: 2.1.3. Simulations indicated that dividing the end caps into rings that rotated independent of the cylinders would establish a favorable mean flow.

A photograph of the PRINCETON MRI EXPERIMENT experiment is show in Fig. 3.1. The circular-Couette flow is established in a fluid volume confined between concentric co-rotating cylinders and capped at each end by two differentially rotatable end-rings. The dimensions of the experimental volume are list in Table:3.1 The rotating components are mechanically supported by an Aluminum frame. The frame is hinged near the experiment center-of-mass and can be rotated $90°$ for installation of the rotating components. The magnet coils and drive motors

are also mounted to the frame.

The design and construction of a circular-Couette experiment capable of achieving $Re \sim 10^7$, dynamic pressures of $\sim 25\ \mathrm{atm}$ and the peculiar constraints required of a scientific apparatus has been a challenging and evolving engineering task. Where it is required in order to understand the functionality of the current apparatus some discussion of superseded designs will be made.
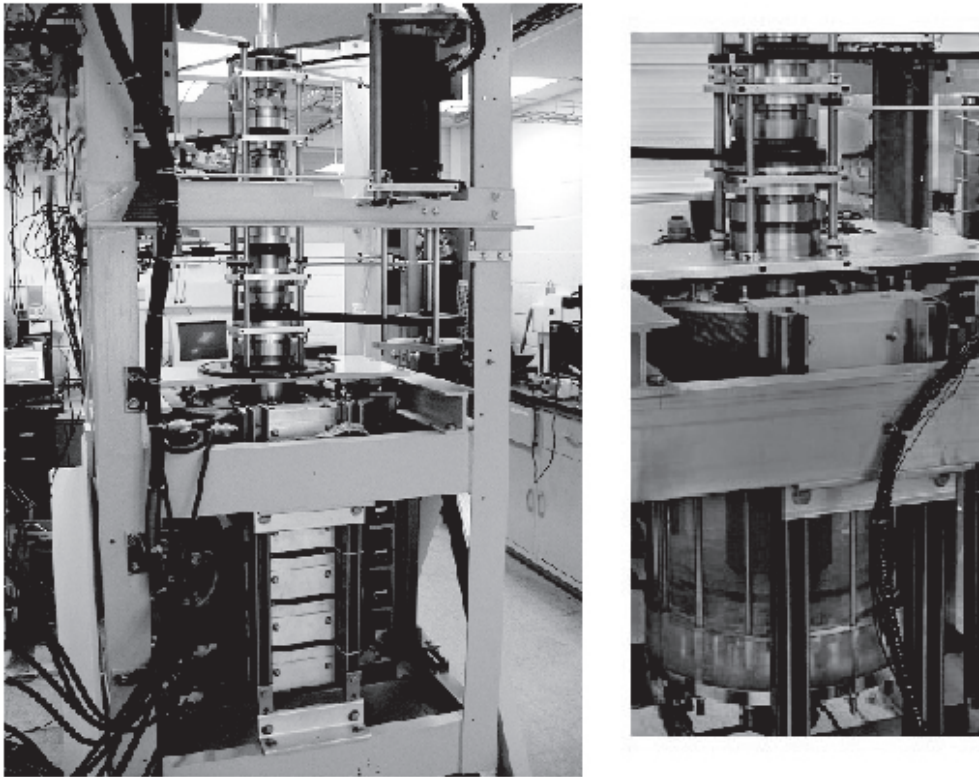
Figure 3.1: Left: The PRINCETON MRI EXPERIMENT just prior to gallium operation, Right: Close-up of the experimental volume before installation of magnet coils and stainless steel outer cylinder.

Table 3.1: Experimental dimensions. Ring gap radius is the location of the gap between the inner and outer end rings.

Inner cylinder radius	r_1	$70.6mm$
Outer cylinder radius	r_2	$203.0mm$
Ring gap radius	$r_{3,4}$	$132.5mm$
Gap width	$d = r_2 - r_1$	$132.4mm$
Cylinder height	h	$280.0mm$

3.1 Rotating Assembly

3.1.1 Cylinders and rings

The experiment outer cylinder is a pressure vessel designed to withstand 25 atmospheres in which the other rotating components are submerged. The cylinder is formed by an annulus of cast acrylic or type 304 stainless steel capped by two acrylic disks. The wall thickness of the acrylic annulus is 25.4 mm and 9.5 mm for stainless steel. The caps are 101.6 mm thick with the bottom cap polished to permit the use of optical diagnostics. The caps are drawn against the annulus by 16 stainless steel tie rods. Stress concentrations due to the tie rods that would potentially damage the caps are borne by 25.4 mm thick by 38.0 mm wide stainless steel rings. The rings feature electrical breaks at two points. O-rings are used to seal the annulus to the caps.

The experiment was originally designed to use an acrylic annulus for the outer cylinder under operation with both water and GaInSn. The wall thickness was chosen to withstand the dynamic pressure generated by the GaInSn based on the yield stress of the acrylic. During a peer review, a concern was raised that crazing failure (see Fig:3.2) of acrylic can occur for stresses 1500 psi below the yield point. The stresses developed at the interface of the outer cylinder with the end caps was calculated to be 4300 psi while the yield strength of the acrylic is 7200 psi.

This proximity of the crazing point to the maximum stress prompted us to manufacture a new outer cylinder for use with GaInSn. Transparency of the outer cylinder is not needed during liquid metal operation so stainless steel was chosen as the replacement material.
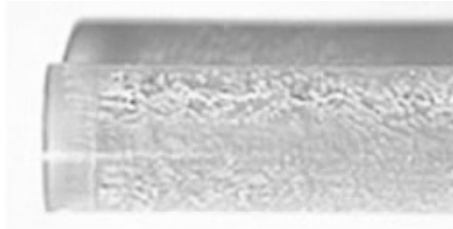
Figure 3.2: An acrylic sight glass which has become crazed. Crazed materials have the potential to undergo sudden "catastrophic" failure. Photo credit: ESC plastics.

The outer cylinder assembly is supported vertically by a quick-draw bushing which clamps to a central stainless steel axle $35\ \mathrm{mm}$ in diameter and $2.06\ \mathrm{m}$ in length. An O-ring crushed between the bushing and bottom cap seals the joint where the axle passes through. The center axle is hollow to accommodate potential experimental work using a toroidal magnetic field in addition to the vertical one. A flange-mounted ball bearing on the lower cross piece of the experiment frame provides radial and thrust support for the outer cylinder assembly. Vertical alignment of the outer cylinder is set by another quick-draw bushing clamped to the center axle which rests on the flange bearing inner race. The upper end of the outer cylinder is radially supported by a plain bearing located between the upper axle and the axle of the upper outer ring. The bearing also features a groove which holds the #1 seal and guarantees the seal's concentricity to both axles.

The inner cylinder and all of the rings are mounted to nested stainless steel axles which pass through the outer cylinder top cap. Each ring is machined from cast acrylic and mount via screws to a flange welded to the submerged end of the axle.

The inner cylinder is stainless steel welded to its axle. The inner cylinder is filled to its axle diameter with nylon to reduce the required amount of GaInSn. A lip seal is mounted at the top end of each axle to seal against its inner neighbor. Each axle has a 6.3 mm hole drilled 25.4 mm below the lip seal landing area to allow fluid to fill the inter-axle gaps. The submerged, lower, end of each component is fixed radially by a plain bearing. The lower rings were polished to allow optical access for diagnostics.

The rings, inner cylinder and axles were static balanced during manufacture. The upper ends of the rotating components require radial support by an external frame, which prevented balancing of the apparatus as a unit. The "as assembled" balance is adequate and operation of the experiment is not limited by mechanical vibration of rotating components.

3.1.2   Seals and Seal Cooling

Spring-energized lip seals (see Fig:3.4) are used to seal the axles to one another where they thread out of the outer cylinder pressure vessel. The seal lips are made of a PTFE-filled plastic and are rated to about 2 MPa, though they do not ever experience such high pressures. The radial force applied by the seal to its sealed surface varies with the pressure at the seal. Each seal has a fluid path that couples it to the bulk flow at one of three radii: the inner cylinder, the ring gap or the outer cylinder. Because the flow is pressure supported, the seal friction is sensitive to the flow profile. This makes the torque required to rotate the components unsuitable for measuring the viscous torque required to maintain the flow. In other experiments [Beckley, 2002][Sisan et al., 2004] motor torque is a primary diagnostic.

Seals #1, 2 and 3 are located radially by a thermoplastic ring: seal #1 uses Techtron

1. Outer Cylinder center axle
2. Seal #6
3. Lower Outer Ring pulley
4. Lower Outer Ring axle
5. Seal #5
6. Lower Inner Ring pulley
7. Lower Inner Ring axle
8. Seal #4
9. Inner Cylinder pulley
10. Inner Cylinder axle
11. Seal #3
12. Upper Inner Ring pulley
13. Upper Inner Ring axle
14. Seal #2
15. Upper Outer Ring pulley
16. Upper Outer Ring axle
17. Seal #1 and radial bearing
18. Outer Cylinder upper axle
19. Outer Cylinder top cap
20. Submerged radial bearing
21. Upper Outer Ring
22. Submerged radial bearing
23. Upper Inner Ring
24. Nylon filler
25. Inner Cylinder
26. Outer Cylinder
27. Tie rod (1 of 16)
28. Submerged radial bearing
29. Submerged radial bearing
30. Lower Inner Ring
31. Lower Outer Ring
32. Submerged radial bearing
33. Outer Cylinder bottom cap
34. Quick draw bushing

Figure 3.3: Rotating components of the PRINCETON MRI EXPERIMENT experiment as originally designed by Lew Morris.
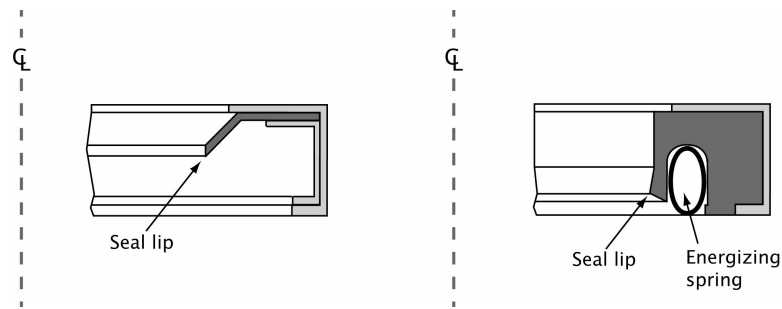
Figure 3.4: Left: Unsupported lip seal. Right: Spring energized lip seal.

HPV, the others are Acetyl Copolymer. The rings are machined for a precise fit in to the inner diameter of the axle. O-rings are used for the static seals between the lip seal and ring and between the ring and the axle. A stainless steel retaining ring clamps the seal against the axle end.

Seals #4 and 5 originally used uniquely sized seals. The original seals were abandoned because they wore out too quickly, required radial alignment tolerances that were difficult to meet, and caused damage to the axles. Adapters are used to allow the #3 seal to be used as replacements for the originals. The adapter is diagrammed in Fig:3.5. The inner diameter of the larger axle is adapted out by a sleeve. A retaining ring draws the seal against this sleeve and O-rings provide for the static seals between the seal and sleeve, and sleeve and axle. The sealing face is a Stainless steel annulus which is fixed to the inner axle by a shaft clamp.

A drawback to the adapters used for seals #4 and 5 is that fluid access for cooling the seal is limited and the use of stainless steel causes heat to buildup at the seal. The heating of the seal causes erratic torque demands on the motors. Automatic Transmission Fluid (ATF) is sprayed on to all the seals to reduce friction and remove heat. In addition, Seal 5 features a large finned Aluminum heat sink to improve cooling of the seal.

Seal #6 also required a unique mounting scheme to meet its alignment
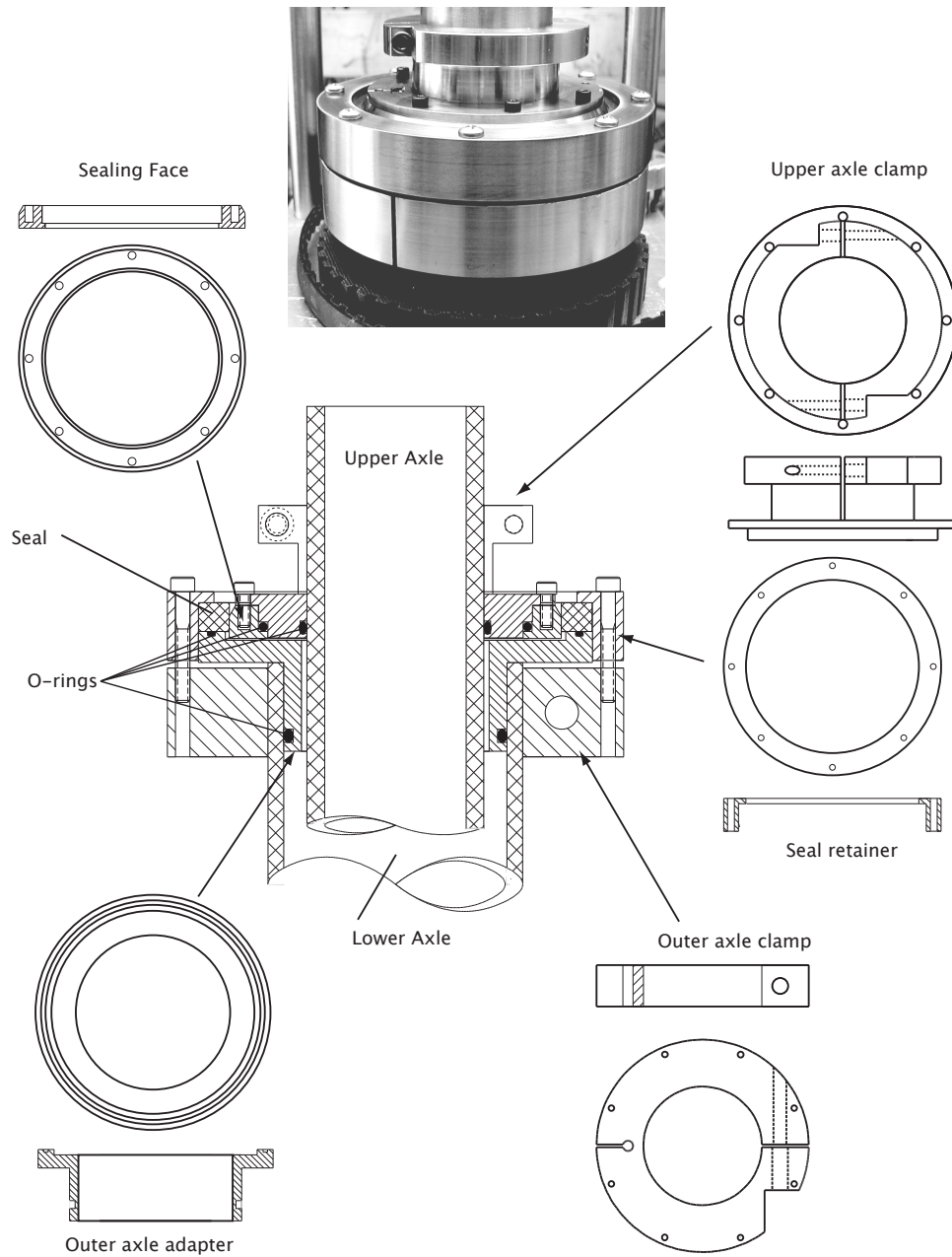
Figure 3.5: Adaptor for seals #4 and #5

specification of 0.05 mm Total Indicated Runout. The outer cylinder center axle which threads through the entire machine does not have a radial bearing and plate combination as described in Section: 3.1.3. Instead, the seal holder has a ball bearing mounted in it, above the seal. A slip-fit bushing adapts the outer cylinder axle to the bearing inner diameter. The bearing outer diameter and seal share a housing which is concentric and clamped to the lower outer ring axle.

3.1.3   Bearings

The axles supporting the end rings and inner cylinder are each aligned and supported by two bearings. One is mounted in the submerged end of the component to provide radial location, and the other is clamped to the axle to carry combined thrust and radial loads.

Submerged Bearings

The submerged radial bearings are located as listed in Figure: 3.3. They are plain type 25 mm thick, machined from Techtron HPV (PTFE-filled PolyPhenylSulfide). The Techtron HPV was chosen for its excellent wear resistance, low sliding friction and low absorption of water. Though they are submerged in the apparatus' working fluid, the clearances between bearing inner diameter and axle are too large for the development of load-supporting hydrodynamic films. The radial clearance is not well controlled, ranging from about 0.03 mm to 0.15 mm. The clearance is necessary to allow the entire length of each axle to pass through the bearing during assembly.

Owing to these clearances, the inner cylinder has a radial runout ($m = 1$ mode) with minimum amplitude of 0.30 mm, based on the radial clearance of the bearing mounted in the bottom of the inner cylinder. The upper limit for the runout was

estimated to be a maximum of 0.76 mm from time series LDV data acquired near the inner cylinder. See Section: 3.5.1 for details.

Radial support of the upper axle of the outer cylinder is performed by a Techtron bearing submerged just below Seal #1. The bearing has a ring cut in to it to mount the seal, which allows proper axle alignment for the seal to be maintained.

Combined-Load Bearings

A bearing is clamped to each axle above the point at which the axle is sealed by its larger neighbor, see Figure: 3.3. The clamping mechanism is diagrammed in Figure: 3.6. The axle is adapted out to the bearing inner diameter by a split bushing. The split bushing has a shoulder to prevent the bearing from interfering with the two-piece clamp which fixes the bushing to its axle. Axial movement in the other direction is prevented by another two-piece clamp. The clamp assembly provides precise radial location of the axle within the bearing and supports it against thrust loads. The direction of the thrust load may vary with the working fluid and the operating speed. For example, the upper outer ring and axle float in the GaInSn when stationary, but dynamic pressure acts to draw the assembly down into the bulk fluid volume.

The outer diameter of the combined-load bearing is captured by a 200 mm square Aluminum plate. Each plate is threaded by four precision ground 19 mm diameter steel rods. The plates are clamped to the rods after fine adjustment of the vertical clearances of the submerged components. The rod-plate combination provides thrust and radial support to the bearings. Deflection of the plate stack is prevented by Aluminum tensioning straps which run from the frame to the rods. The entire bearing assembly is removed from the axles and frame before disassembly. If a seal needs to be replaced the bearings and plates above that seal are removed to allow the seal to pass over the axles.
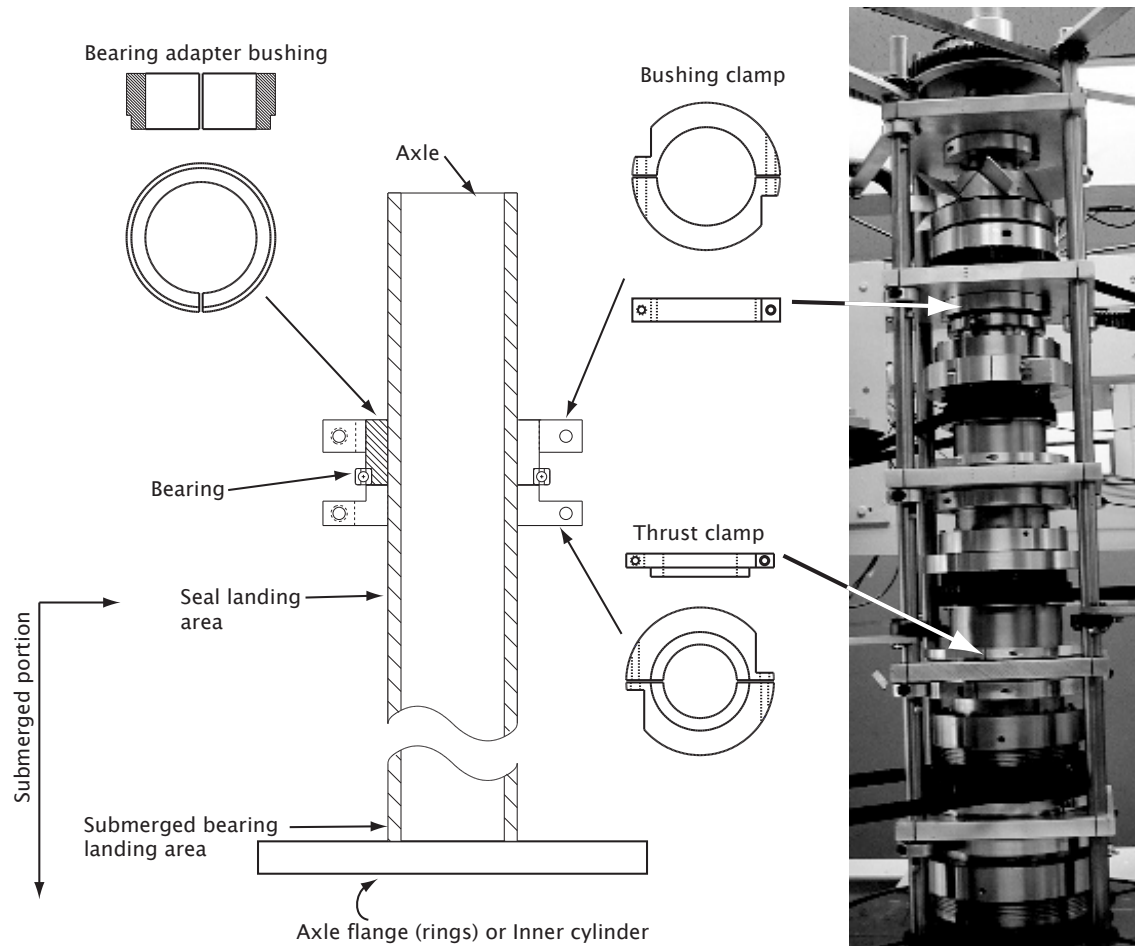
Figure 3.6: Diagram: clamp components and arrangement to fix ball bearings to axle. Photo: The bearing stack portion of the frame which supports the bearings and ensures concentricity.

3.1.4 Dynamic Pressure

The fluid rotational profile developed in gap between the cylinders is pressure supported:

$$\frac{\partial P}{\partial r} = \rho r \Omega^2,$$

where P is the pressure at radius r and ρ is the fluid density. In the absence of vertical pressure gradients, the surfaces of the end rings which face the experimental volume must also support this pressure. The fluid in the volumes between the rings, and between the outer cylinder and outer ring do not have a rotation profile identical to that of the bulk flow: this profile is approximately solid body rotation. The pressure generated by the solidbody rotation is a small correction to the bulk flow pressure profile. Therefore the pressures in the non-experimental fluid volumes are approximately equal to the bulk pressure where a vertical gap provides a link to the bulk flow. This is diagrammed in Figure: 3.7 along with pressure profiles for an ideal circular-Couette experiment. During the hydrodynamic experiments presented in Chapter 4, the pressures developed across the end rings was insufficient to disrupt the experiment operation. Interference of the rotating components were observed during high-speed testing in water, when preparing to switch over to GaInSn operation. As shown in Figure: 3.8, interferences of four components occurs. At the point marked "A", the upper outer ring was drawn up against the outer cylinder top cap. The deflection away from the bulk fluid occurred for two reasons. One was that the ring was too close to the cap to allow propagation of the bulk pressure along the entire top surface of the end ring. The second is that the equilibration hole between the upper outer and inner rings caused the bulk of the outer ring to experience the lower pressure of the ring gap. Blocking the equilibration hole confirmed that this pressure differential was the cause of the problem. At the
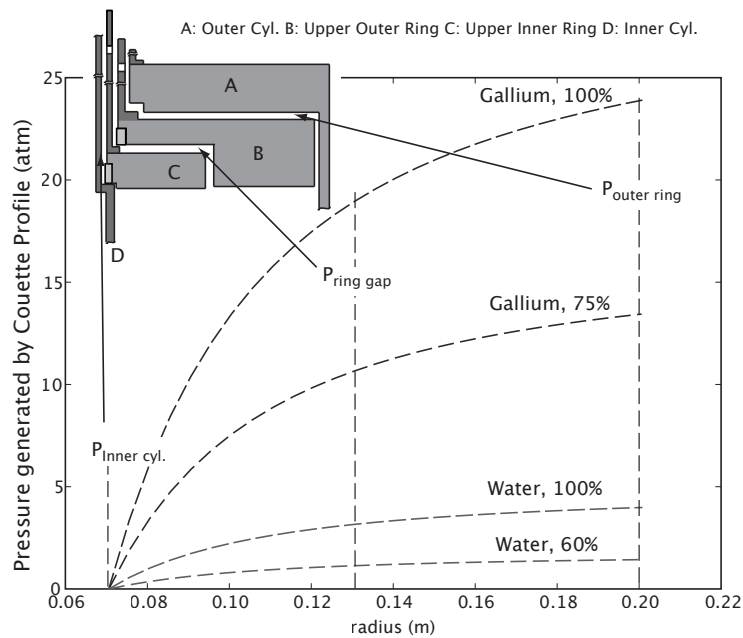
Figure 3.7: Pressure versus radius for ideal circular-Couette flows generated by the `MRI` speed profiles.

point marked "B", the inner rings are being pushed against the inner cylinder by the ring gap pressure. Here, the combined-load bearings for the inner rings had too much axial play to maintain a proper clearance. The interference of the inner rings with the inner cylinder could be eliminated by adjusting the vertical spacing of the upper and lower rings. However, this would introduce interference between other components.

To permanently fix the dynamic pressure problem, a series of holes were drilled vertically through the end rings, as shown in Figure: 3.9. The holes are 5.10 mm in diameter drilled at eight radii on the inner and outer end rings. The radial spacing is approximately 34 mm. The effect of the holes on the mean rotation profile was not measured. However, the vertical boundaries are already turbulent and any radial circulation should be negligible due to the small flow rates required to relieve the pressure. This was born out by observing the deposition of

an ATF-water emulsion that formed when ATF leaked in to the vessel past a worn seal. The pink emulsion was deposited only between the outer two holes of the upper end ring and along the inner cylinder axle - where it was well separated from the bulk fluid. The surface of the inner cylinder remained free of oily deposits.

3.2   Fluids

The working fluids of the PRINCETON MRI EXPERIMENT are water, water-glycerol mix and a gallium alloy consisting of gallium, indium and tin which is eutectic and liquid at room temperature. The properties of the fluids are listed in Table: 3.2. The kinematic viscosity of water at room temperature is approximately three times that of the gallium alloy. This allows us to evaluate the operation of the experiment and determine its suitability for a search for the MRI in a readily available and easy to diagnose fluid. The water-glycerol mixture allows us to decrease the Re of the experiment to overlap the highest Re achievable in simulations of the experiment.

Table 3.2: Properties of experimental fluids

Fluid	Density $(10^3 \mathrm{kg/m^3})$	kinematic viscosity $(10^{-6} \mathrm{m^2/s})$	magnetic diffusivity $(\mathrm{m^2/s})$	refractive index
water	1.0	1.0	NA	1.33
water(.25)- glycerol(.75)	1.2	15.0	NA	1.43
Ga(.67)-In(.21)-Sn(.12)	6.3	0.3	0.2	NA
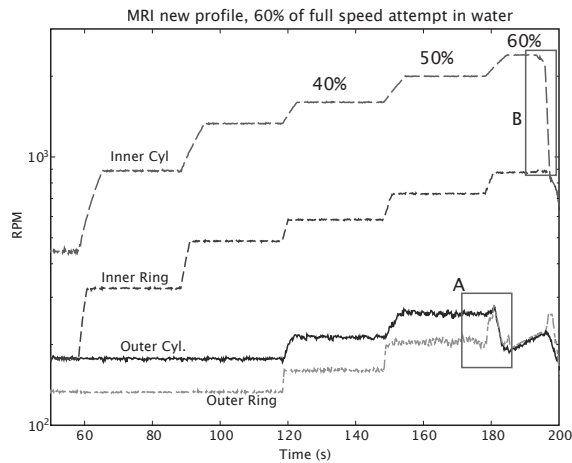
Figure 3.8: Mechanical interference due to dynamic pressure. A: Low pressure above the outer ring causes the ring to be lifted against the outer cylinder top cap. B: High pressure in the ring gap causes a large thrust load on the submerged bearings which exceeds the peak torque of the inner cylinder drive.
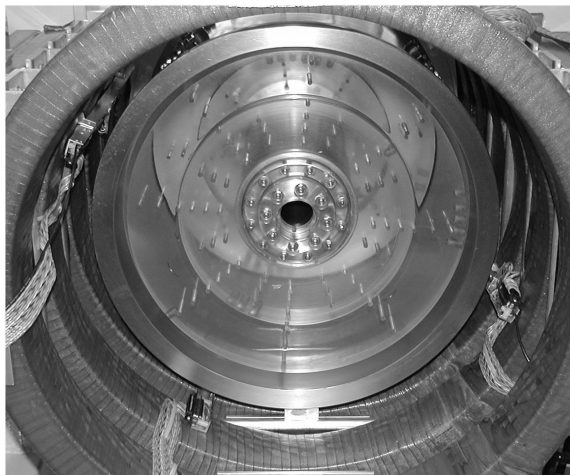
Figure 3.9: Holes drilled vertically through end rings to relieve pressure differential. Also visible are the solenoid coils used to produce the axial magnetic field for MHD experiments, and the mounting brackets of the four pick-up coils array. There is insufficient clearance between the outer cylinder end caps and solenoid coils to accommodate installation of the diagnostic arrays after assembly.

3.2.1   Special considerations for working with GaInSn alloy

When exposed to oxygen liquid gallium forms a protective oxide layer on its surface. If that layer is mixed in to the bulk, the layer will break up and surround smaller amounts of un-oxidized gallium [Morley et al., 2007]. If the process is allowed to progress the result is a spongy metallic sludge. To prevent this from occurring in the PRINCETON MRI EXPERIMENT oxygen levels are kept to a minimum using positive argon pressure in the vessel and a closed-loop transfer system to move gallium into and out of the experiment. The transfer system also includes a weak bath of HCl to recover the gallium which is trapped by the oxides, as well as convert some of the oxides back to pure gallium.

3.3   Stationary Components

3.3.1   Experiment Frame

The experiment frame provide mechanical support for the rotating apparatus, motors and transmissions, seal cooling apparatus, magnet coils and diagnostics. The frame consists of a rectangular Aluminum structure mounted to triangular legs through two bronze bushings. The bushings allow the frame to be rotated on to its side during assembly and disassembly. Either upright or on its side, the frame is prevented from rotating by bolts securing it to the legs. The legs are bolted to the lab floor. In the plane of rotation the frame assembly is stiff enough to resist dynamic loads from the rotating components. Stiffening legs are bolted from the top sides to the floor when running at high speed to damp vibrations perpendicular to the plane of the legs.

3.3.2 Magnet Coils

Six magnet coils surround the experimental volume of the rotating apparatus as shown in Fig: 3.10. The coils are water-cooled multi-turn Copper. The two center coils have 67 turns and the remaining four have 72 turns. The midplane of the solenoid is coincident with the fluid midplane.

The upper three coils are wired in series, as are the lower three. The two series-connected sets are powered in parallel by a 480VAC diode rectifier. The coils are capacitor-bypassed to reduce current ripple from the diode's switching. The total bus current is measured for each experiment shot.

The rectifier current setpoint is determined by an analog voltage generated by the PC. A dead reckoning technique is used to determine the appropriate voltage when a new target current is required.
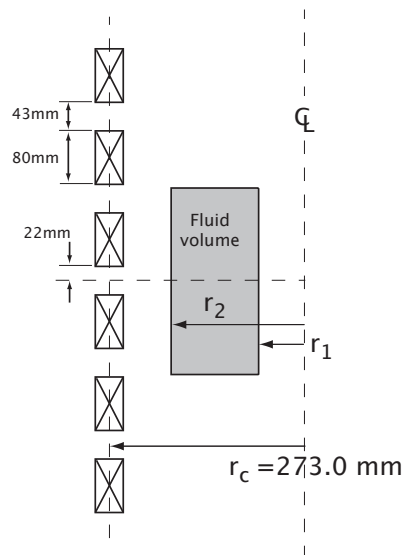
Figure 3.10: Location of solenoid coils relative to fluid experimental volume. The center two coils have 67 turns of 6.3x6.3 mm Cu conductor, the other 4 have 72 turns.

3.4   Drives and Control

Each rotating component is driven by a motor mounted on the experiment frame. Motor specifications and maximum mechanical rotation speeds are given in Table: 3.3. Power transmission is accomplished through combinations of 1/2-inch wide 3/8L timing belts and associated pulleys. Transmission ratios are listed in Table: 3.4.

In the water experiments all four motors were permanent magnet DC type. The inner cylinder was powered by a uni-directional KB Electronics KBCC-225 SCR drive. The time constant of the KBCC-225 was modified to 0.1 s from the stock 0.2 s. The other motors were all driven by KB Electronics KBMG-212D bi-directional SCR drives which have 0.1 s time constants. The drives are run in open-loop mode with speed set via computer-controlled analog voltages. The analog signals are isolated from the PC by KB and KBSI-240D isolators.

For gallium operation, the inner cylinder was upgraded to a 7.5 kW AC motor with a Leeson SM plus Variable Frequency Drive.

Servo control of component speeds is done by a National Instruments PCI-7344 4-axis motion control card. Velocity information is supplied to the motion control card from four 4000 count/rev incremental encoders. The control outputs of the card are analog voltages generated by 16-Bit Digital to Analog Converters (DAC). The full-scale swing of the DAC output is ± 10 V, with a value of 32767 corresponding to $+10$ V. DAC limits can be set in software to match the requirements of the motor drive. For the KBMG drives the allowed input voltage is ± 10 V, $0-9$ V for the KBCC and $0-10$ V for the Leeson. Speed and DAC register values are recorded by the LabView-based experiment control software. The PID loop of the PCI-7344 updates at 5 ms intervals while the response time of the drives 0.1 s. To achieve stable operation of the experiment the PID gain

parameters are set very low (relative to their max).

For each axis, the motion control card calculates a "Following Error" between the current state of the axis and its setpoint. In the MRI experiment the axis velocity is the controlled variable of the servo loop and the Following Error is a time integral of the velocity error. If the Following Error for an axis exceeds an user determined threshold, that loop is terminated ("Killed") and the output DAC is set to zero. This shutdown will always occur when the target velocity is not reached, with one exception. Due to the way the card stores velocities in its onboard registers, the maximum velocity for an axis is subject to the constraint,

$$v \leq (65,536 \times a_{decel}) - a_{accel},$$

where v is the axis velocity in $counts/(sample\ period)$, a_{decel}/a_{accel} is the deceleration/acceleration rate in $counts/(sample\ period)^2$. If the deceleration rate is too low the axis will not achieve its target and will not trigger a Following Error shutdown. More information on this can be found in the National Instruments PCI-7344 user manual.

Table 3.3: Motor mechanical specifications

| | | | Speed ratings | |
Component	Power (kW)	armature voltage (V)	Motor max (RPM)	Component max. (RPM)
Inner cylinder, DC	2.25	180	1750	4112
Inner cylinder, AC	7.5	230	1750	4112
Outer cylinder	0.56	90	2500	833
Inner ring	0 .75	90	2500	2500
Outer ring	0.75	90	1750	700

Table 3.4: Pulley ratios for the MRI experiment drives

Component	Pulleys				Ratio
	Motor	Int. 1	Int. 2	Axle	
Inner cylinder	40	17	40	38	2.35
Outer cylinder	16	NA	NA	48	0.33
Inner ring	45	NA	NA	45	1.00
Outer ring	24	60	60	60	0.40

3.5 Diagnostics

3.5.1 Laser Doppler Velocimetry

The opacity of liquid metals severely constrains the choice for non-invasive diagnostics for measuring flow velocity.

Because of the difficulty of measuring flow velocities within a liquid metal where optical techniques are not available, we decided to characterize the hydrodynamic operation of the apparatus and benchmark the simulations using Laser Doppler Velocimetry (LDV). Most of the measurements were made using a Dantec Dynamics Flow-lite two-component model. The unit was rented from Dantec four times between August of 2005 and June of 2006.

The first two data runs with the Dantec instrument were used to measure the mean velocity profile to determine the effect of the choice of component speeds, and its scaling with Re (see Chapter: 4). During the last runs the instrument was used in coincident mode to measure radial as well as azimuthal velocities. This provided a direct measure of the Reynolds stress, allowing us to rigorously determine the presence of subcritical instability [Richard and Zahn, 1999], see Section: 4.4.1.

Orientation of the LDV diagnostics relative to the experiment are diagrammed in Figure: 3.11. The inner cylinder was painted black to prevent reflections from

interfering with the measurement.
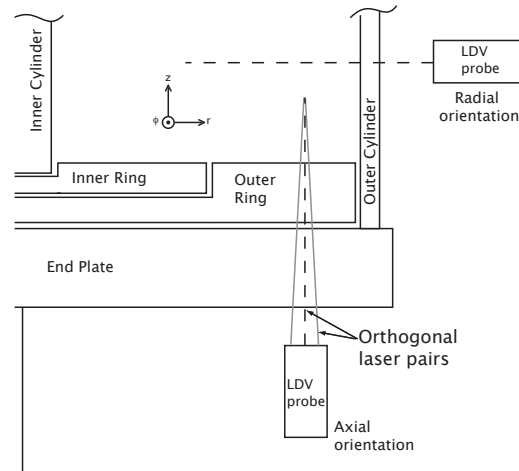
Figure 3.11: Orientations of LDV diagnostics used in the hydrodynamic experiments. In the axial orientation, 2 components of velocity were measured: $\hat{r}$ and $\hat{\phi}$.

Principle of Operation

LDV [Albrecht et al., 2003] uses coherent scattering of laser light from tracer particles in a fluid to obtain a measurement of the flow velocity. The measurement for a single velocity component is diagrammed in Fig. 3.12. A laser beam is split into two components which are then focused to interfere coherently in a region called the measurement volume, diagrammed in Figure: 3.13. A tracer particle traversing the measurement volume with a velocity perpendicular to the beam bisector will reflect a Doppler burst back to the collecting optics.
The burst is the beat frequency between the reflections ofthe two component laser beam reflected from a particle of velocity $\mathbf{v_p}$. For the geometry in Figure: 3.13, the reflected beam frequencies are Doppler-shifted:

$$f_b \approx \frac{\mathbf{v}_p \cdot \hat{\mathbf{k}}_i}{\lambda_b} \qquad (v \ll c, c = \lambda_b f_b),$$

where the beam is incident with frequency f_b and wavelength λ_b, $\hat{\mathbf{k}}_i$ is the propagation unit vector of the i-th beam, i = 1 or 2. The difference frequency of the two reflected beams is:

$$\Delta f = \mathbf{v}_p \cdot \frac{\hat{\mathbf{k}}_1 - \hat{\mathbf{k}}_2}{\lambda_b}. \tag{3.1}$$

The velocity of the particle perpendicular to the beam bisector is simply the product of the difference frequency with the fringe spacing of the interfering beams:

$$\mathbf{v}_{p\perp} = \Delta f \cdot d_{\text{fringe}},$$

Where $d_{\text{fringe}} = \lambda_b/|\hat{\mathbf{k}}_1 - \hat{\mathbf{k}}_2|$

Because the cosine is even about the origin, only the magnitude of the particle's velocity is measured. To obtain the direction of propagation, an offset frequency may be introduced on one beam. Dantec uses a Bragg cell to do this.

The Doppler burst is focused on to an optical fiber and sent to a photo-multiplier tube. The Dantec system continuously samples the detector voltage and writes it in a round-robin fashion to buffers in a dedicated Burst Processor. A burst is detected by continuously fitting for a DC envelope. When one is detected, the envelope is subtracted out and the autocorrelation of the remainder is used to determine the Doppler frequency. This method of detection requires no filtering of data during analysis. The transit time of the tracer particle through the measurement volume is obtained from the fit to the DC envelope.

The Flow-lite uses two lasers of different colors (red and green) to measure two orthogonal velocity components. In Figure: 3.12, the second laser pair is oriented in the plane perpendicular to the page. The two velocities can be measured in a coincident mode where a valid measurement is generated only if a Doppler burst for each laser occurs within a small time window. The window for our correlation measurements was of order $10~\mu s$.

The Dantec probe head is mounted on a 3-axis traversing stage which is controlled by the diagnostic software.

Calibration

Fringe spacing, d_{fringe}, and propagation angle, θ_i, are constants internal to the LDV measurement. No calibration of the velocity is required if the beams pass normally through a window of constant index of refraction. This is because the index of refraction appears in both the numerator and denominator of Equation 3.1. The curved surfaces of the outer cylinder introduce position dependencies in to the velocity measurement.These must be corrected as well as the radial location of the measurement volume which is, in general, a function of the changes in refractive index through which the beams travel.

Calibration for radially-acquired data

For profiles that were acquired with the probe head mounted radially, the beams measuring azimuthal velocity pass through the curved surface of the acrylic (with index of refraction of 1.49) outer cylinder as diagrammed in Figure: 3.11. The curvature causes a change in beam angle of incidence as the probe head is scanned radially. The beam bisector is centered on the experiment axis of rotation and the beam separation is small compared to the outer cylinder radius, $d_b/2 \ll r_2$, therefore the derivative of θ_i with radius is approximately small and constant. Calibration of the data then involves linear corrections to radial location and velocity.
Solidbody rotation is used for the calibration process because as long as the fluid has been given sufficient time to equilibrate with the cylinders, the velocity profile is known a priori:

$$v(r) = \Omega r. \tag{3.2}$$
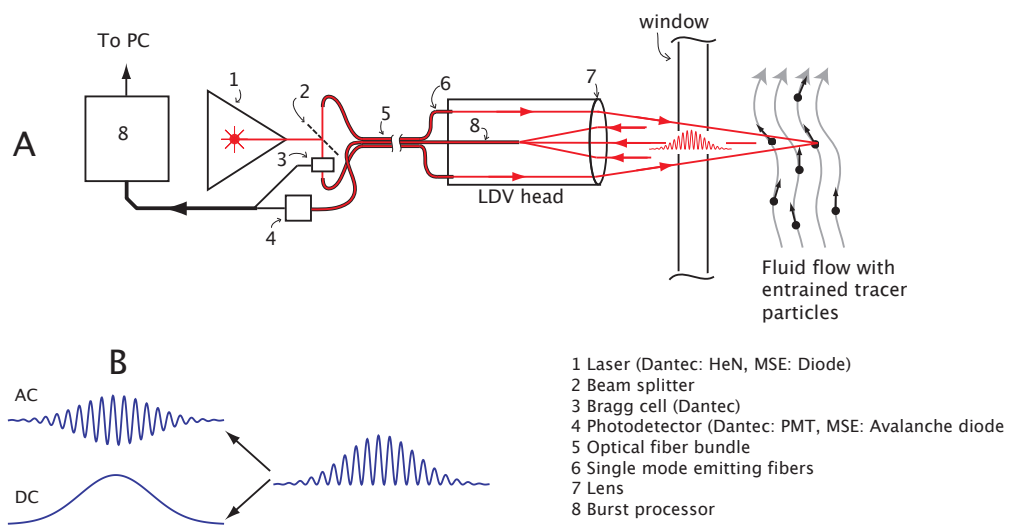
Figure 3.12: A: Components of a 1D-LDV measurement. B. Decomposition of the Doppler burst into AC and DC components.
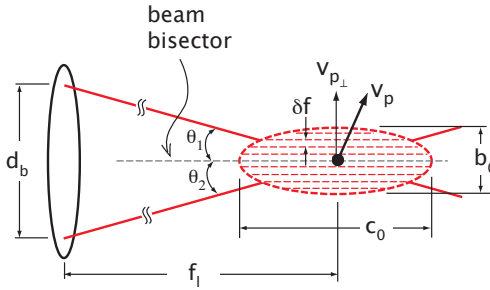
Figure 3.13: Measurement volume defined by the region of interference of two Gaussian laser beams.

Figure: 3.14 diagrams the determination of calibration parameters. The calibrations for velocity and radius commute, but velocity correction requires a calibrated radius, which we do not have. Therefore, the radial calibration is performed first. Assuming the derivative of the radial error approaches zero as the measurement volume approaches r_2, the correct location of the i-th measurement is:

$$r_i = r_2 - (y_2 - y_i) \cdot \frac{r_2 - r_1}{y_2 - y_1}, \tag{3.3}$$

where $y_1(y_2)$ is the location of the inner(outer) cylinder in the traverser coordinates.

The cylinder walls are located by scanning the measurement volume across them, see Figure: 3.15. As the inner cylinder enters the measurement volume the large reflective area causes a jump in the data rate which peaks at the center of the volume and goes to zero when the beams are interrupted before they intersect. The beam intensity is Gaussian and the number of scatterers on the surface is approximately constant, therefore as long as the data rate is not limited by the burst processor pipeline the count rate is also Gaussian. The data rate and fit to it are plotted in Figure: 3.16 for the October 2005 experiments. The mean is the location of the inner cylinder and the length of the measurement volume is given

by the FWHM. For the data shown r_1 is located at $y_1 = 4.2$ mm with a radial extent of $c_0 = 1.7$ mm. More details can be found in Appendix: A.

For the Flow-lite unit, the data rate is limited by laser intensity which was less than 3 mW. Near the inner cylinder the intensity is such that the data rate is less than 1 Hz. As the probe volume is scanned outward from the inner cylinder, the data rate increases exponentially as fewer photons are lost due to scattering. When the edge of the probe volume overlaps the outer cylinder the data rate follows a new exponential curve. On the log-linear plot of Figure: 3.15 the intersection of the two scalings shows the location of the outer cylinder at $x_2 = 120.5$ mm $+ 2c_0/2 = 121.3$ mm.

Applying the radius correction to the raw data yields curve 2 of Figure: 3.14A. A least-squares fit to this line is used,

$$\chi^2 = \sum_{i=1}^{N} \left(\frac{v_{meas,i} - (a + br_i)}{\sigma_i} \right)^2,$$

to determine the coefficients a, b from $r_i, v_{meas,i}$. Then, by Equation 3.2, the calibrated velocity is,

$$v(r) = v_{meas} \frac{\Omega_{sb} r}{a + br}. \tag{3.4}$$

The solidbody data calibrated by this method is shown in curve 3 of Figure: 3.14A. The upper limit for the runout was estimated from time series LDV data acquired near the inner cylinder. During a calibration run, the measurement volume slightly overlapped the inner cylinder. As the high spot swept through the volume, the data rate changed substantially. The high and low data rates are marked on Figure: 3.16 by the horizontal bars. The horizontal distance between the intersections of the bars with the fit data-rate profile indicate that the runout is a maximum of 0.76 mm.
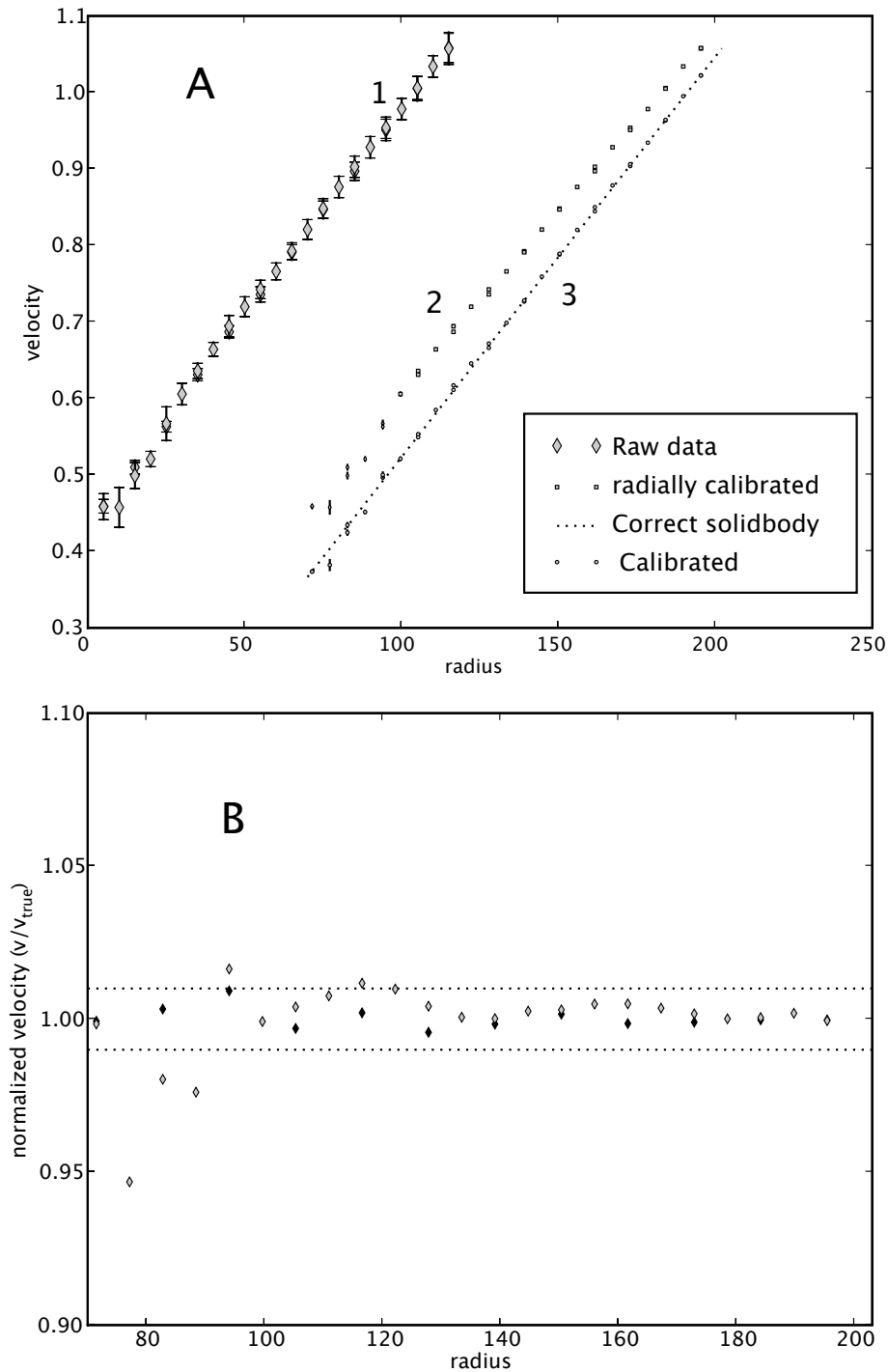
Figure 3.14: A. Steps employed to calibrate radius and velocity for radially-acquired LDV data at a height of 76 mm. *N.b.* during set-up of the diagnostic, the approximate location of the inner cylinder in the traverser coordinates was set to 0. B. Residual error after application of the calibration routine to the two radial scans used to perform the calibration. The large variance at the interior points are due to low count numbers. Dotted lines are at $\pm 1\%$.
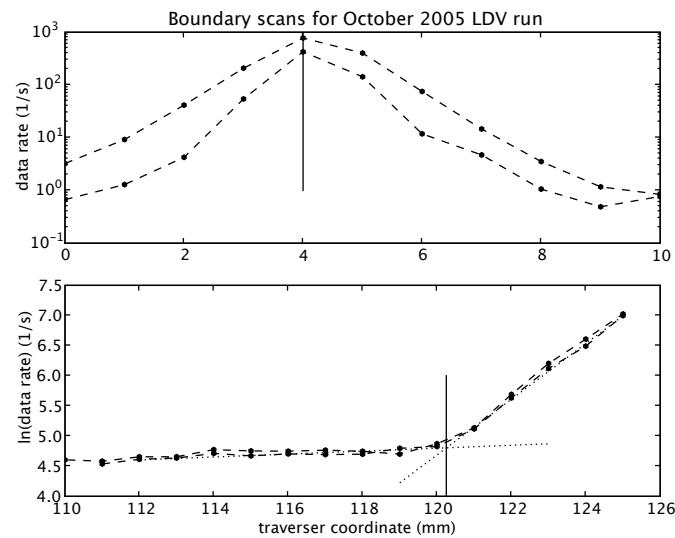
Figure 3.15: Location of cylinder walls in October 2005 data. Vertical solid lines indicate location of wall. Upper plot: the peak occurs when the inner cylinder wall is at the center of the measurement volume. Lower plot(needs correct y-axis label): the break in scaling indicates the outer cylinder wall has entered the edge of the measurement volume.
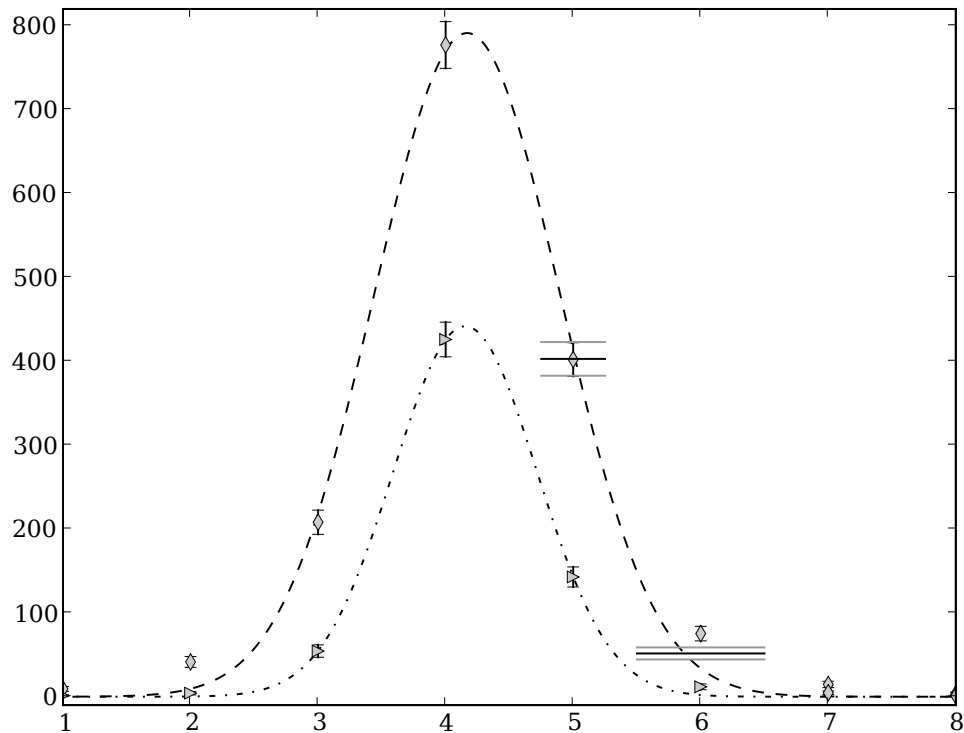
Figure 3.16: Scanning the LDV measurement volume across the inner cylinder wall provides a measurement of the wall's location in the traverser coordinates (abscissa). The data rate (ordinate) is proportional to the intensity of the lasers. The data rate is fit to a Gaussian, dotted line. The horizontal bars were used in a measurement of the run-out of the inner cylinder.

Calibration for axially-acquired data

It was originally assumed that in the axial orientation, the velocity data would not require correction because the flat surface of the end cap and the probe head's normal orientation would allow the index of refraction effects to cancel out. In turned out to be the case that a constant velocity offset was present in this orientation: most likely due to an axial misalignment of the probe head. Angular misalignment was less than $1°$ and cannot account for the magnitude of the offset. Furthermore, the measurement of radial position of the probe head was unreliable, so solidbody data could not be used for calibration. To correct the velocity and position in this orientation relies upon the velocity profile for the experiment running in the `Ekman` configuration where the end caps co-rotate with the outer cylinder, see Chapter: 4. The procedure is diagrammed in Figure: 3.17. Over the outer ring, the Ekman profile features a knee where solidbody-like velocities near the outer cylinder transition to shear flow driven by the inner cylinder. The profile is radially translated, and a constant offset added to the velocity to align the linear portions of the data.

The result published in [Ji et al., 2006] using the original calibration states that the data was acquired at a radius of 170 mm. The correct radius is 179 mm. The essential results are independent of the magnitude of velocity and remain valid as published.

3.5.2 Errors in LDV measurement

Particle entrainment and fluid loading

LDV is a reliable estimator of a fluid velocity if the tracer particles are well coupled to the flow. A particle is considered to follow the fluid flow exactly when the ratio of particle to fluid timescales is smaller than 0.01 [Rogers, 1991]. This
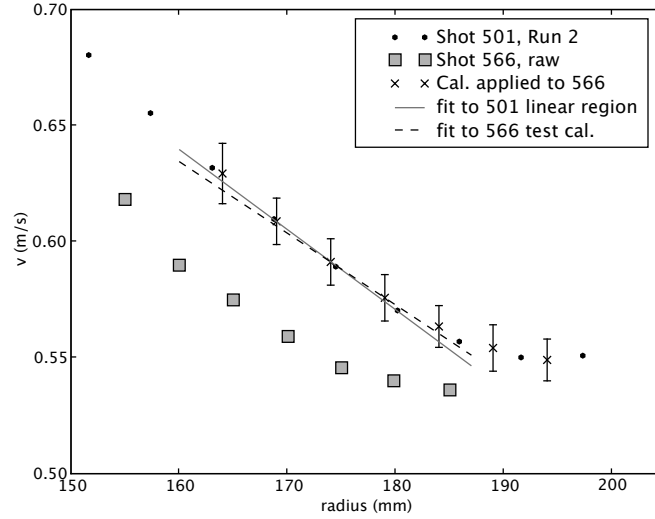
Figure 3.17: An Ekman profile is used to calibrate the radial location and velocity offset of LDV data acquired in the axial orientation.

ratio is the Stokes number,

$$\text{Stokes number } = \frac{\tau_p}{\tau_f}, \tag{3.5}$$

where subscript "p" refers to the particle and "f" is the fluid. For the PRINCETON MRI EXPERIMENT the LDV seed particles are silver-coated hollow glass beads supplied by Potters Industries Inc. The beads have an average diameter, $d_p = 15~\mu$m and average density of $\rho_p = 1.6~\text{gm/cm}^3$. For Stokes drag, a particle timescale is:

$$\tau_p = \frac{\rho_p}{\rho_f} \frac{d_p^2}{18\nu}, \tag{3.6}$$

where ν is the kinematic viscosity of the fluid. Using this formula, the particle timescale for our seed particles is $\sim 10^{-5}$ s. For a choice of fluid timescale based on either viscosity or Ekman effects, $\tau_f \geq 1$ s and the Stokes number satisfies the entrainment criterion.

The particle mass loading is defined as the ratio of particle mass flux to fluid mass

flux through a given volume. It is possible for the particle loading to alter the properties of any turbulence that may be present if it exceeds about 1% [Rogers, 1991]. The fluid volume between the cylinders is $\approx 3 \times 10^7$ mm^3. The volume of seed particles added to the flow was not well controlled but did not exceed 20 mm^3. Therefore there is no impact on the fluid flow due to the presence of the particles.

Errors for radially acquired LDV

The errors in the radially acquired LDV data are dominated by the optical defects of the outer cylinder. The index of refraction of acrylic changes with local stress and also the cylinder has a substantial deviation from circularity. Without careful *in situ* measurements it is not possible to determine which of the two effects is more important. They affect the data by introducing deviations into the propagation vector, $\mathbf{k_b}$. Each deviation adds an offset to some number of samples taken from the Gaussian velocity distribution inherent to LDV. By the Central Limit Theorem, for a large enough number of samples the noise distribution will also tend to a Gaussian which must be wider than that of the true LDV measurement. A plot of the distribution of velocity measurements for a solidbody profile is shown in Figure: 3.18.

In addition, defects at different spatial separations on the cylinder wall contribute to the error as the probe is scanned radially. There is no reason to assume that the acrylic defects maintain the linear corrections to radius and velocity that are the foundation of the calibration procedure described above. However, insufficient data was acquired to characterize fully the solidbody data's deviation from a line. The calibration averages over solidbody data acquired at several axial locations to produce the constants used in Equation 3.4.
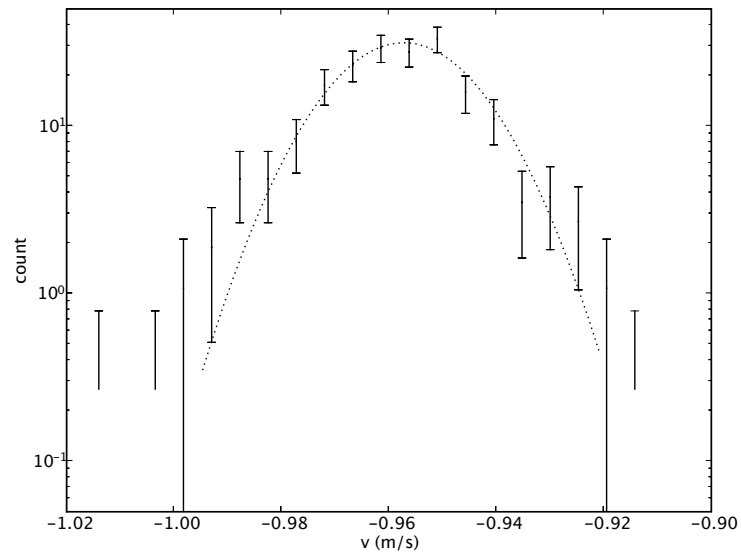
Figure 3.18: Probability distribution of raw velocity measurements for a solidbody flow profile. The error bars are $\sqrt{n}$, where n is the number of samples in a velocity bin. The dashed line is a Gaussian fit to the data. Optical defects in the acrylic outer cylinder wall cause individual Doppler bursts to be shifted by an arbitrary amount.

Errors for axially acquired LDV

Like the radial data, the axially acquired velocities also suffer from distortion due to acrylic defects. The effect of broadening the distribution and introducing extreme outliers is nearly identical to that shown by Figure: 3.18. The effect of the optical defects could have been to decorrelate v_r and v_ϕ. If this were the case the effect would have been extremely difficult to correct for, or even measure. Solid body rotation has no gradient of angular velocity and therefore the velocity correlations are identically zero. In this case, decorrelation by optical defects would have mapped zero onto zero. Instead we found that solid body rotation had non-zero correlation. This offset was used to correct correlations in flows with non-zero shear.

Errors associated with flow properties

It is possible for the flow properties to introduce errors into the LDV measurement [Albrecht et al., 2003]. In particular, a velocity gradient along the length of the measurement volume will broaden the spread of velocity:

$$\Delta v = \nabla v \cdot c_0,$$

where c_0 is the length of the measurement volume, see Figure: 3.13. The maximum shear in the absence of turbulence occurs at r_1 on the Rayleigh stability boundary: $\partial v_\phi / \partial r = -br^{-2}$. For 10% flow at the mid-radius $\Delta v / \bar{v}_\phi$ is expected to be 1.3%, for solid body rotation we measure $\sigma_{v_\phi} / \bar{v}_\phi \approx 1.3\%$. Therefore spreading due to the velocity gradient is less than the spreading due to optical defects.

Error estimation

The total velocity error involves both systematic and random errors. By shifting and broadening the measurement distribution, the acrylic defects are the

dominant contributor to both errors. From Figure: 3.18B, after calibration the systematic error is less than 1% over most of the experimental volume. This calibration error is not affected by the number of samples in a measurement. The distribution of a measurement is broadened by the defects, but the error on the estimate of the mean is still reduced by increased sample size. The combination of the two error sources gives an estimate for the error on a measurement of a mean quantity:

$$\sigma_{total} = \sqrt{\sigma_{random}^2 + \sigma_{systematic}^2}, \tag{3.7}$$

where $\sigma_{random} = \sigma_v/\sqrt{n}$. Here, σ_v is the standard deviation of velocity distribution and n is the number of samples in the measurement.

For the correlation experiments, the systematic error appears as an offset which can be eliminated by subtracting the correlation measured for solidbody rotation. In this case we are left with only the random error associated with estimating distribution properties from a finite sample population.

3.5.3   Magnetic Diagnostics

Magnetic Pick-up Coils

When the MRI is destabilized by an appropriate applied solenoidal field, its signature is the amplification of radial and azimuthal fields. In the experimental apparatus fluctuations of the radial component of the field will propagate external to the outer cylinder and may be detected with diagnostics fixed to the experiment frame. The simulations by Liu [Liu, 2007] for rotation at 45% of full speed indicate that during the linear growth phase of the MRI, the radial field component at the radius of the solenoid coils will have a time derivative on the order of $0.1 \ \mathrm{G/s}$ with a maximum amplitude of order $1 \ \mathrm{G}$. Pick-up coils were chosen to measure this field for two reasons: 1) they are insensitive to the DC

portion of the applied magnetic field. 2) because of reason 1, the coils do not need to be precisely aligned - which would be extremely difficult to do in the confined space between the outer cylinder and solenoid coils.

A photograph of a magnetic pick-up coil is shown in Figure: 3.19. There are 39 localized coils formed of 400 turns 36 gauge Cu wire on 7.6 mm diameter fiberglass bobbins. They have an average effective area of 0.014 m^2 and resistance of 20Ω. The effective areas were measured using a Helmholtz coil driven by an audio amplifier. A typical calibration curve is shown in Figure: 3.22. The arrangement of the coils around the fluid volume is diagrammed in Figure: 3.20. In addition to the small pick-up coils a saddle coil with an effective area comparable to the localized coils was wound on a 25 mm wide Kapton tape. This coil was wound around the inner diameter of the solenoid coils, on the experiment midplane. The effective area of the saddle coil is estimated to be 0.01 m^2. The coil is largely immune to non-axisymmetric effects but is not circular enough to completely eliminate them.

3.5.4   Pick-up coil amplifiers

To maximize the signal-to-noise ratio of the pick-up coil measurement each signal is amplified before transmission to an Analog to Digital Converter (ADC) in the PC. Figure: 3.23 shows the output of a prototype coil-amplifier combination. The amplifier has a gain of 1000 and passband of DC – 15 kHz which is well above the roll-off of the pick-up coil. The signal is dominated by ripple currents in the solenoid coils at 60, 120, and 360 Hz.

To reduce sensitivity to the ripple currents and add the possibility of using gains higher than 10^3 a filter-amplifier was developed around the Maxim MAX7401[url] 8th-order switched-capacitor Bessel filter. The circuit diagram for the filter is
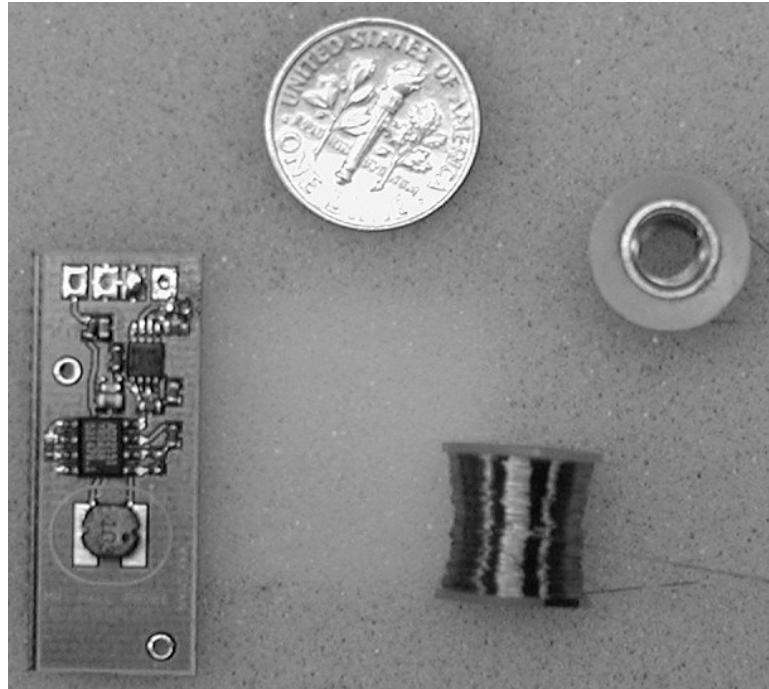
Figure 3.19: Left: Hall probes, Right: Pickup coils
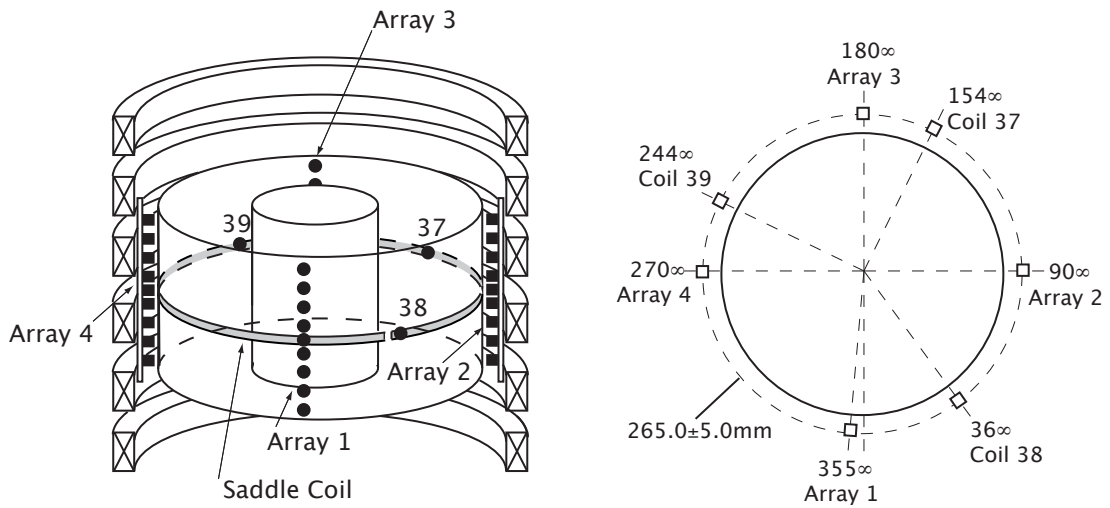
Figure 3.20: Arrangement of magnetic pick-up coils. 36 localized coils are mounted on 4 vertically-oriented arrays. Three additional coils are located on the experiment midplane at the indicated azimuthal angles.
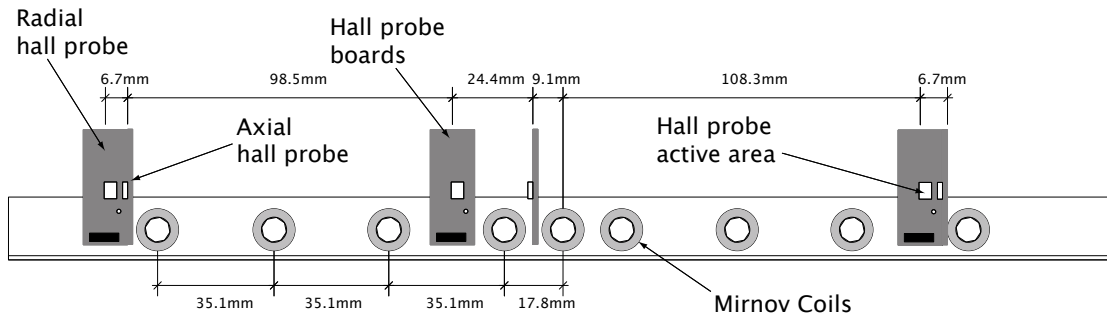
Figure 3.21: Location of localized pick-up coils and Hall probes. Nine pick-up coils are distributed vertically along the array. The full Hall probe array shown here is only implemented on Array 2. Array 4 has Hall one axial and one radial Hall probe mounted identically to the middle two probes.
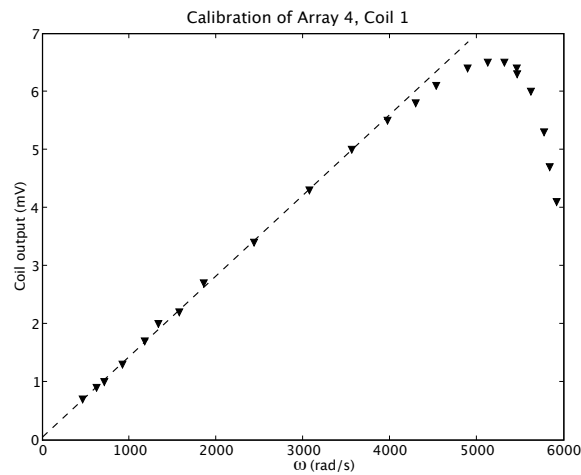
Figure 3.22: Calibration data for pickup coil array #4, coil 1. The dashed line is a fit to the linear portion of the curve, yielding the effective coil area. A Helmholtz coil was used to provide a spatially-uniform magnetic field which oscillated sinusoidally with frequency ω., the amplitude of the applied field is approximately 5 G.

shown in Figure: B.1. The MAX7401 is a single-supply filter with a clock-selectable knee-frequency ranging from 1Hz to 5kHz. The pick-up coil signal passes through an Analog Devices AD622 instrumentation amplifier with a gain of 100. The output of the AD622 is referenced to $+2.5$ VDC to accommodate the filter's input voltage requirements. The filter output is sent to another AD622 with a gain of 10, and a ground-referenced output. The gains of the AD622s are resistor selectable up to a gain of 1000, each. The selected gain of 1000 was chosen as a good balance between sensitivity and dynamic range.

The data acquisition card in the PC is used to generate the clock signal for the filter. The clock frequency is software selectable for each experiment shot. The knee-frequency of the filter is the -3 dB point and its relation to the clock is $f_{knee} = f_{clock}/100$. The filter-amplifier performance on a low frequency test signal is shown in Figure: 3.24

Hall Probes

Eight Hall probes measure the applied field. Six Hall probes are vertically positioned as diagrammed in Figure: 3.21. An additional two probes are located $180°$ from the others. Four Hall probes are oriented measure the vertical magnetic field with a range of about 6 kG. The other four are radially oriented with a range of ± 1 kG. Calibration of the Hall probes mounted in the MRI experiment was performed against a Gaussmeter.
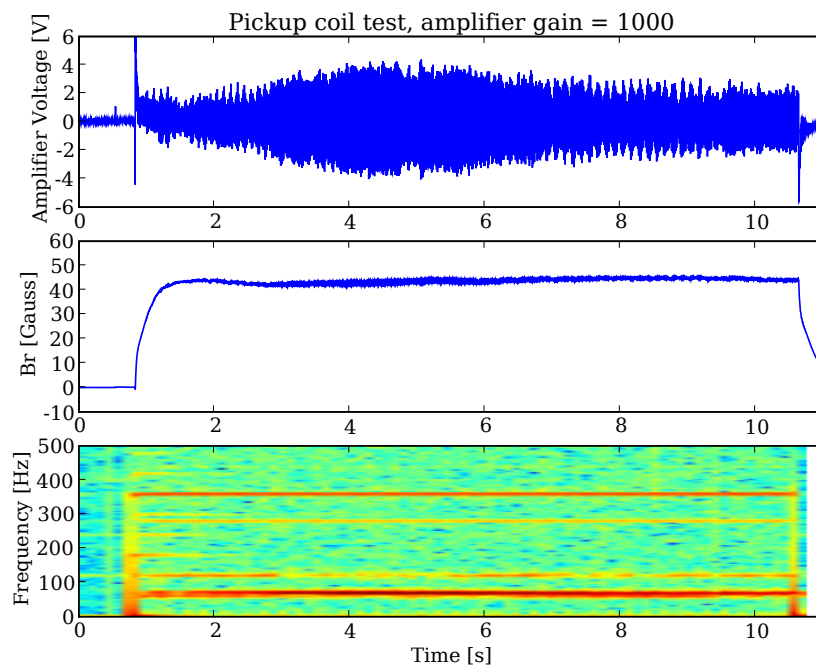
Figure 3.23: Output of Pickup coil after being amplified by 1000, sampled at 1 kHz. No filtering has been done. Strong signals at 60, 120, and 360 Hz are due to rectifier current ripple on the solenoid coils.
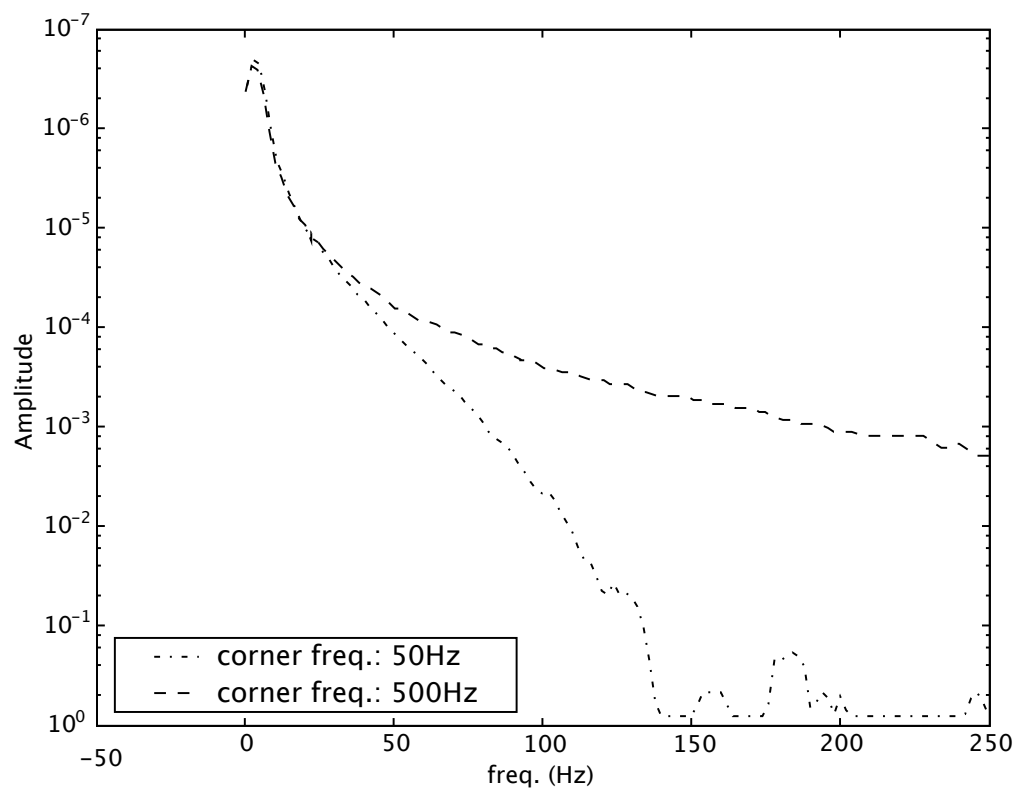
Figure 3.24: Amplification by the filter-amplifier of a low-frequency square wave for two clock frequencies.

Chapter 4

Hydrodynamic Experiments

The hydrodynamic experiments were conducted with a Dantec Flow-lite LDV system between August 2005 and June 2006. The current apparatus was designed to achieve a better approximation of ideal circular-Couette flow than the prototype. The initial experimental goals were to meaure the success of the new design in approximating the ideal flow. The measurements consisted of the radial profile of angular velocity, and its scaling with Reynolds number.

Measurements of the radial profile of mean azimuthal velocity, $\bar{v}_\phi(r, z)$, under the action of differentially rotating end rings were first reported by Burin [Burin et al., 2006]. These results confirmed that the split end-ring design reduces the impact of Ekman circulation on the bulk flow. We also inferred from the small fluctuation levels, $\sigma_{v_\phi}/\bar{v}_\phi \sim 1 - 2\%$, there was no evidence of vortices driven by residual boundary circulation.Such vortices were predicted by simulations which had been highly successful in matching the qualitative flow properties of the prototype experiment[Kageyama et al., 2004]. In addition, we found no evidence of a Stewartson layer forming near the gap in the end rings, as was predicted by Hollerbach and Fournier[Hollerbach and Fournier, 2004].

After optimization of the end ring speeds, the mean profile was found to be a

significantly better approximation of the ideal circular-Couette solution than the simulations predicted. Based on the simulations we expected the end rings to disrupt the apparatus-filling two-cell structure of the Ekman circulation. The residual Ekman circulation would then produce multiple smaller cells within the flow.

Combined with the vertical access for optical diagnostics and a two-component LDV system we saw that we could make a direct measurement of the $\hat{\phi}$-$\hat{r}$ component of the Reynolds stress tensor. The hydrodynamic experiments were therefore extended to look for evidence of Subcritical Hydrodynamic Instability (SHI) in quasi-Keplerian flows. Prior to this the work of Richard [Richard, 2001] was the only experimental investigation of the stability of quasi-Keplerian flows near (but below) the Rayleigh stability line. Richard observed a qualitative change in the flow using a Kalliroscope imaging method and also a jump in fluctuation levels of v_ϕ using single-component LDV. From these he inferred that a hydrodynamic instability was present.This was interpreted as corroborating the estimate by Richard and Zahn[Richard and Zahn, 1999] of astrophysically relevant angular momentum transport due to SHI. That estimate, in turn, was based on the torque measurements of Wendt[Wendt, 1933] and Taylor[Taylor, 1936] in the cyclonic regime. The flexibility of the MRI apparatus, combined with the precision and the non-invasive nature of LDV provided us with a unique opportunity to directly perform a sensitive transport measurement in the quasi-Keplerian regime while able to distinguish effects due to the vertical boundaries.

Finally, an unambiguous observation of the MRI requires detailed knowledge about the hydrodynamic state of the background flow in which we wish to observe it. The required knowledge consists of a measurement of the radial profile of mean azimuthal velocity, the scaling of that profile with Re, and the presence

of boundary flows which may interact with the applied magnetic field to obscure or suppress the MRI. The set of experiments with the Dantec LDV provided us this detail at sufficient precision to make a detection of the MRI unamiguous.

4.1 Profile nomenclature

For a given ratio of inner cylinder to outer cylinder speeds Ω_1/Ω_2, a wide range of flow properties can be established through the choice of end ring speeds. These flows are not well parameterized by the common dimensionless numbers employed for discussion of rotating flow. Therefore, we employ an *ad hoc* naming convention to distinguish the profiles. Table:4.1 lists the component speed ratios relative to Ω_2 for centrifugally-stable anticyclonic flows. `Ekman` refers to the configuration in which both rings rotate with the outer cylinder. In the `Split` configuration the inner ring rotates with the inner cylinder , and the outer ring rotates with the outer cylinder .

The `Ekman` configuration was chosen to benchmark the apparatus' performance against hydrodynamic simulations which were successful in modeling the prototype experiment [Kageyama et al., 2004]. The split configuration was chosen in order to make a comparison to previous circular-Couette experiments in which angular momentum transport was studied. Those experiments include Wendt [Wendt, 1933], Taylor [Taylor, 1936] and Richard [Richard, 2001]. The `Keplerian` profile is chosen to approximate the $q = -\partial \ln \Omega / \partial \ln r = 1.5$ flow of accretion disks. `MRI` labels the configurations with ring speeds optimized such that the flow is most likely to be unstable to the MRI, $q \sim 1.9$ while not centrifugally unstable. `Solidbody` refers to the flow profile with zero angular velocity shear, which provides a baseline from which calibration and interpretation of velocity measurements are made. Centrifugally unstable and

marginally stable profiles are abbreviated by `CUS` and `MS` , respectively. Throughout the remainder of this thesis, flow profiles will be referred to by the profile configuration followed by the outer cylinder speed as a percentage of the full-scale speed , *e.g.* "`MRI` 10%". The process of determining the optimal ring speeds for the `MRI` configuration was iterative. When referring to alternate configurations, the iteration number will be appended, as in "`MRI` a0 10%". Reynolds numbers of the profiles used in the hydrodynamic experiments are diagrammed in Fig:4.1. Wendt[Wendt, 1933] and Taylor's[Taylor, 1936] observations of enhanced torque at large Re were made along the horizontal axis of the figure, where the inner cylinder is at rest. In our apparatus observations in this cyclonic circular-Couette regime are difficult to interpret due to the sensitivity of the profile to end ring speeds. In addition cyclonic flows are of limited relevance to accretion disks and those experiments will not be discussed herein.

Table 4.1: Component speeds used to produce various flow profiles. Speeds are listed as a fraction of the outer cylinder speed, Ω_2. $\Omega_{2,max}$ is the maximum rotational velocity of the outer cylinder, given in radians per second. The `Ekman` and `Split` configurations do not have a well-defined $\Omega_{2,max}$ because the maximum speed is limitied by power dissipation in the seals. The experiment has a mechanical maximum speed of $\Omega_1 = 418.9$ rad/s and $\Omega_2 = 55.8$ rad/s. To date the highest speed tested is 60%.

Profile name	Ω_1	Ω_3	Ω_4	Ω_2	$\Omega_{2,max}(rad/s)$
`Ekman`	7.50	1.00	1.00	1.00	n/a
`MRI`	7.50	2.74	0.77	1.00	55.8
`MRI a0`	7.50	3.60	1.22	1.00	55.8
`Split`	7.50	7.50	1.00	1.00	n/a
`Keplerian`	5.91	2.48	1.09	1.00	55.8
`Solidbody`	1.00	1.00	1.00	1.00	55.8
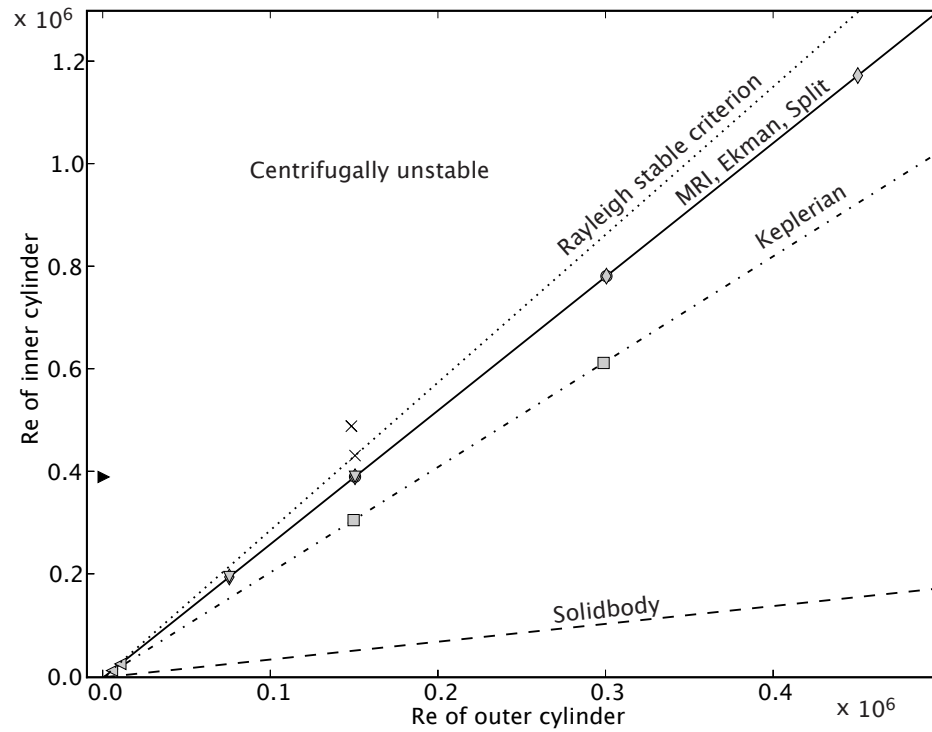
Figure 4.1: Rotation profiles used in the hydrodynamic experiments. Reynolds numbers of the cylinders are $Re_{cyl} = \Omega_{cyl} r_{cyl} \Delta R / \nu$, where $\Delta R = R_2 - R_1$. The configurations are squares: `Keplerian` , diamonds: `MRI` , circles: `Ekman` , downward-triangles: `Split` , leftward-triangles: `MRI` with glycerol mix, cross: marginal and centrifugally unstable with outer cylinder rotating, filled rightward triangle: centrifugally unstable with the outer cylinder at rest. Solidbody profiles (not shown) were used for calibration.

4.2 Study of radial profile of azimuthal velocity

4.2.1 Profile control via end rings

Radial scans of profiles which are globally stable to the Rayleigh criterion are plotted in Fig:4.2. The figure compares the `Ekman` ,`MRI` and `Split` configurations. The scans were performed at the apparatus quarter-height, $0.25h = 76mm$, measured from the top surface of the lower end ring. For each profile the measurement volume at the point $r = 71.9mm$ is overlapping the inner cylinder and should be interpreted as a measurement of the boundary speed. The ideal circular-Couette solution for 10% in our geometry is plotted as the dotted line. No fit has been attempted in this figure.

Surprisingly, the `Ekman` configuration produces a flow in which the azimuthal velocity has everywhere a negative radial gradient . This is in contrast to the profiles of both the prototype experiment [Kageyama et al., 2004] at $(\eta \equiv h/\Delta R \sim 1$, where h is the cylinder height) and Richard [Richard, 2001] $(\eta \sim 25)$. Those experiments , at smaller and larger aspect ratio, respectively, feature a radius at which $\partial v_\phi/\partial r$ changes sign for the `Ekman` configuration. This transition indicates a region of the flow which rotates rigidly with the outer cylinder.

The split configuration cannot be compared with the prototype because that apparatus was only able to operate in the `Ekman` style. Richard found (see Fig: 4.2 of *Ibid.*) that the split style eliminated the change in sign of $\partial v_\phi/\partial r$, though a zero does appear at a radius two-thirds across the experimental volume, $r - r_2 \simeq 0.6d$. In our split configuration $\partial v_\phi/\partial r$ does change sign, but $\partial \Omega/\partial r < 0$ everywhere which satisfies the criterion for producing the MRI. However, there are substantial secondary circulations driven by the boundaries, including a centrifugally unstable layer which must exist between the point measured near

$195mm$ and the outer cylinder . Boundary layers and secondary circulation will be discussed in Sections 4.2.4 and 4.4.1.

The `MRI` profile is the sixth iteration attempting to minimize the difference between the ideal circular-Couette and the measured azimuthal velocity profiles. Fine tuning of the profile is demonstrated in Fig:4.3. The initial attempt, a0, was obtained through a trial and error optimization process using the simulation of Kageyama *et al* [Kageyama et al., 2004].

Table 4.2: Fit to circular-Couette Profiles for `MRI` and `Ekman` 10%, $\Omega_{1,2}$ are fitting parameters.

Configuration	radial interval	Ω_1 RPM	Ω_2 RPM	χ^2/dof
MRI	72–200	403.0	51.6	2.2
Ekman	72-195	358.1	49.7	5.7

Table 4.3: χ^2 for alternate `MRI` 5% profiles plotted in Figure:4.3. The inner (outer) ring angular velocity $\Omega_3(\Omega_4)$ is listed as a ratio to the outer cylinder speed.

Configuration	Ω_3/Ω_2	Ω_4/Ω_2	χ^2/dof
MRI	2.74	0.77	2.4
MRI a0	3.41	1.24	148.5
MRI a1	3.00	1.12	28.2
MRI a2	2.81	1.05	17.0
MRI a3	2.62	1.00	6.1
MRI a4	2.62	0.77	3.7
MRI a5	2.81	0.77	2.8

4.2.2 Reynolds scaling of mean profile

MHD experiments with the GaInSn alloy will be initiated without a velocity diagnostic. The kinematic viscosity of the alloy is about one-third that of water. Due to the speed limitations of the motor transmissions, a scaling of the mean
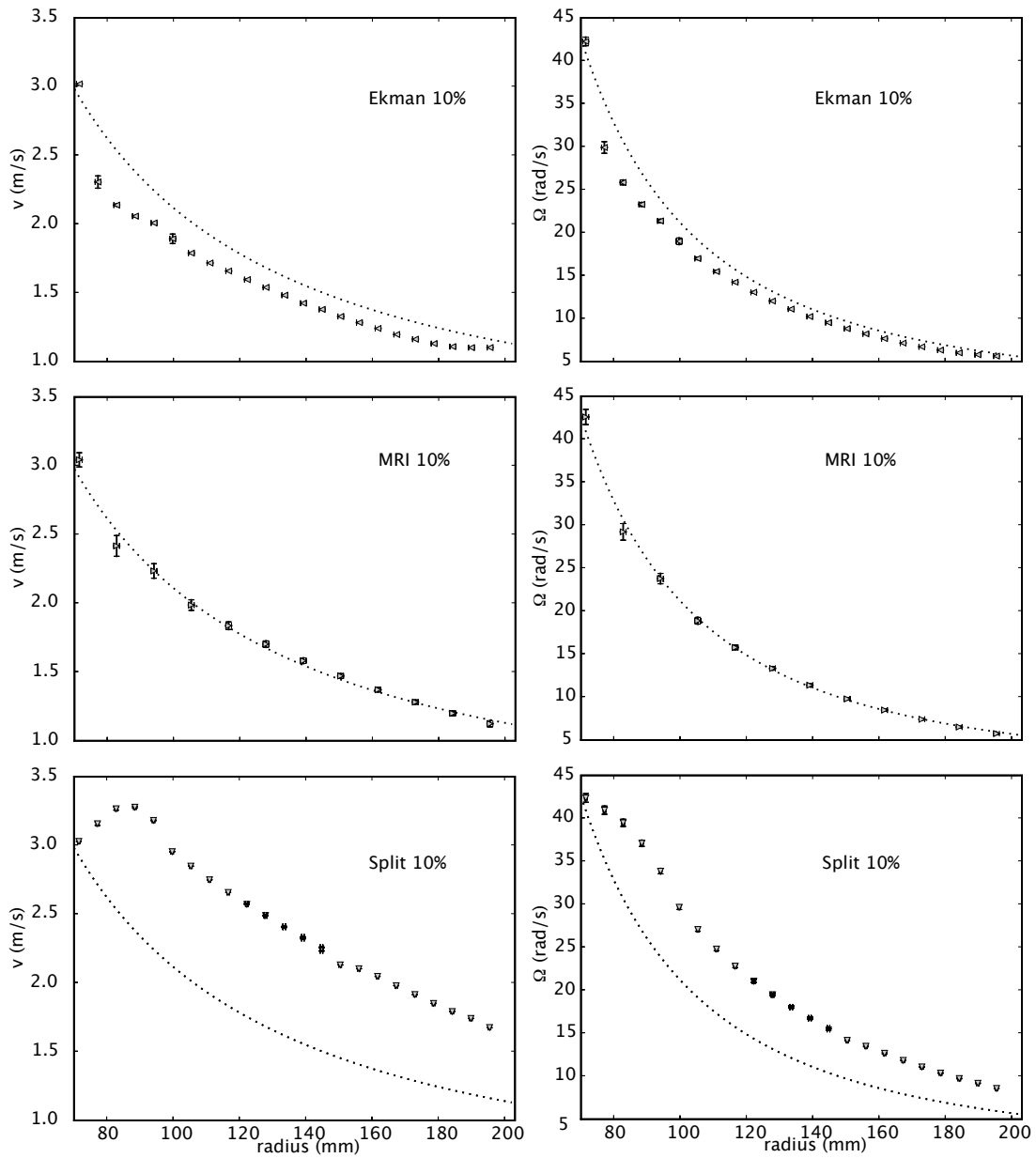
Figure 4.2: Velocity profiles at 10%, measured at $z = 76$ mm. Error bars are uncertainty based on the calibration. Dotted lines are the ideal circular-Couette profile.
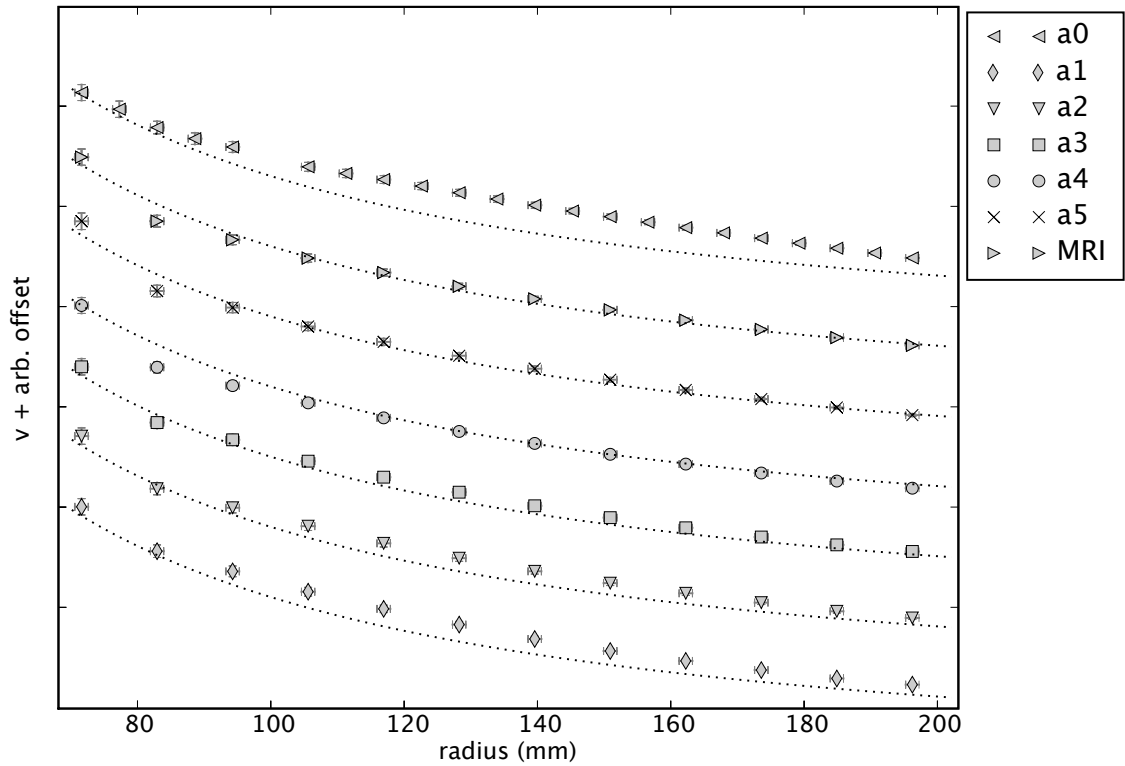
Figure 4.3: Fine control of velocity profiles at 5%, measured at $z = 76$ mm. The end rings speeds for each iteration are given as the ratio to the outer cylinder speed, Ω/Ω_2. The ideal circular-Couette profile is plotted as the dotted line.

profile with Reynolds number must be relied upon for our knowledge of the fluid state for high-speed liquid metal experiments. A scan of the `MRI` configuration was performed over the range $Re \sim 1 \cdot 10^4$ to $1.3 \cdot 10^6$. Fig:4.4A plots the results of these scans. The profile remains a good approximation to the ideal circular-Couette profile throughout the range of Reynolds number. To within about 3%, doubling the component speeds results in a doubling of the mean azimuthal velocity.
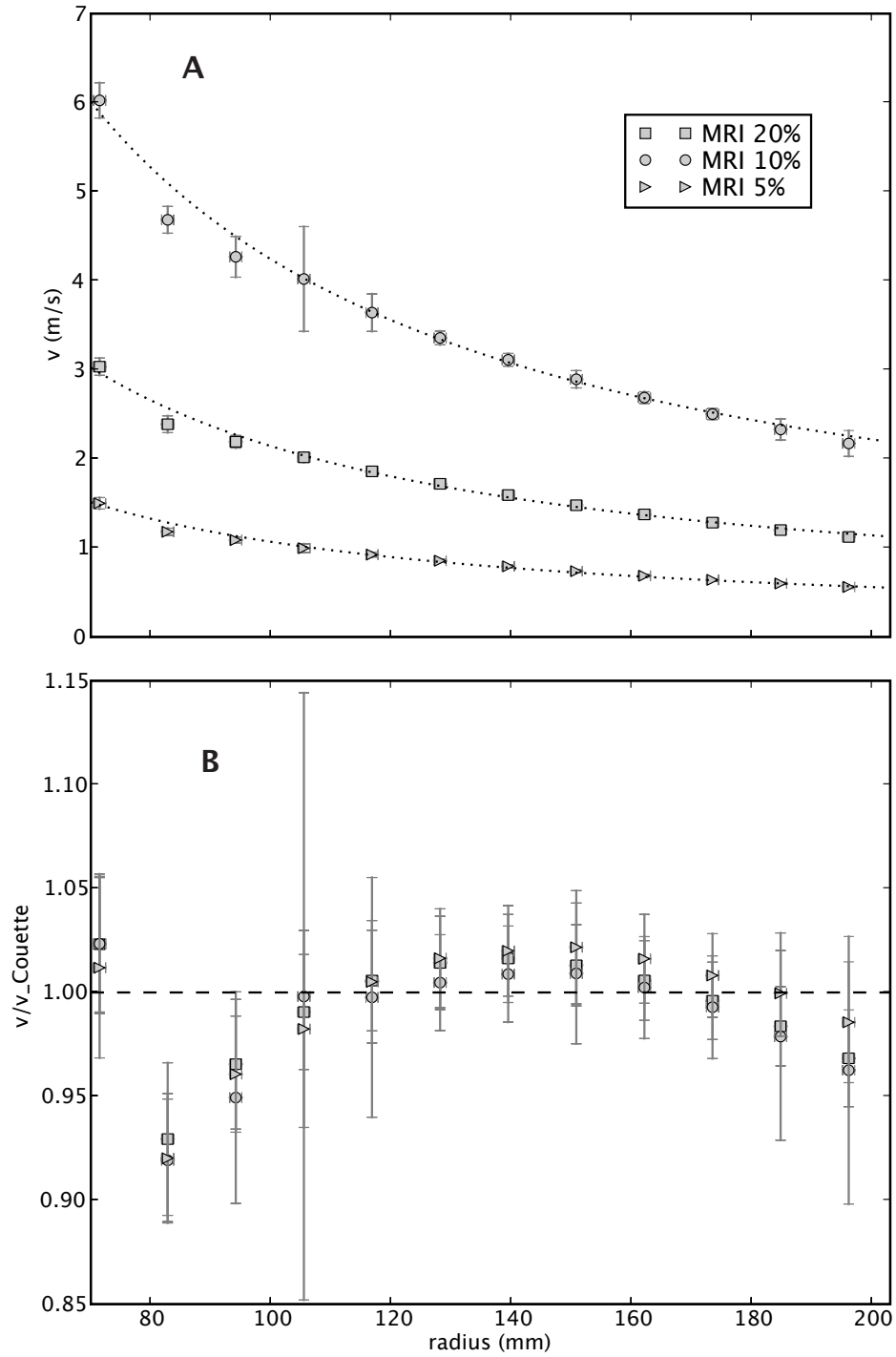
Figure 4.4: A) Reynolds number scaling of the `MRI` profile. B) Mean profile normalized to the ideal circular-Couette speed. The large fluctuation at $r \approx$ 107 mm in the 20% profile is due to outliers produced by optical defects.

4.2.3   Comparison to simulation

A primary goal of the PRINCETON MRI EXPERIMENT is to provide a laboratory benchmark for codes used to simulate accretion disks. In pursuit of this goal, three codes have been adapted or developed to simulate the experiment. The first code is an incompressible, 2D, axisymmetric hydrodynamic solver. It was written as part of the prototype experimental campaign. Details of the code and experimental results can be found in [Kageyama et al., 2004]. The other two codes include MHD effects, and were used to perform simulations of both hydrodynamic and MHD experiments with the new PRINCETON MRI EXPERIMENT apparatus. Wei Liu[Liu, 2007] adapted the 2D, axisymmetric, compressible MHD code ZEUS-2D for use with the insulating and partially-conducting boundary conditions of the experiment. The third code is a 3D spectral element solver developed by Fischer, Obabko and Cattaneo[Obabko et al., 2006] Argonne National Laboratory and the University of Chicago. Kageyama's simulation of the prototype was extremely successful in reproducing qualitative features of the experimental mean profile of azimuthal velocity. The data of Figure 9 in [Kageyama et al., 2004] is reproduced in Figure: 4.5. The overlap of the simulated and experimental data indicates that the simulation captures the most important physics despite being reduced in Reynolds number by a factor of more than 300 from that of the experiment and 2D.

Also plotted are simulated and experimental profiles of the new apparatus operating in the `Ekman` configuration. The ZEUS 2-D code was used at $Re \sim 10^4$ and the experiment performed at 10^5. The expectation was that the reduced difference in Re would produce agreement at least as good as that achieved for the prototype. Instead, there is no longer any region over which the simulated and experimental profiles overlap. Comparison with the 3-D simulations as well
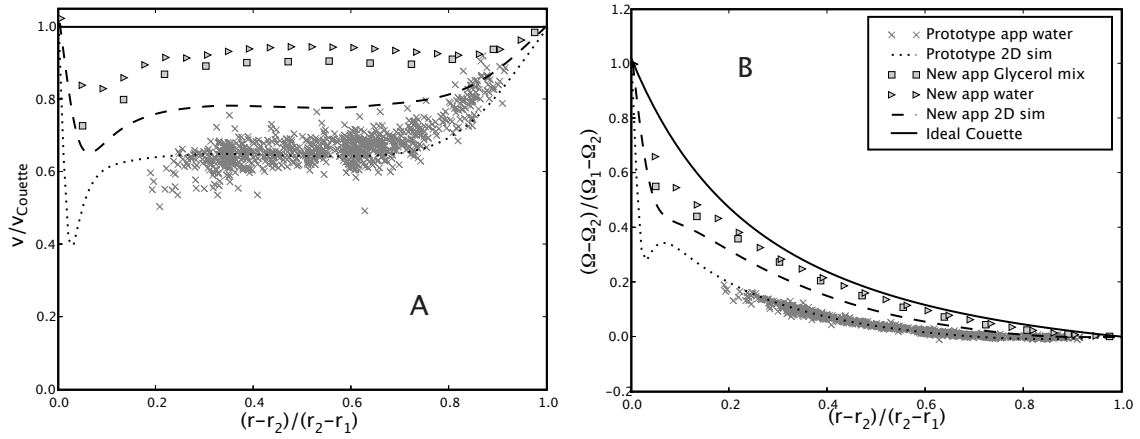
Figure 4.5: Comparison of agreement between simulated and experimental profiles for both the prototype and current apparatus. The excellent qualitative agreement achieved for the prototype has been lost with the new apparatus. Prototype velocity data is indicated by the crosses, which were measured via Particle Tracking Velocimetry at $Re \sim 10^6$. Simulation of the prototype used the 2D code by Kageyama[Kageyama et al., 2004] and was performed at $Re = 3200$. Simulation of the new apparatus used the ZEUS 2-D code[Liu, 2007] at $Re \sim 10^4$. The Reynolds number of the experiment with the new apparatus is $\sim 10^5$. In panel A, the profiles have been normalized to their respective ideal circular-Couette profiles based on the speeds of the cylinders. Angular velocity is plotted in panel B, normalized by the rotation rates of the cylinders. The experiments and simulations are located near the quarter height of each apparatus.

as ZEUS 2-D are shown in Figure: 4.6. The 3-D simulation agrees with the 2-D results indicating that the discrepancy generated by the new apparatus is not simply "3-D effects" acting within the bulk of the flow. At the time of the simulation, the model of the apparatus reflected our best knowledge of the mechanics of the experiment.

To rule out the possibility that the discrepancy was due to effects not captured by the lower Reynolds number of the simulations we replaced the water with a Glycerol-water mixture. The Glycerol to water ratio was tailored to reduce the experimental Re by a factor of 15.0 to coincide with that of the simulations (for details of the mixture, see Sec:3.2). Though improved, the agreement was still not comparable to that achieved for the prototype. The solution was hinted at when the Chicago group [*private communication*] added to the inner cylinder boundary condition a velocity white-noise with $\Delta v/v = 1\%$ in order to approximate possible effects due to the inner cylinder runout. Though the 3-D simulation was designed to include few approximations of the physical apparatus to gain as much insight as possible in to the physics of the flow, the white-noise prescription was very successful in restoring agreement with the experiment.This indicated that a disruption of the boundary flow was responsible for the performance of the apparatus.

Knowing that the simulations could match the experiment by destroying the coherence of the boundary layer flow, we needed to next identify where the disruption was taking place in the apparatus. The performance of the experiment in the `Ekman` configuration, where there was no attempt at optimization of the flow, indicated that the improvement in approximation of ideal circular-Couette flow was not due to a particular choice of end ring speeds. This pointed to differential rotation of the inner ring with respect to the inner cylinder as the source of disruption. To test this hypothesis, the ZEUS 2-D simulation was run for
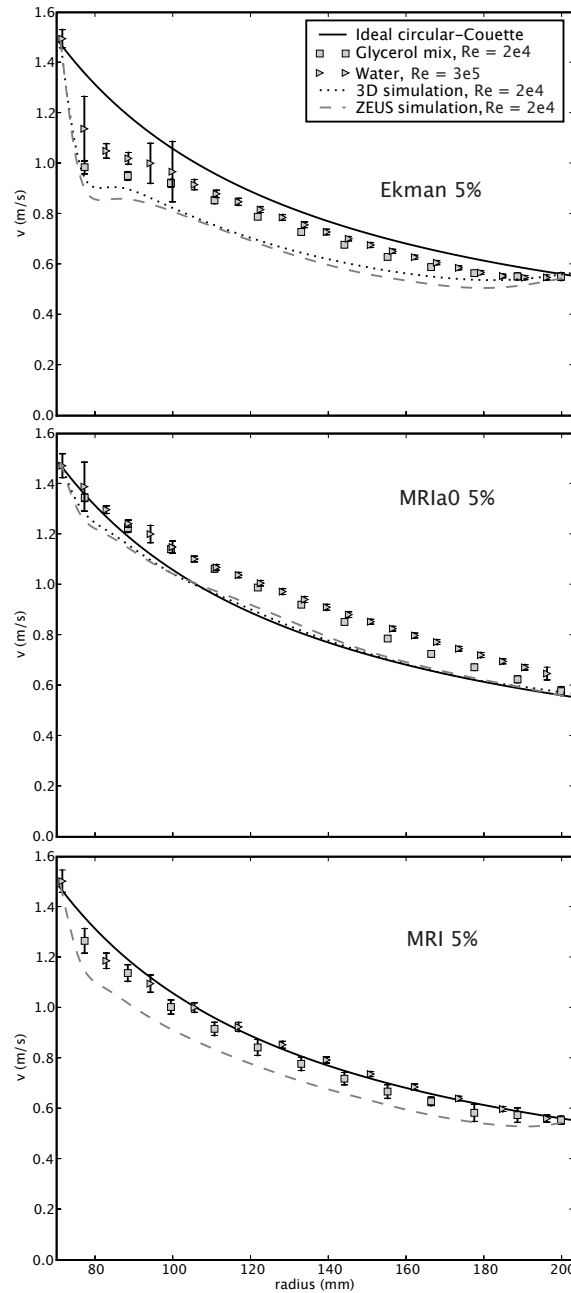
Figure 4.6: Comparison of 5% profiles to two simulations: axisymmetric 2-D[Liu et al., 2006b], and 3-D spectral element [Obabko et al., 2006]. Three configurations are compared: `Ekman`, `MRI` a0 and `MRI`. The optimization that led to the `MRI` profile was carried out after the 3-D simulations were completed, therefore only the ZEUS 2-D results are available to compare with the `MRI` case. Reynolds numbers for the simulations are $\sim 10^4$, which matches the Re of experiment operating with the Glycerol-water mixture. For water, $Re \sim 10^5$.

the `Split` case in order to compare it to the experimental `Split` profile. A comparison of the simulation and measurement is shown in Figure: 4.6. Excellent qualitative agreement has been restored, consistent with the interpretation that the boundary layer is primarily disrupted at the transition from the inner ring to the inner cylinder. The mechanism of disruption will be addressed in Section: 4.2.4.
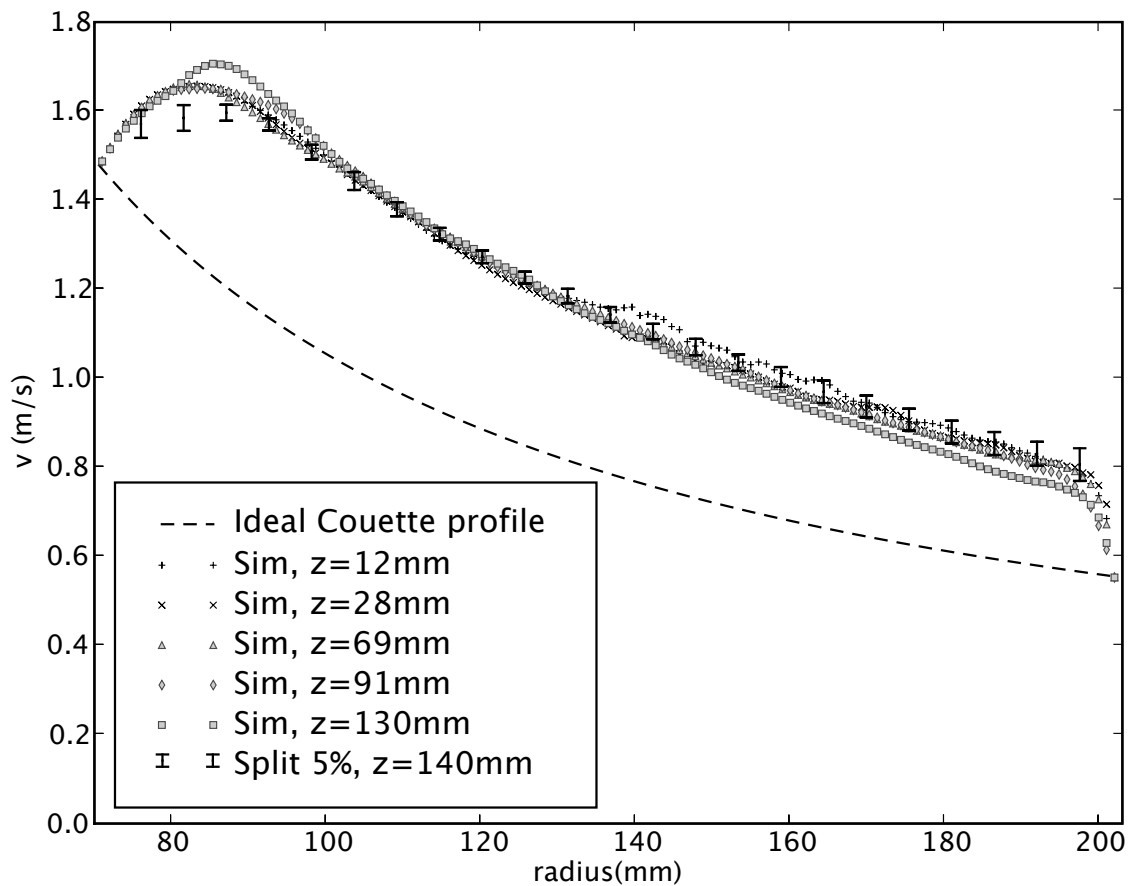
Figure 4.7: Operation in the `Split` configuration restores the agreement of the simulation with the experimental profile. The simulation used here is the 2D incompressible code of Kageyama. The Re of the simulation is $\sim 10^4$ and that of the experiment is $\sim 10^5$. Rigid rotation of the inner ring with the inner cylinder in the `Split` configuration does not disrupt the boundary layer.

4.2.4   Disruption of Ekman circulation

In the analysis of the prototype experiment [Kageyama et al., 2004], the boundary layer was seen to establish a large-scale poloidal circulation which efficiently transported angular momentum from the inner cylinder to the outer cylinder. Analysis of the simulations showed that at the end caps the layer was an axially-thin, radially-inward flow. This flow then turned at the interface of the inner cylinder to the end cap and became an axial flow which traveled to the middle of the inner cylinder. At the cylinder midplane the oppositely-directed axial flows from each end cap merged to form a radial jet. In this model, the circulation volume for the flow generated by one end cap is then half of the experimental volume.

From the experience with the prototype, if the PRINCETON MRI EXPERIMENT apparatus featured no runout of the inner cylinder we should observe a velocity profile in which at least two poloidal circulation cells are established within the bulk flow, with one cell driven by each end cap. The runout therefore must either reduce the size of the circulation regions, or prevent their formation.

The superior ideal circular-Couette approximation developed by our apparatus when operating in the `Ekman` as opposed to the `Split` configuration is opposite to that seen in other experiments, e.g. Richard's Figure: 4.2[Richard, 2001] comparing the two operation modes. In Section: 4.2.3 we demonstrated that differential rotation of the inner cylinder with respect to the inner ring is the source of the boundary layer disruption which underlies our experimental success. When these components differentially rotate, the inner cylinder has a large runout due to the oversize radial clearances of the submerged plain bearings. The bearings must be the source of the runout because the cylindricity of the inner cylinder surface and concentricity with respect to its axle are within

the limits of standard machine practice. However, the bearings guarantee concentricity of the inner cylinder to only about 0.25 mm. This is an order of magnitude larger than the concentricity tolerance of journal or ball bearings used in such experiments as those of Richard, Wendt and Lathrop [Richard, 2001],[Wendt, 1933],[Lathrop et al., 1992] where the tolerance can achieve 0.01 mm.

Under differential rotation of the inner cylinder with respect to the inner ring a discontinuity in angular velocity occurs along the curve $r \rightarrow r_1$, $z = 0$ where $z = 0$ is the surface of the lower inner ring which faces the bulk flow (an identical condition holds for the upper ring so no loss of generality occurs in discussing only the lower ring). For the anti-cyclonic profiles (other than Split , which does not feature differential rotation) explored here, the discontinuity is centrifugally unstable within some region close to the component intersection. Within that region a boundary layer roll develops, see Figure:4.8A. The radial and vertical extent of the roll is determined by pressure balance between the roll and the combined bulk flow and Ekman circulation.

For the PRINCETON MRI EXPERIMENT , the effect of the inner cylinder runout on the roll is diagrammed in panel B of Fig:4.8. The runout of the cylinder is a significant fraction of the groove width. As the high side of the cylinder passes it sweeps the roll out of the groove, similar to an eccentric displacement pump. The roll is ejected in to the flow near the ring as an eddy. The presence of these eddies is hinted at in the 5 mm scan of Fig:4.11.

The 5 mm scan of Fig:4.11 has been reproduced in Fig:4.9. The original data is replotted as solid triangles. The three points between 80 and 115 mm feature a double-peaked velocity distribution, which has been included in the inset histograms. The two peaks of each histogram have also been plotted with the mean profile marked by the diamonds. The lower velocity peak is that of the bulk
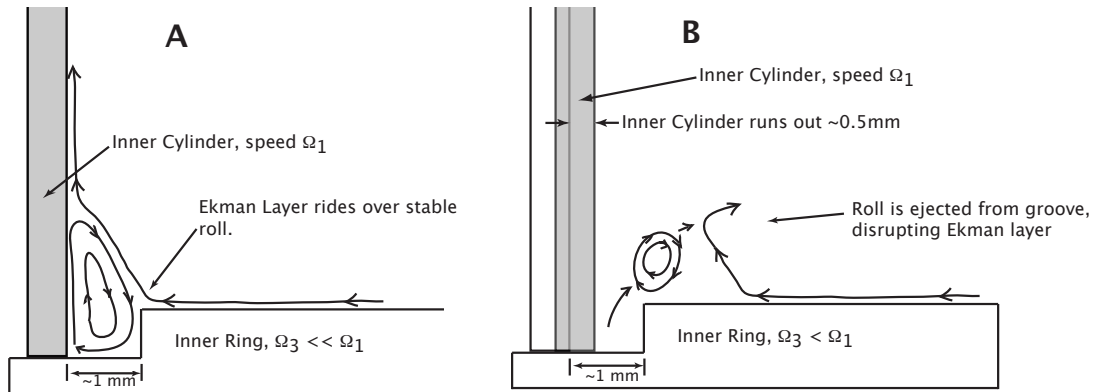
Figure 4.8: A) In experiments with insignificant runout of the inner cylinder, when the end cap differentially rotates the poloidally-circulating boundary layer separates from the inner ring then reattaches to the inner cylinder after passing over a recirculation region. B) In the PRINCETON MRI EXPERIMENT , the runout of the inner cylinder causes it to sweep a large fraction of the gap between it and the inner ring. This sweeping motion ejects the roll from the gap preventing the reattachment of the outer boundary layer.

MRI flow. The difference in arrival time for a velocity from each peak can be as small as 3 ms which indicates that a velocity discontinuity may occupy the measurement volume which is less than 2 mm in radial extent. This provides strong evidence that the upper peaks are eddies being shed by the cylinder-ring corner.Taking the difference in peak velocities as a measure of the eddy circulation speed and width of the groove as a characteristic size gives an eddy turn-over time of:

$$\tau_{eddy} \sim \frac{0.001m}{0.37m/s} = 0.003s,$$

which is comparable to the arrival times of the eddies in the data.
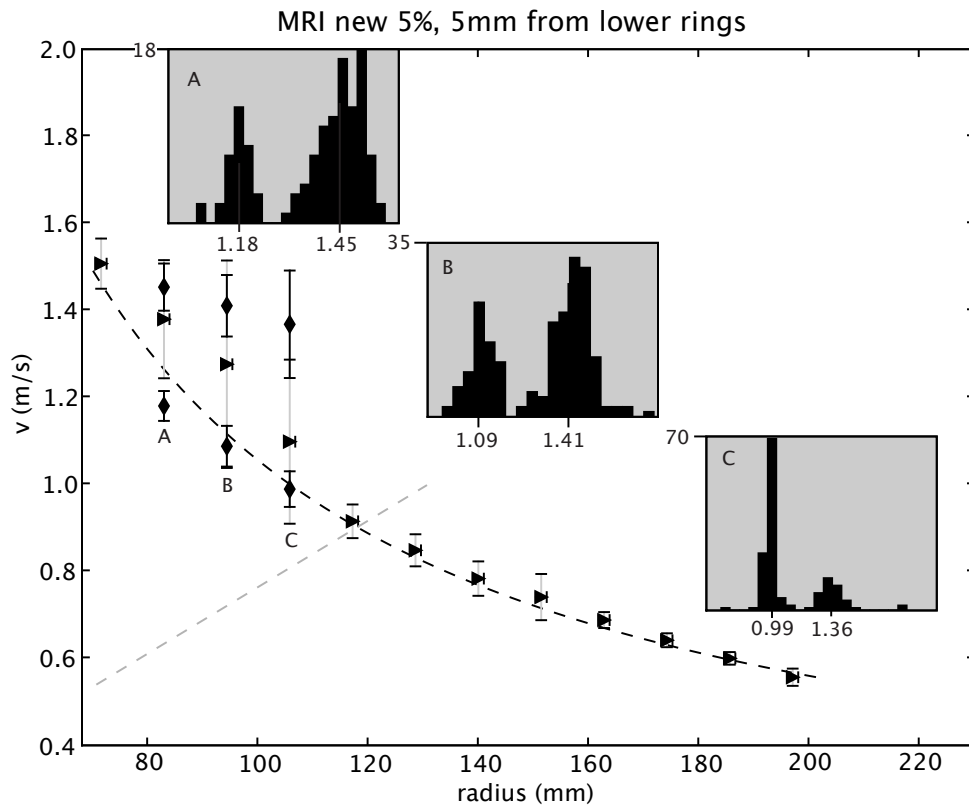
Figure 4.9: Radial scan of the MRI 5% profile at $z = 5$ mm. The dashed line is the ideal circular-Couette profile. Solid triangles are the mean speed measured by the LDV. The three points, A, B, C exhibit mean speeds above the Ideal circular-Couette line. Inset histograms of these points shows two peaks in the velocity distribution.

4.2.5 `Keplerian` profile

The `Keplerian` configuration was originally intended to produce a nominal $q = 1.5$ profile that has an angular velocity shear that is as relevant to accretion disks as our apparatus is capable. During the January 2006 LDV experiments, an optimization process similar to that for the `MRI` profile was performed to determine optimal end ring speeds.

A comparison of velocity, angular momentum and q for MRI and `Keplerian` 10% profiles are presented in Fig:4.10. The data were acquired during the third experimental run with the Dantec diagnostic in January 2006. In the October 2005 data, the largest radius at which the profile was measured was 195 mm, here it is 200 mm. The dip in q at 200 mm for the MRI profile is due to this closer proximity to the outer cylinder where the flow must transition to match the boundary.
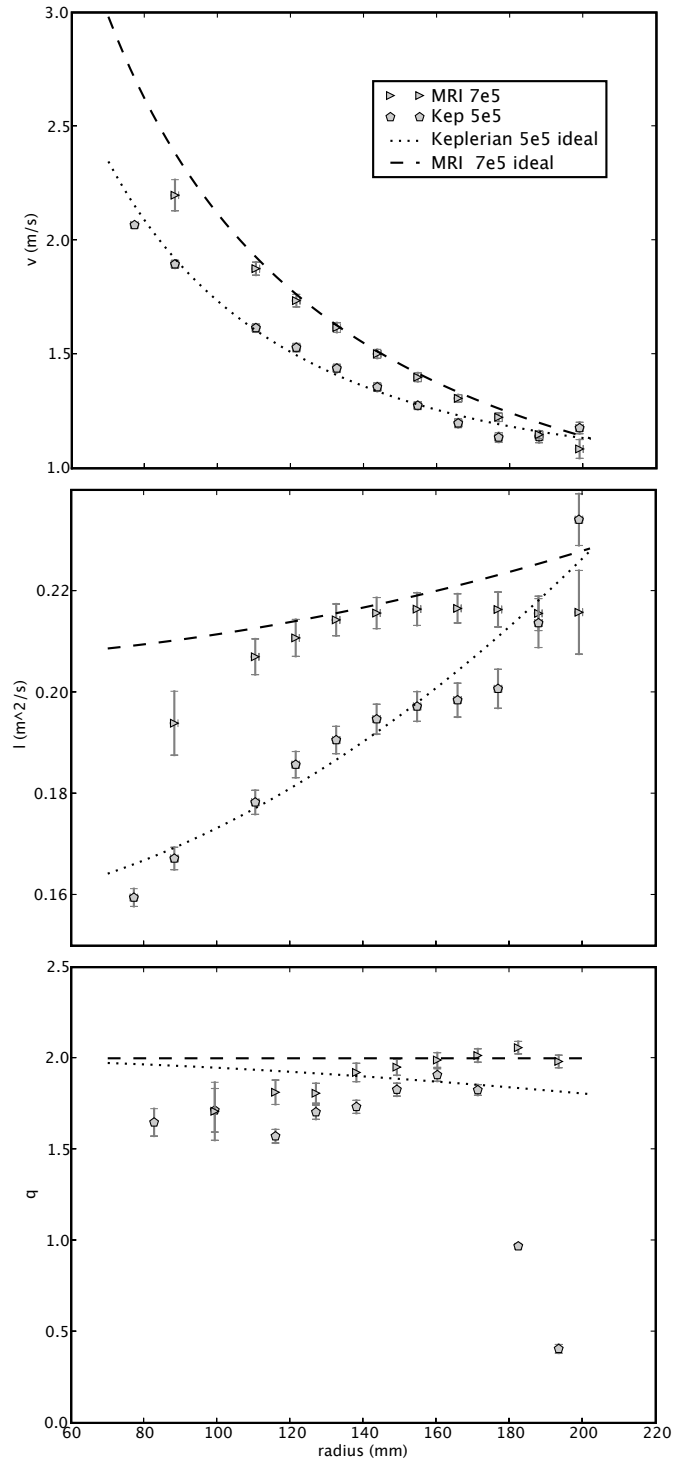
Figure 4.10: Comparison of velocity, specific angular momentum and q between MRI and `Keplerian` 10% profiles. In the q plot, the dashed line is the Rayleigh Criterion and the dotted line is q for the ideal circular-Couette profile corresponding to MRI 10% speeds.

4.3 Axial Variation of Profile

4.3.1 Axial variation of mean profile

During the initial water experiments, a vertical scan of the mean profile produced by the `MRI` a0 configuration was performed. The goal was to determine how deep into the bulk flow any variation produced by the end rings was propagated. The profiles are plotted in Figure: 4.11. In the left panel, to aid visual comparison the profiles have been vertically offset by an arbitrary amount. The profile deviation seen in the scan at $z = 5$ mm near the inner cylinder is due to the presence of eddies (see Section: 4.2.4) shed by the inner cylinder- inner ring gap. The mean profile within the bulk of the flow shows no significant axial deviation, though enhanced fluctuation levels can be seen in the $z = 5$ mm scan.In the right panel of Figure: 4.11 the effect of the eddies has been removed and the velocities normalized by the ideal circular-Couette profile.

The consistent depression of the profile from the ideal circular-Couette case for $r \leq 100$mm indicates that angular momentum is being vertically transported through the inner ring. Because the end ring speed is lower than the inner cylinder, a centrifugally unstable layer is likely to exist in this region.

4.3.2 Fluctuations across the full radial volume

Relative fluctuation levels at an axial height of 76 mm for the full radial gap are plotted in Figure: 4.12. The upper panel compares relative fluctuations in radial scans of `MRI` 5,% 10% and 20% with solidbody, `Ekman` 5% and `CUS` 5% cases. The centrifugally unstable case has component speed ratios of $[\Omega_1, \Omega_3, \Omega_4, \Omega_2]/\Omega_2 = [11.5, 3.5, 1.3, 1.0]$, corresponding to the `MRI` A0 5% configuration with a faster inner cylinder speed. Solidbody and `MRI` 10% scans
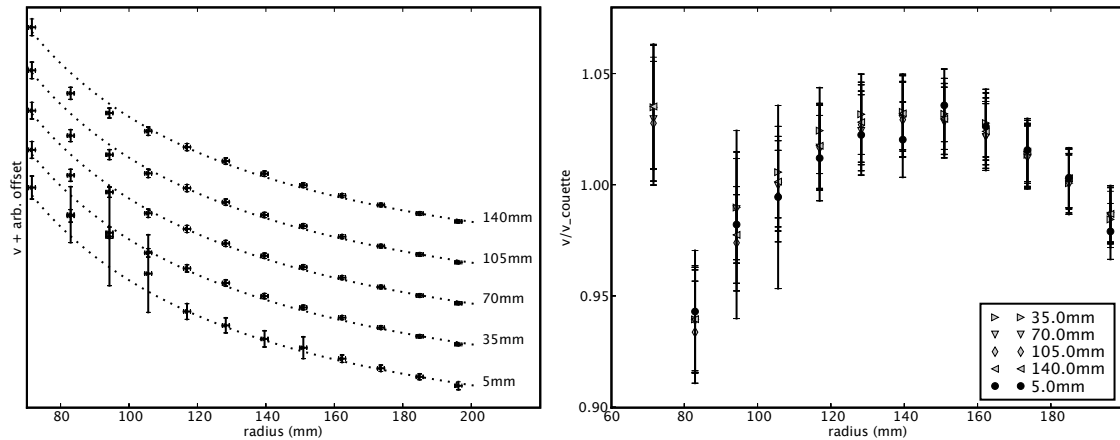
Figure 4.11: Left: Radial scans of azimuthal velocity for `MRI` 5% flow. Velocities have been offset by an arbitrary amount to ease visual comparison. Dotted lines are the ideal circular-Couette profile. Right: Azimuthal velocity normalized to ideal Couette speed. 5 mm scan has had eddies removed from data over the inner ring, see Section:4.2.4

from the January 2006 run (labeled r3) are also included. The scans were acquired at an axial height of $z = 74$ mm. The scatter in fluctuation amplitude between the inner cylinder and $r \simeq 115$ mm is due to low sample numbers. In the `MRI` 20% data, optical defects which produced extreme velocity measurements have been filtered out. "Extreme" is defined as being displaced from the mean by more than 3 standard deviations, where the standard deviation is computed on *all* samples in a measurement (relative to the standard deviation of the filtered data these points lie in excess of 5 standard deviations from the mean). This filtering affected only the points inside of 110 mm.

The departure from solidbody levels for the sheared-flow profiles at radii between the inner cylinder surface and 100 mm is due to optical defects. This effect is confirmed by comparison with the centrifugally unstable data.

The fluctuation levels near 118 mm are consistent with the inference based on
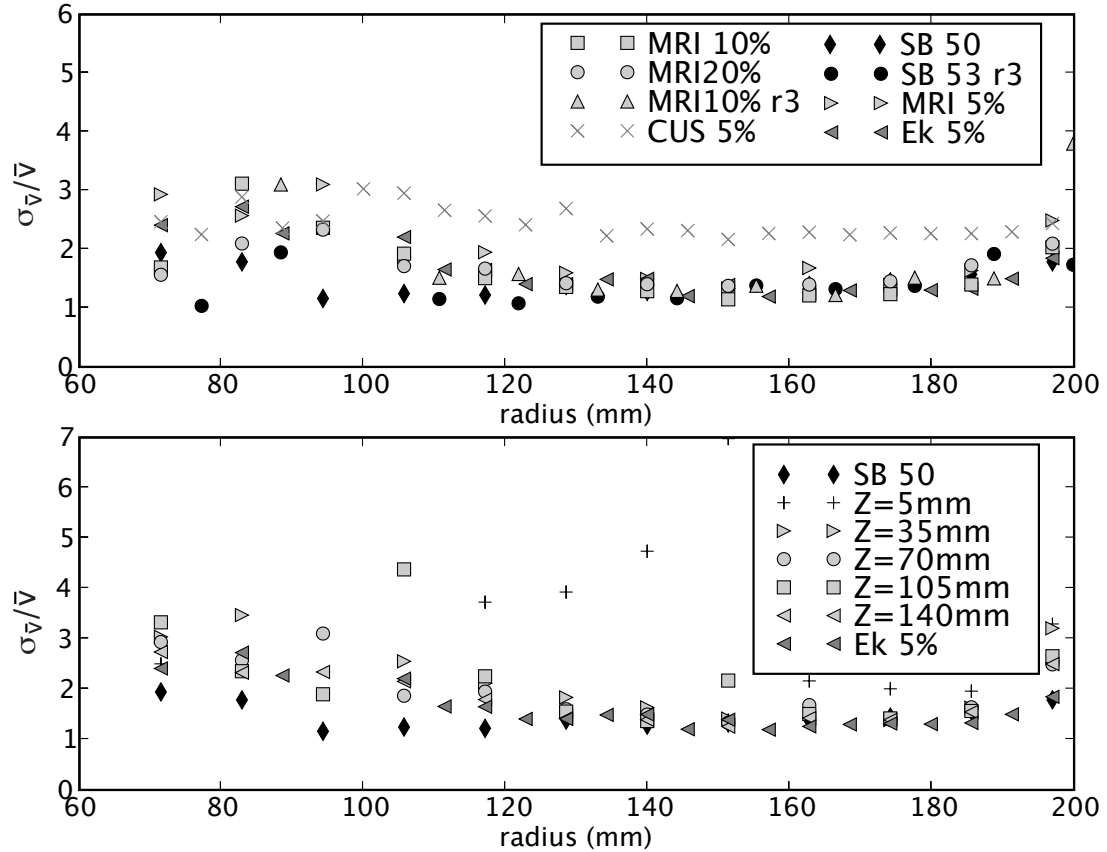
Figure 4.12: Top: Relative fluctuations for `MRI` profiles at 5, 10, and 20%. The data were acquired at $z = 74$ mm. Two scans from experimental run 3 (January 2006) are labeled with the suffix "r3". The large scatter in fluctuation level between the inner cylinder and $r \simeq 100$ mm is due to both low sample number and optical defects. In run 3, January 2006, optical defects make the data acquired at 100 mm unusable $(\sigma_{\bar{v}_\phi} \sim \bar{v}_\phi)$. Data from `Ekman` 5% and `CUS` 5% cases are included for additional reference. In the `MRI` 5% data, the large fluctuations for the radius overlapping the inner cylinder are caused by an oscillation of the boundary speed. During this experiment Ω_1 varied by about 2% on a 5-second timescale. Bottom: Radial scan of relative fluctuations in `MRI` 5% profile at several axial locations. The three points between 80 and 115 mm of the $z = 5$ mm scan exceed 7% due to the presence of eddies. See Sec.4.2.4 for a discussion of the eddies.

Figure: 4.13 that a boundary layer extends in to the bulk flow near 118 mm. The elevated levels on the inner cylinder surface for the 5% cases are due to poor speed control of the inner cylinder during the October 2005 experiments. In particular, during the `MRI` 5% scan, Ω_1 oscillated by about 2% over a 5-second period. By Rayleigh's centrifugal stability criterion this oscillation was too small in magnitude to produce instability. The ability of the oscillation to elevate fluctuation levels in the bulk flow would therefore be governed by the Ekman time, $\tau_{Ekman} \simeq 10s$. Because it was slower than τ_{Ekman} it is not responsible for the elevated fluctuations seen for $115mm < r < 130$ mm.

The fluctuation magnitude of one other radius must be pointed out. For the January 2006 data, the scan grid included a point at $r = 200$ mm. In the figure the fluctuation levels at that radius for an `MRI` 10% profile are the highest for the figure, both in absolute value and relative to the solidbody profile. This may be explained by the presence of a Rayleigh-stable boundary layer in the measurement volume. Such a boundary layer must exist to transition the bulk mean flow speed to the solidbody speed of the outer cylinder.

4.3.3   Fluctuations near the ring gap

During the October 2005 experiments, a detailed vertical scan of an `MRI` 5% profile was made at four radii near the ring gap. The goal was to determine if a Stewartson Layer[Stewartson, 1957] was being formed by the discontinuity in speed at the ring gap and propagating vertically in to the experimental volume. This effect was predicted to occur in our experiment by Hollerbach and Fournier [Hollerbach and Fournier, 2004].

Stewartson layers are expected to form in regions where the Taylor-Proudman theorem holds. For our geometry where all rotation is about the z-axis, the

Taylor-Proudman theorem is simplified to:

$$\frac{\partial \mathbf{v}}{\partial z} = 0.$$

If Stewartson layers were formed in the experiment the effect would be to extend the solidbody velocity of the end rings vertically through the bulk flow. Because we always operate with the inner ring rotating faster than the outer ring, this layer should give rise to a drop in azimuthal velocity as the LDV measurement scans outward across the gap. Hollerbach and Fournier further predict that this shear layer will be unstable to a Kelvin-Helmholtz instability and that this instability will not "break" the Taylor-Proudman theorem. If these predictions hold in our experiment, we will observe enhanced fluctuation levels in some annulus above the ring gap.

The results of our search for a Stewartson layer are plotted in Figure: 4.13. Relative fluctuations for a solidbody profile are indicated by the vertical dotted lines. Large effects due to the gap vertically propagate only about 40 mm after which the fluctuations are roughly uniform. For the radii $r = 129, 134, 140$ mm, the uniform level is close to that for solidbody. Detailed solidbody scans were not performed, which limits our ability to further remark on residual discrepancies between the profiles at these radii. This is illustrated by examination of the measurement $r = 129$ mm, $z = 76$ mm. The velocity samples at this point were filtered to remove a single measurement (out of more than 200 samples) which was severely distorted by an optical defect in the outer cylinder. The removed point lay more than ten standard deviations off the mean of the remaining data. To illustrate the effect of that outlier, the fluctuation level including it is plotted marked by the cross. Distortion by a single optical defect has increased $\sigma_v/\bar{v}$ from 1.4% to about 4%.

At $r = 123$ mm the uniform fluctuation level above 40mm is clearly
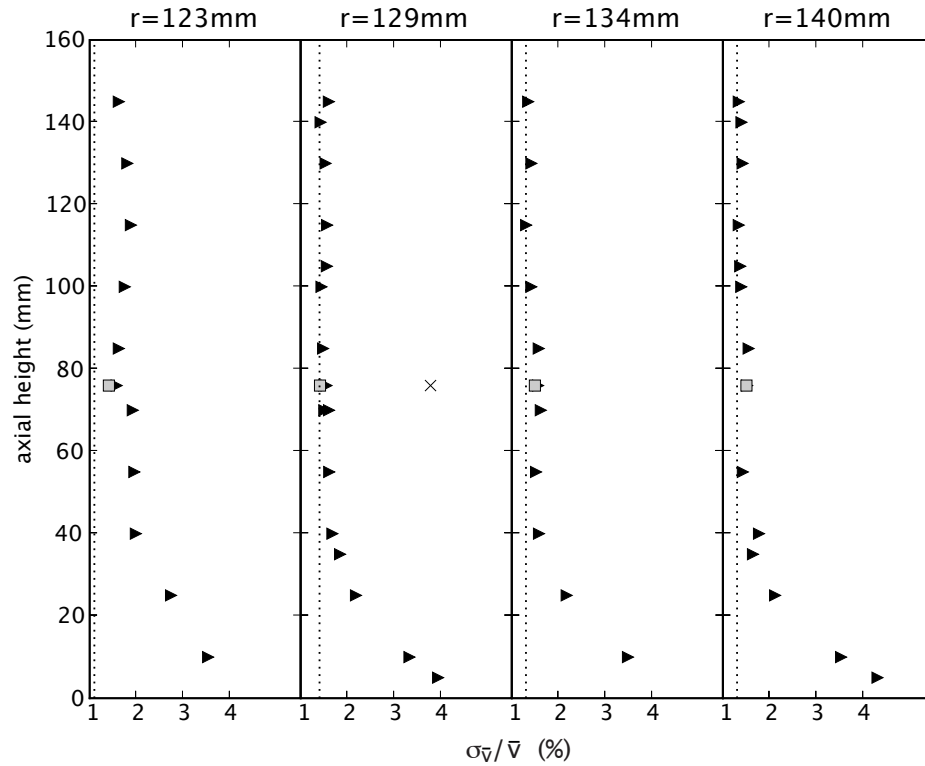
Figure 4.13: Axial scan of `MRI` 5% profile for four radii near the ring gap. The listed radii are nominal values, the precise location of a measurement may be at most 3 mm different. The ring gap is at 132 mm. The vertical axis is the height at which the scan was performed, measured from the top side of the lower end ring. The horizontal axis is the percentage relative fluctuation $\sigma_{v_\phi}/\bar{v}_\phi$. Vertical dotted lines indicate fluctuation levels for solidbody for a radial scan performed at $z = 74$ mm. Detailed vertical scans for solidbody were not made. Gray squares are data from an `Ekman` 5% profile. The `MRI` 5% data were filtered to remove velocity measurements which lay more than 6 standard deviations from the mean. An example of an unfiltered measurement has been marked by the $\times$ in the $r = 129$ mm data. At that point, a single measurement (out of ≈ 200) raised the fluctuation level to 4%.

distinguishable from solidbody. Part of this is due to a reduced level for solidbody, and part to an increased level for the MRI 5% case. To quantify the increase, we compare it to $r = 140$ mm. To make the comparison we note that optical defects do not act to *reduce* measurement noise. Therefore the low and constant level of the fluctuations at 140 mm are not contaminated by any vertical non-uniformity of defects. For the MRI 5% profile the uniform fluctuation level is $1.79 \pm 0.05\%$ at $r = 123$ mm and at $r = 140$ mm it is $1.41 \pm 0.02\%$. The difference between the two is $0.38 \pm 0.05\%$. Two possible explanations for this increase are:

1. it is due to broadening of the measurement by an increase in the velocity gradient between 140 and 123 mm.

2. For MRI profiles, the inner ring velocity matches that of the ideal circular-Couette profile at $r = 118$ mm. The fluctuations may therefore be due to the presence of a boundary layer extending vertically into the bulk.

Addressing the first of these possibilities, can a changing radial gradient of velocity account for the increase in fluctuations? Ignoring the effect of optical defects due to the cylinder walls, broadening of the sample distribution for an LDV measurement arises through:

$$\Delta v = \nabla v \cdot c_0, \tag{4.1}$$

where the gradient is in the direction parallel to the length of the measurement volume, c_0. No measurement of c_0 exists within the bulk flow so we use the value of 1.7 mm measured on the inner cylinder surface as an approximation (the measurement of c_0 is detailed in Appendix:A). c_0 is parallel to $\hat{r}$ and using the ideal circular-Couette flow $\nabla_r v = a + br^{-2}$, we expect for $r = 123$ mm, $\Delta v / \bar{v} \approx 1.3\%$. At 140 mm, $\Delta v_\phi / \bar{v}_\phi \approx 1.1\%$. For a solidbody profile this estimate yields 1.4% and 1.2%, respectively. These levels are of the same order as the

observed fluctuations, but do not include the effect of optical defects which must increase them. It is therefore a poor approximation to use the measurement volume on the inner cylinder surface to estimate its value in the fluid interior as this overestimates velocity gradient broadening.

Turning from the use of Equation: 4.1, a more reliable comparison can be made using the `Ekman` profile. Here, the velocity gradient differs from that for `MRI` by only about 8%(see Figure: 4.2) while the end ring matches the bulk flow speed only at the outer cylinder, and there is therefore no possibility of the proposed boundary layer being present in the interior. Fluctuations for a radial scan of an `Ekman` configuration taken at $z = 76$ mm have been plotted with the `MRI` fluctuations in Figure: 4.13. The `Ekman` profile fluctuations are 1.41% at 123 mm and 1.50% at 140 mm. This near constant fluctuation level indicates that any effect due to the velocity gradient is insufficient to account for the `MRI` data at 123 mm. Ruling out the velocity gradient as the source of the increased fluctuation levels at $r = 123$ mm for the `MRI` case leaves the second possibility as the cause. The larger fluctuations at $r = 123$ mm in the `MRI` profile are therefore due to the boundary layer at $r = 118$ mm extending deep in to the bulk flow.

4.4 Reynolds stress measurement

4.4.1 Subcritical Hydrodynamic Instability

This section is adapted from and modifies the results published in [Ji et al., 2006]. Based on observations of Wendt and Taylor, Richard and Zahn[Richard and Zahn, 1999] argue that anticyclonic shear flow undergoes a subcritical turbulent transition when a Reynolds number based on the gradient of angular velocity exceeds a critical value:

$$Re* = \frac{\tilde{r}^3}{\nu} \frac{\Delta\Omega}{\Delta r} \left(\frac{r}{\Delta r}\right)^2 \approx 6 \times 10^5,$$ (4.2)

where $\tilde{r} = (r_1 + r_2)/2$ is the mid-radius of the cylinders and $\Delta r = r_2 - r_1$. For our apparatus $\tilde{r}/\Delta r = 1$ therefore our critical Reynolds number is expected to be $\approx 6 \times 10^5$. In addition to exceeding this Reynolds number, perturbations present in the experiment must be large enough to trigger the transition. Richard and Zahn argue that the turbulence observed by Wendt and Taylor was triggered by this subcritical transition. As discussed in Section:4.2.4, our apparatus is far more perturbative to the fluid than those experiments, and should therefore easily satisfy the finite-amplitude requirement.

The relation proposed by Richard and Zahn for the flux of angular momentum is:

$$\rho r \langle v_r' v_\phi' \rangle = -\rho \nu_t r^2 \frac{\partial \Omega}{\partial r},$$ (4.3)

where $\langle v_r' v_\phi' \rangle$ is the mean fluctuating component of the Reynolds stress, and the turbulent viscosity ν_t, is given by:

$$\nu_t = \beta \left| r^3 \frac{\partial \Omega}{\partial r} \right|.$$ (4.4)

In terms of q, this relation becomes $\beta = -\langle v_r' v_\phi' \rangle / q^2 v_\phi^2$.

4.4.2 Radial profile of local angular velocity exponent and angular momentum

Gradients of angular momentum and angular velocity may become sources of free energy to drive turbulent angular momentum transport in circular-Couette flow. Rayleigh's centrifugal instability and the ideal-MHD limit of the MRI are threshold instabilities in which the flow becomes linearly unstable when a critical gradient is achieved. The threshold for instability of both the ideal MHD version of MRI and centrifugal instability can be parameterized by the local exponent of angular momentum, $q \equiv -\partial \ln \Omega / \partial \ln r$. In MRI, the threshold (with a weak magnetic field) is simply $q > 0$. Marginal centrifugal instability occurs for constant angular momentum, $\Omega_1 r_1^2 = \Omega_2 r_2^2$, therefore the instability criterion becomes $q > 2$.

The value of q also arises in the subcritical hydrodynamic transition proposed by Richard and Zahn [Richard and Zahn, 1999], where β is related to the flow profile by:

$$\beta \equiv \frac{\langle v'_r v'_\phi \rangle}{q^2 \bar{v}_\phi^2}. \tag{4.5}$$

To measure β we need to determine q for the experimental profiles. For ideal circular-Couette flow,

$$q = -\frac{r}{\Omega} \frac{\partial}{\partial r} \left(a + b r^{-2} \right) = \frac{2}{\frac{a}{b} r^2 + 1}.$$

The PRINCETON MRI EXPERIMENT does not produce ideal circular-Couette flow, and for some configurations an estimate based on the cylinder speeds can be extremely misleading. Therefore we need to provide a measurement of q based on the measured angular velocity profile.

To calculate q from the measured velocity profiles a central difference method is used. To avoid errors associated with converting to angular velocity, the derivative is performed on v:

$$q = -\frac{r^2}{v}\frac{\partial v r^{-1}}{\partial r} = 1 - \frac{r}{v}\frac{\partial v}{\partial r}$$

This is implemented as:

$$\bar{r} = \frac{r_{i+1} + r_i}{2}, \quad \bar{v} = \frac{v_{i+1} + v_i}{2},$$

$$\Delta r = r_{i+1} - r_i, \quad \Delta v = v_{i+1} - v_i,$$

$$q(\bar{r}) = 1 - \frac{\bar{r}}{\bar{v}}\frac{v_{i+1} - v_i}{r_{i+1} - r_i}. \tag{4.6}$$

With the error in q given by:

$$\sigma_{\bar{r}}^2 = \sigma_{\Delta r}^2 = \sigma_{r_{i+1}}^2 + \sigma_{r_i}^2$$

$$\sigma_{\bar{v}}^2 = \sigma_{\Delta v}^2 = \sigma_{v_{i+1}}^2 + \sigma_{v_i}^2$$

$$\sigma_q^2 = \sigma_{\bar{r}}^2 (\frac{\Delta v}{\Delta r \bar{r}})^2 [1 + (\bar{r}\Delta r)^2] + \sigma_{\bar{v}}^2 (\frac{\bar{r}}{\Delta r \bar{v}})^2 [1 + (\bar{v}\Delta v)^2] \tag{4.7}$$

Profiles of q and l for `Ekman`, `MRI` and `Split` configurations are plotted in Fig:4.14. For `Split` operation, the flattening of angular momentum profile over the outer ring, with a steep negative gradient connecting to the outer cylinder wall indicates that regions of turbulent transport are present in the apparatus. The profiles of Lewis and Swinney (see Section: 2.1.2) showed that circular-Couette flow which is fully saturated by centrifugal instability exhibits two shear layers at the cylinder walls with negative angular momentum gradients while the interior has a flat angular momentum profile.For `MRI` operation, l appears to flatten over the outer ring. However, in this region a direct measurement of the $\hat{\phi}$-$\hat{r}$ component of the Reynolds stress tensor shows no sign of an enhanced radial transport. Therefore, angular momentum must be removed through the outer ring. The negative gradient of angular momentum in a laminar state seen here contradicts the Rayleigh stability criterion. Scaling of the

`MRI` profile with Re confirms that this is a characteristic of the `MRI` configuration, see Figure: 4.15A. Variation of q with alternate `MRI` configurations is plotted in Figure: 4.16. It is a consistent feature of all the variations that $q \geq 2$ for some radii above the outer ring.

According to the Rayleigh criterion linear instability occurs whenever the radial gradient of angular momentum becomes negative. The Rayleigh criterion was derived for the case in which angular momentum transport is purely radial in a rotating inviscid fluid. Taylor [Taylor, 1923] proved that for a narrow gap circular-Couette geometry with rigid cylinder walls, viscosity stabilizes finite, but small, negative gradients of angular momentum. When the outer cylinder is at rest the transition occurs for $Re \sim 10 - 100$, where Re is read as a measure of the inner cylinder speed. The results shown above indicate that vertical transport of angular momentum can give rise to a violation of the Rayleigh criterion where the resulting negative radial gradient of angular momentum is stable.The analysis of Taylor cannot be directly extended to our wide-gap geometry, so a proof of this stability is an area for future research.

The values of q used in the angular momentum transport measurement of Section: 4.4.1 are listed in Table: 4.5.
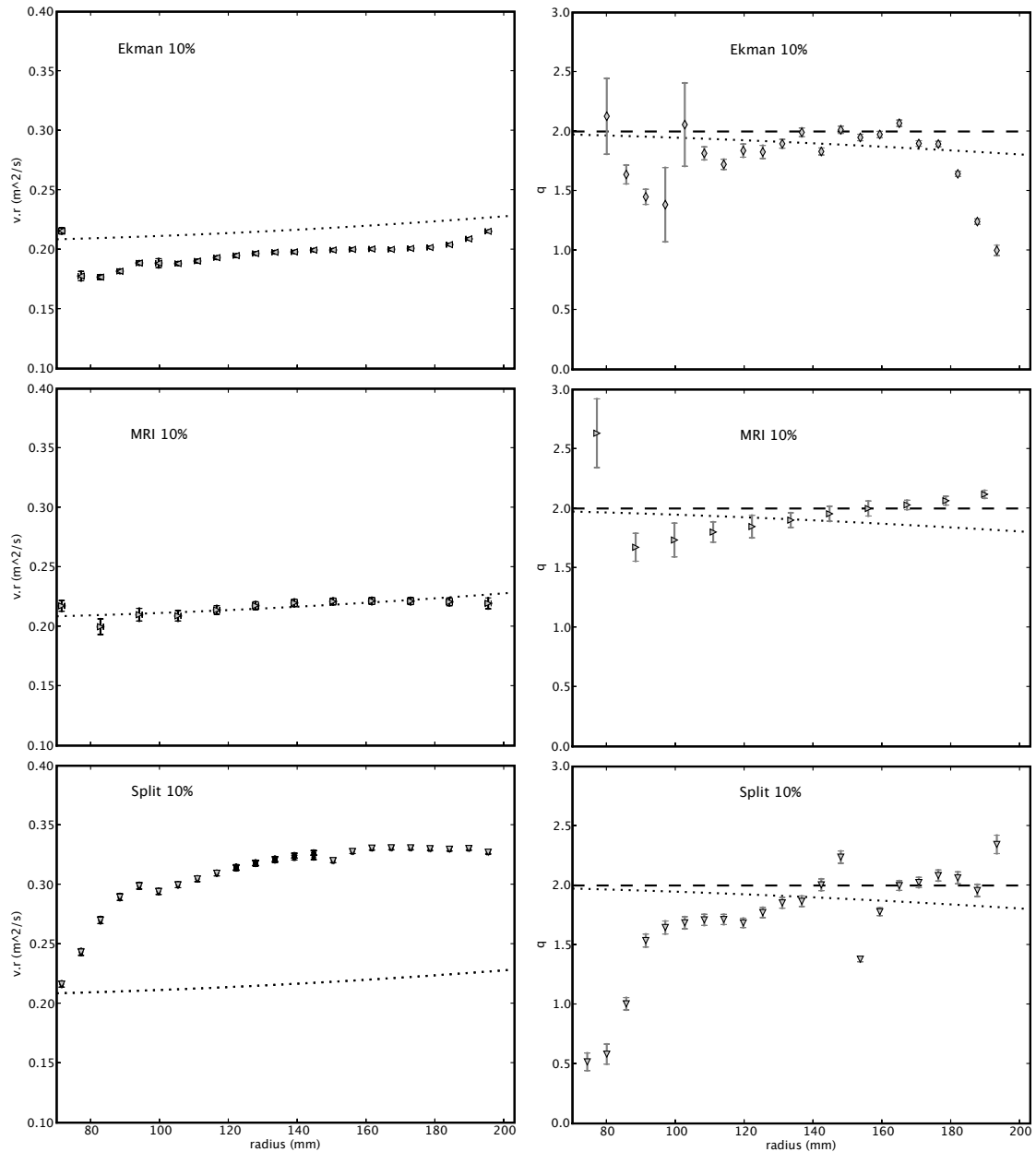
Figure 4.14: Comparison of l and q profiles for 10% `Ekman`, `MRI` and `Split` configurations. Angular momentum and q profiles for the ideal circular-Couette solution are indicated by the dotted lines. In the q plots, the Rayleigh stability criterion, $q = 2$, is indicated by the dashed line. In the `Split` data, several points near the ring gap have been substituted with data from a Stewartson layer study. Several points in the original profile featured large errors in the mean azimuthal velocity which were not observed in any other `Split` profiles. One data point from the original profile remains, and is the source of the large discontinuity in q near $r = 140$ mm.
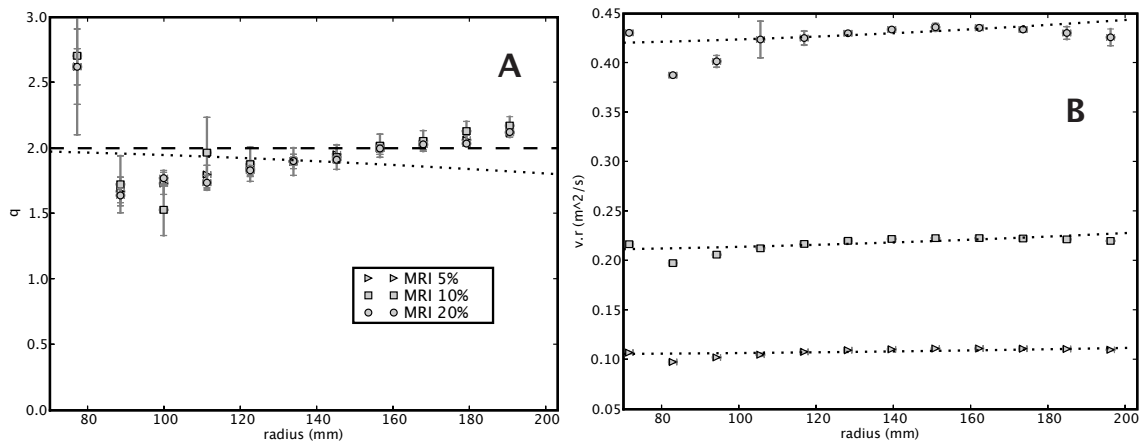
Figure 4.15: A. Scaling of q profile with Re for `MRI` profiles. Dashed line is the Rayleigh criterion, dotted is q for ideal circular-Couette flow. B. Scaling of l with Re . Dotted lines are ideal circular-Couette flows.
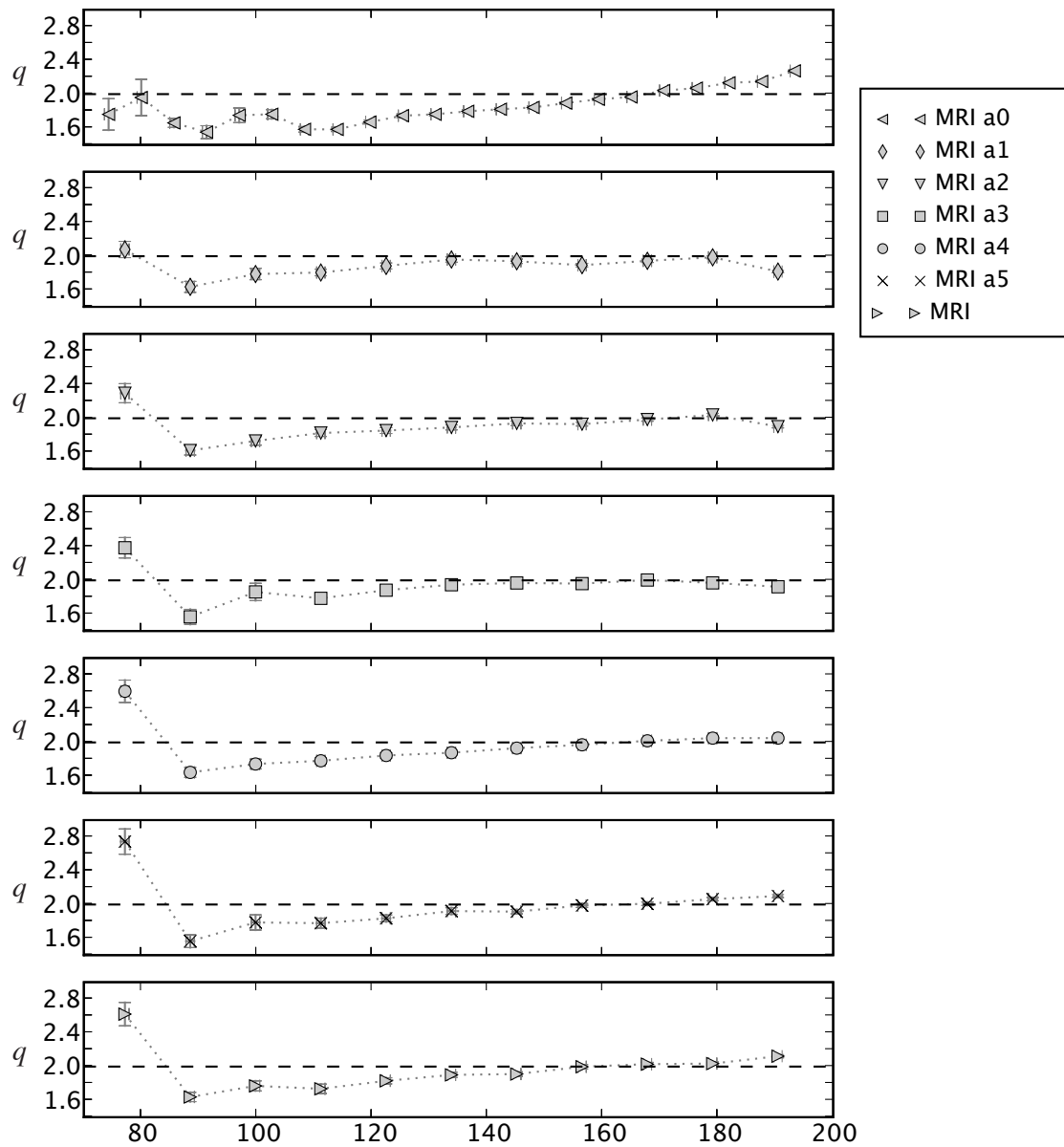
Figure 4.16: Variation of q with End Ring speeds for MRI 5% configurations. To ease visual comparison, the q profiles are vertically offset from each other. Speed ratios associated with the end ring speeds are listed in Table:4.3.

4.4.3   Determination of β from correlation measurement

Correlated LDV provides a nearly simultaneous measurement of two orthogonal velocity components. During setup of the instrument these components are aligned with the radial and azimuthal directions of the experiment. Solidbody rotation is used to measure any residual misalignment which is then removed from the data. Optical defects in the acrylic introduce a systematic error which is similar in magnitude to the correlations observed while operating in the `MRI` configuration. This error is removed by subtracting a normalized solidbody signal from that of the sheared profile:

$$\beta \equiv \frac{\langle v_r' v_\phi' \rangle}{q^2 \bar{v}_\phi^2} = \frac{1}{q^2} \left(\frac{\langle v_r' v_\phi' \rangle_p}{\bar{v}_{\phi,p}^2} - \frac{\langle v_r' v_\phi' \rangle_{sb}}{\bar{v}_{\phi,sb}^2} \right), \tag{4.8}$$

where $\langle v_r' v_\phi' \rangle$ is calculated via,

$$\langle v_r' v_\phi' \rangle = \frac{1}{N} \sum_i^N \left(v_{i,\phi} - \bar{v}_\phi \right) \left(v_{i,r} - \bar{v}_r \right).$$

The error on β is,

$$\begin{aligned}
\sigma_\beta^2 = &\left(\frac{1}{q^2 \bar{v}_{\phi,p}^2} \right)^2 \frac{\sigma_{\langle v_r' v_\phi' \rangle, p}^2}{N_p - 1} + \left(\frac{1}{q^2 \bar{v}_{\phi,sb}^2} \right)^2 \frac{\sigma_{\langle v_r' v_\phi' \rangle, sb}^2}{N_{sb} - 1} + \\
&\left(\frac{-2 \langle v_r' v_\phi' \rangle_p}{q^2 \bar{v}_{\phi,p}^3} \right)^2 \frac{\sigma_{\bar{v}_\phi, p}^2}{N_p - 1} + \left(\frac{-2 \langle v_r' v_\phi' \rangle_{sb}}{q^2 \bar{v}_{\phi,sb}^3} \right)^2 \frac{\sigma_{\bar{v}_\phi, sb}^2}{N_{sb} - 1} + \\
&\left(\frac{-2\beta}{q} \right)^2 \sigma_q^2
\end{aligned} \tag{4.9}$$

Subscripts p and sb refer to the profile being measured and the solidbody reference, respectively.

The dominant contribution to the error on β arises from the first two terms in Equation 4.9. This error is reduced by using large sample numbers, between 10^3 and 10^4. Overall sample number was limited by the data rate which varied from 10 Hz to < 1 Hz as oil entrained by a leaking seal would cause the fluid to cloud.

Cleaning cycles between experiments removed accumulated oil and restored consistent data rates. As published by Ji [Ji et al., 2006], no vertical variation in beta was observed.

In addition to the profiles listed in Table:4.1, three additional profiles were investigated. The speed ratios of these profiles are listed in Table:4.4. They were chosen to lie at or above the Rayleigh centrifugal stability limit. MS refers to an MRI configuration for which the end ring and inner cylinder speeds have been scaled up to the marginal stability line, $\partial l / \partial r = 0$. The CUS profiles are centrifugally unstable by the Rayleigh criterion. In configuration CUS a1, the speeds of the inner cylinder and the end rings have been scaled by the same factor from the MRI configuration to correspond to a profile expected to be 15% above the Rayleigh criterion. To make the flow even more unstable, the CUS a2 profile has had the outer end ring and outer cylinder speeds set to zero. Radial profiles of $\bar{v}_\phi$ for the CUS cases were not measured. Figure: 4.20 presents angular momentum and q profiles for two similar centrifugally unstable configurations which were measured. As in the case of CUS a1, when the outer cylinder is rotating, scaling the inner cylinder speed above the Rayleigh criterion does not automatically produce a saturated state of nearly constant angular momentum.

Table 4.4: Component speeds used to produce marginal and unstable flow profiles. Speeds are listed as a fraction of the Outer Cylinder speed, Ω_2. MS is marginally stable, CUS is unstable by the Rayleigh criterion.

Profile name	Ω_1	Ω_3	Ω_4	Ω_2
MRI	7.50	2.74	0.77	1.00
MS	8.27	3.02	0.83	1.00
CUS a1	9.43	3.43	0.94	1.00
CUS a2	9.43	3.43	0.00	0.00

The transport levels for linearly-stable profiles are plotted in Figure:4.17, the data used to produce the figure is summarized in Table:4.5. The optimized MRI and

`Keplerian` configurations for $Re > 10^6$ are not consistent with the proposed transport level. Averaging the results for the optimized configurations yields $\beta = 1.13 \pm 1.15 \times 10^{-6}$ and $\beta < 3.4 \times 10^{-6}$ at 2 standard deviations. Because negative values for β would indicate inward transport of angular momentum, 2 standard deviations yields 98% confidence. The slight improvement of the transport limit over the previously published result[Ji et al., 2006] is due to the use of the local measurement of q (see Section:4.4.2) and the new calibration for v_ϕ(see 3.5.1).

Also included in Fig:4.17 is a plot of $\beta_{visc} = \nu/\bar{r}^3|\partial\Omega/\partial r| = \nu/2b$ for water as the working fluid. This is provided to indicate where turbulence would be expected to dominate laminar viscosity in the the establishment of the equilibrium profile, in the absence of boundary layer effects. Radial transport associated with the `Split` configuration indicates that boundary layers cannot be assumed to be negligible. In fact, the data for the linearly-unstable profiles plotted in Figure:4.19 show that transport due to the influence of the boundaries for `Split` operation exceeds that for the unstable flow with rotating outer cylinder (`CUS` a1) by a factor of 20. Given this level of transport, the observations by Richard [Richard, 2001] are likely to be caused by the influence of the end rings extending throughout the fluid volume.

The source of the higher levels of transport associated with the glycerol runs are hinted at by the time-averaged radial velocities listed in Table:4.5. Of the `MRI` configurations, only for these low Reynolds number experiments is there a radial velocity which is distinguishable from zero. The velocity distributions for the glycerol runs are compared to a solidbody profile in Figure:4.18. For the 5% ($Re = 2 \times 10^4$) run, fluctuations are clearly present in the negative tail of the distribution which cause the non-zero value of $\bar{v}_r$. At double the Reynolds number, the fluctuations are more symmetric about the mean, the mean radial

velocity has fallen by a factor of two and β is already converging to the constant level seen above $Re \sim 10^5$. This convergence occurs an order of magnitude below the estimate for the critical Reynolds number given in Equation:4.2, in contradiction to the assertion that a transition exists in the intervening speed range.
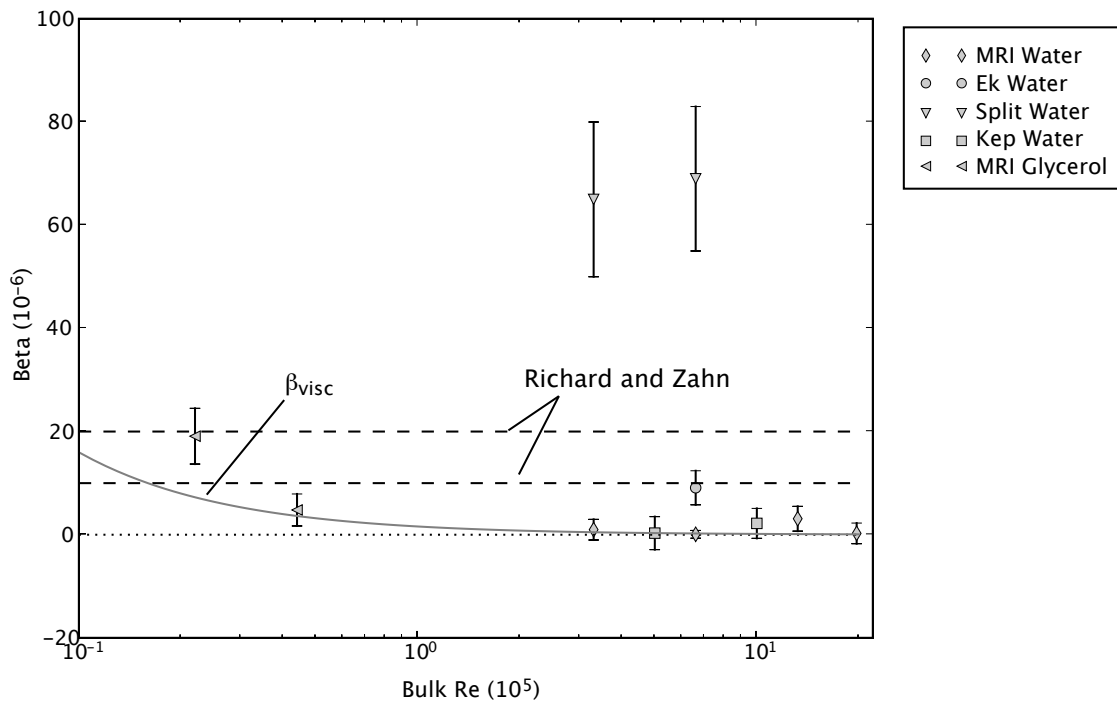
Figure 4.17: β for stable quasi-Keplerian profiles. The estimate of β made by Richard and Zahn [Richard and Zahn, 1999] is $1.5 \pm 0.5 \times 10^{-5}$. The dashed lines represent the one standard deviation confidence interval for this estimate. The solid line is $\beta_{visc} = \nu_{laminar}/\bar{r}^3 \, |\partial\Omega/\partial r|$. In terms of the Reynolds number, $Re = (\Omega_1 - \Omega_2)(r_2 - r_1)(r_2 + r_1)/2\nu$, $\beta_{visc} = (r_2^2 - r_1^2)^2/4Re(r_2 r_1)^2$.

Table 4.5: β values used for Figures:4.17,4.19. Suffix "G" on the profile name indicates use of glycerol-water mix as the working fluid.

Profile name	$Re/10^5$	$\beta(\times 10^{-6})$	N_p	N_{sb}	$\bar{v}_\phi(m/s)$	$\bar{v}_r(mm/s)$	q
MRI 5% G	0.22	19.1 ± 5.4	3999	2000	0.58100 ± 0.00028	-2.84 ± 0.35	2.00
MRI 10% G	0.44	4.8 ± 3.1	2000	2000	1.16000 ± 0.00051	-1.26 ± 0.67	2.00
MRI 5%	3.3	0.98 ± 2.00	4000	1000	0.60100 ± 0.00015	0.18 ± 0.17	2.03
MRI 10%	6.6	0.08 ± 0.75	7500	1500	1.24000 ± 0.00022	0.32 ± 0.44	2.05
MRI 20%	13.2	3.1 ± 2.4	552	1000	2.4200 ± 0.0017	0.2 ± 1.4	2.05
MRI 30%	19.7	2.6 ± 2.0	1000	707	3.400 ± 0.0016	0.9 ± 1.9	2.05
Keplerian 10%	5.0	0.31 ± 3.2	4000	4000	1.13000 ± 0.00032	-4.16 ± 0.27	1.20
Keplerian 20%	10.0	2.2 ± 2.9	4000	4000	2.3000 ± 0.00065	-9.86 ± 0.55	1.20
Ekman 10%	6.6	9.1 ± 3.3	1000	707	1.10000 ± 0.00071	1.70 ± 0.58	1.76
Split 5%	3.3	65 ± 15	500	707	0.8420 ± 0.0012	9.30 ± 1.60	2.05
Split 10%	6.6	69 ± 14	500	707	1.7700 ± 0.002	29.00 ± 3.60	2.05
MS	7.3	0.56 ± 0.96	5000	2000	1.26000 ± 0.00032	-0.16 ± 0.28	2.00
CUS a1	8.5	3.3 ± 1.6	2500	2000	1.49000 ± 0.00052	2.35 ± 0.38	2.00
CUS a2	9.5	890 ± 110	1000	2000	0.8370 ± 0.0026	-10.70 ± 3.60	2.00
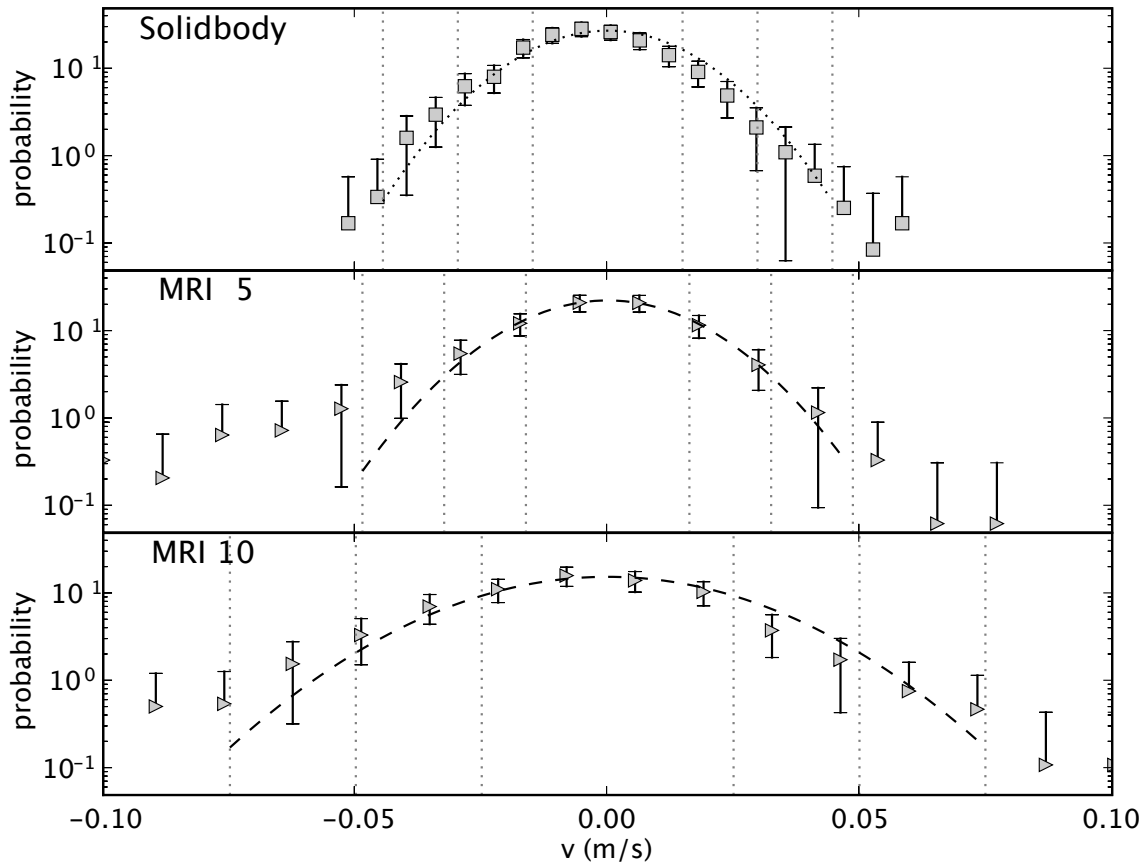
Figure 4.18: Probability distributions of radial velocities for operation in the MRI configuration with glycerol-water mix, $Re \sim 10^4$. Measurement is at $r = 180$ mm, $z = 50$ mm. Residual influence of the vertical boundaries is visible in the negative tails of the distributions. Dashed lines are Gaussian distributions fit to the data, vertical lines denote the 1st, 2nd and 3rd standard deviations of the distributions. Mean velocities of the MRI profiles have been subtracted, for 10% the mean velocity is $\bar{v}_r = -1.26 \pm 0.67$ mm, for 5%, $\bar{v}_r = -2.84 \pm 0.35$ mm
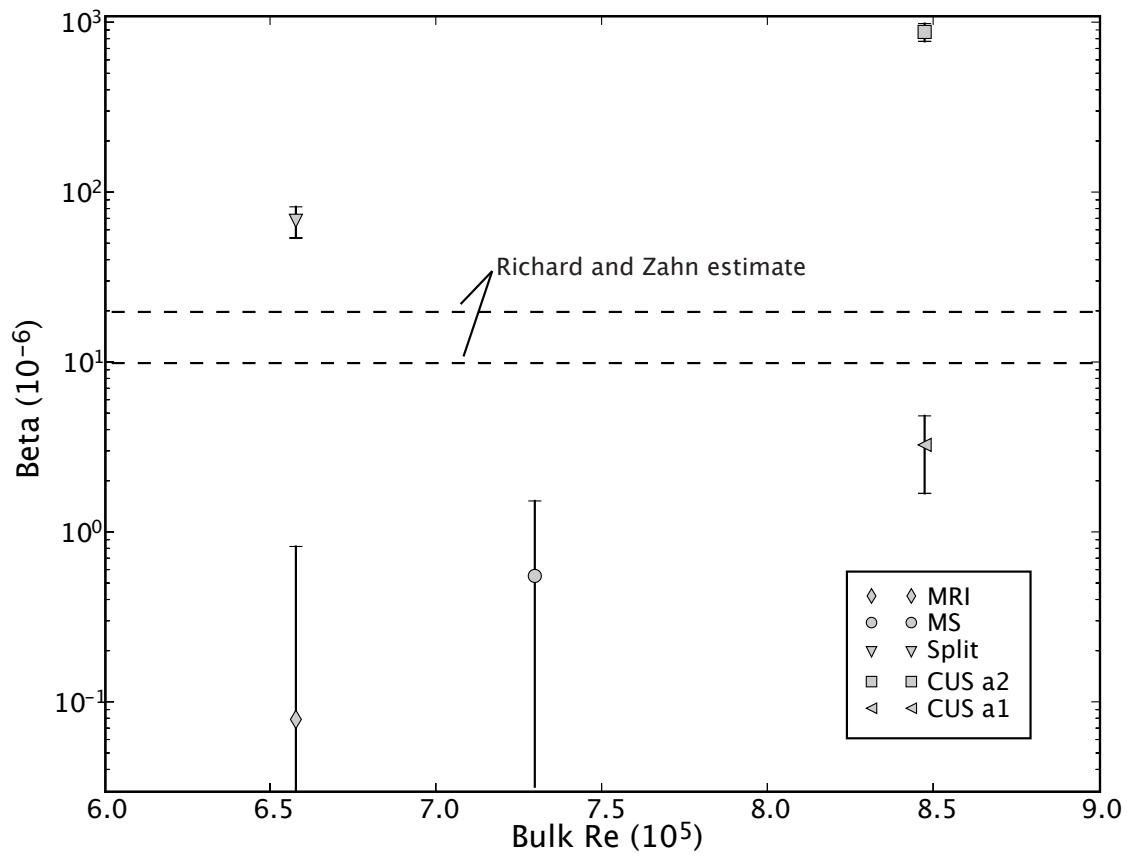
Figure 4.19: β for Rayleigh unstable profiles. For reference, stable `MRI` and `Split` 10% data are included.
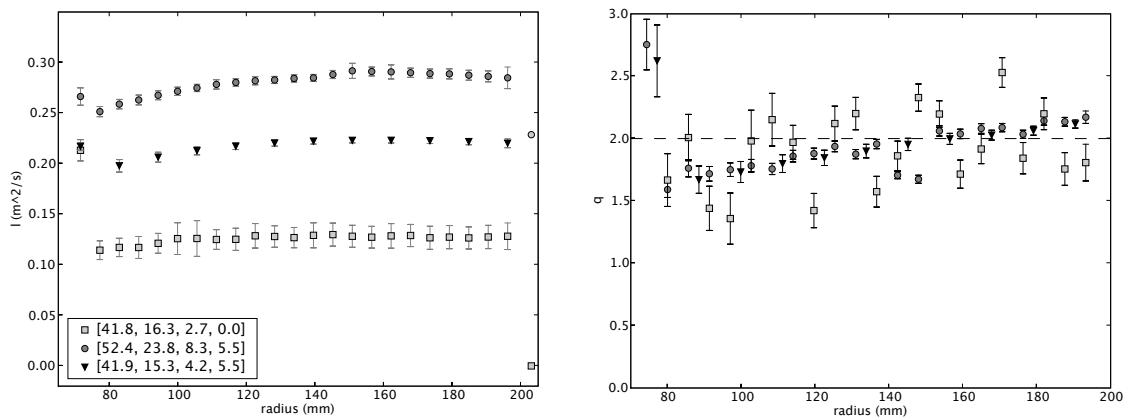
Figure 4.20: Specific angular momentum and local exponent of angular velocity for two centrifugally unstable profiles similar to the CUS cases for which β was measured. The MRI 10% case is also reproduced for reference in solid black. The unstable configurations were not named, so the profiles are labeled by the component speeds, in radians/second.

Chapter 5

Discussion and future work

5.1 Summary

We have constructed a small aspect ratio, wide gap circular-Couette experiment.
The apparatus is compatible with both water and GaInSn. Control of vertical
angular momentum transport through the end caps is achieved through two pairs
of nested, differentially rotating rings. A variety of mechanical difficulties have
been surmounted in order to achieve successful operation at $Re \sim 10^6$. The
primary challenges have been achieving proper sealing of the nested axles as they
extend out of the experiment and preventing premature wear of those seals. The
constraint that assembly of the apparatus proceed by sliding bearings along the
length of axles with poorly-controlled diametral tolerances has led to the most
successful innovation of the experiment: runout of the inner cylinder caused by
the excessive bearing clearances actively disrupts the Ekman circulation
generated at the end caps.

Operation in the `MRI` configuration produces an excellent approximation to the
ideal circular-Couette profile. The success of the approximation rests on the
ability to add and remove angular momentum through the end rings without

131

establishing large advection cells. The contribution of the boundaries to the flow is sketched in Figure: 5.1. The various regions of the flow are:

A Bulk flow in which β measurements indicate radial transport is not due to turbulence. Advection transport is ruled out by the measurement of zero average radial velocity (see Table: 4.5). Measurement of q demonstrates a negative radial gradient in angular momentum above the outer ring. By elimination of $\langle v_r v_\phi \rangle$ and $\langle v_r \rangle$ angular momentum must be removed through a Reynolds stress: $\langle v_z v_\phi \rangle$ (incompressibility rules out $\langle v_z \rangle \neq 0$).

B The axial variation of fluctuations in $\langle v_\phi \rangle$ are detectable only up to 40 mm into the fluid. The outer ring removes angular momentum from the bulk, whereas the inner ring adds it for $r > 120$ mm and removes it for $r_1 < r < 120$ mm. At 120 mm, the ring corotates with the bulk flow and fluctuations from the boundary penetrate vertically through the flow. Radial velocities (if present) within the boundary regions are indicated by the horizontal arrows. By the Taylor-Proudman theorem $\langle v_r \rangle \rightarrow 0$ as $z \rightarrow 40$ mm.

C From Figure: 4.10 the angular momentum at $r = 200$ mm is 8% below that of the outer cylinder at $r_2 = 203$ mm. A sharp gradient must exist between to transition the bulk flow to the cylinder wall. The gradient is centrifugally stable.

D In this region the eddies ejected by the inner ring-inner cylinder groove are detectable. A large-scale advective flow is prevented from forming by this ejection.

E The innermost point of the q profiles, see Figure: 4.14, indicates a centrifugally unstable region, due to the vertical presence of the inner ring, exists near the inner cylinder. The radial extent is unknown.

    F The profile reconnects to the ideal circular-Couette profile by $r = 90$ mm, see
       Figure 4.2.

Axially-oriented 2-component Laser Doppler Velocimetry has been used to
directly measure the $r - \phi$ component of the Reynolds stress. It appears that this
is the first application of LDV to measurement of the Reynolds stress in
circular-Couette flow.

5.2 Discussion of hydrodynamic results

5.2.1 Identification of control profile for MRI search

In the search for the MRI, we need to compare the behavior of unstable flows
against a quasi-Keplerian l profile which is either stable to the MRI or becomes
unstable only for higher magnetic field strengths or Re . This control profile will
provide information about the interaction of the magnetic field with any residual
boundary layer circulation. In the presence of a magnetic field, altered transport
through the end caps may allow the formation of Stewartson layers which can
then become Kelvin-Helmholtz unstable [Liu, 2007]. Alternately, the $q \approx 2$ regions
that are ubiquitous in the `MRI` and `Ekman` configurations may become
centrifugally unstable due to enhanced transport through the end caps. Early in
the design phase, we assumed that operation of the experiment in the `Ekman`
configuration would produce profiles similar to that obtained in the prototype
experiment (see panel B of Figure:4.5). The flattening of the angular velocity
profile over the outer half of the experiment was expected to provide the stability
to the MRI that we require. As shown in Figure:4.14, `Ekman` operation with the
current apparatus is not sufficiently different from the `MRI` configuration to be
assured that it remains stable when the `MRI` profile is unstable: in particular, $q \approx 2$
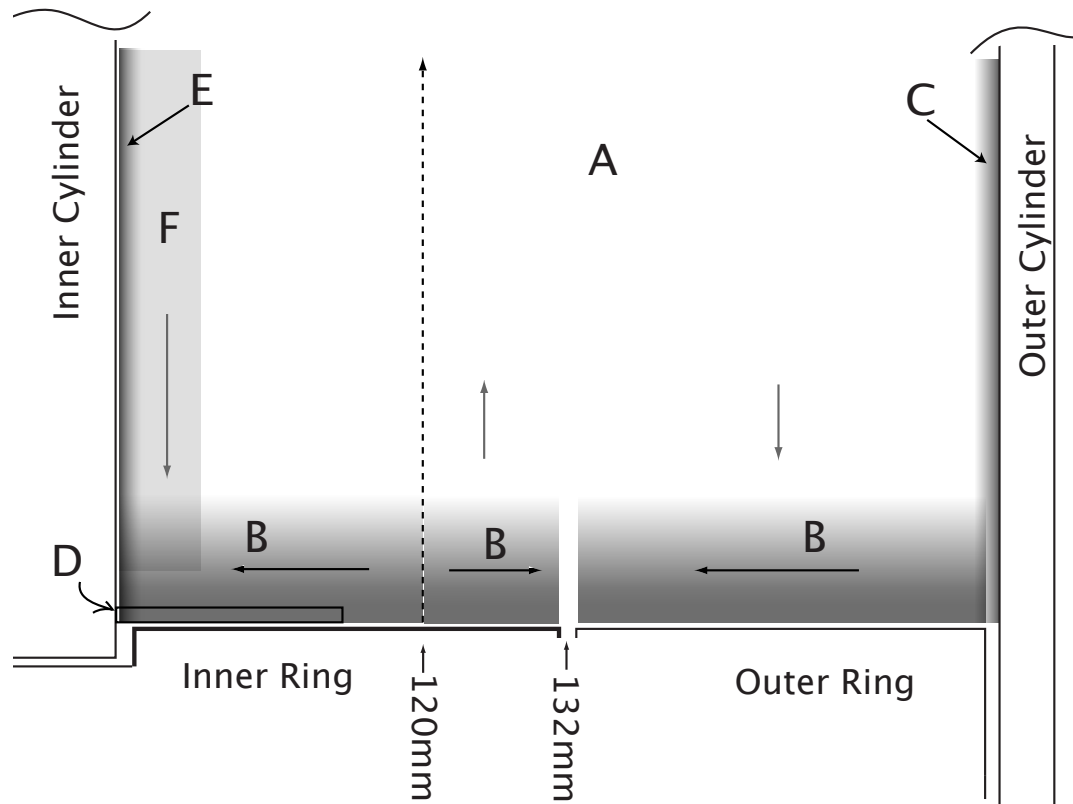
Figure 5.1: Regions of flow within cylinder gap `MRI` operation, the lower half of the apparatus is shown. A) bulk flow closely approximates the ideal circular-Couette profile. B) Fluctuations generated by the vertical boundaries extend approximately 40 mm into the flow. The sign of radial circulation within the "boundary zones" are indicated by the horizontal arrows. Vertical arrows indicate whether angular momentum is being added to or subtracted from the bulk flow. At a radius of 120 mm, the boundary corotates with the bulk flow. A vertical scan of fluctuations indicates that the effects of the boundary propagate through the vertical extent of the fluid. C) Centrifugally stable boundary which transitions from the bulk flow to the outer cylinder. D) Region in which eddies shed by the inner cylinder-inner ring gap are detectable. E) Measurement of q indicates a centrifugally-unstable region exists between $r_1 \leq 90$ mm. F) Region of relaminarization.

in the middle of the apparatus, see Figure: 4.14. The `Keplerian` profile satisfies the requirements of producing a quasi-Keplerian flow while $q < 2$ throughout the cylinder gap.

5.2.2 quasi-Keplerian turbulence

When operating in the `MRI` configuration we find no evidence enhanced angular momentum transport due to the $r - \phi$ component of the stress tensor even at $Re \sim 10^6$. This is in conflict with the observations of Richard[Richard, 2001] in which flow imaging demonstrated a turbulent transition inquasi-Keplerian flow near $Re \sim 10^4$. Richard attributes the turbulence to a subcritical transition but was unable to measure a hysteresis associated with the transition [*unpublished*]. Hysteresis is a defining characteristic of finite-amplitude instability, so its apparent absence casts doubt on the hypothesis. Wendt [Wendt, 1933] observed a similar turbulence for flow on the Rayleigh stability line. Both cylinders were rotating so no torque measurements were available.

Comparing `Split` operation in the Princeton MRI Experiment with the 2-D simulations we can identify a plausible source for the turbulence. In this configuration the Taylor-Proudman theorem applies in the vicinity of the inner cylinder, which causes the development of a fluid layer which is in nearly rigid rotation with the inner cylinder. This layer effectively reduces the gap width of the experiment, and will therefore effectively rotate the Rayleigh line in to the quasi-Keplerian regime.

In our apparatus, the peak of the layer occurs at a radius of $r_{peak} \approx 90$ mm, or normalized to the inner cylinder radius and gap width:

$$r_{peak} = \frac{90 \text{ mm} - r_1}{r_2 - r_1} \approx 0.15. \tag{5.1}$$

To make an estimate of the location of the peak in Richard's apparatus, we should

scale by the radius ratio, $2(r_2 - r_1)/(r_2 + r_1)$. Our radius ratio is 1, so scaling our peak location by Richard's radius ratio of 0.35, we should find the peak in Richard's apparatus at:

$$r_{peak} = (0.15)(0.35) \times (50 \text{ mm} - 35 \text{ mm}) + 35 \text{ mm} = 35.8 \text{ mm}. \qquad (5.2)$$

In cylinder speeds, the condition of marginal stability is $\Omega_1/\Omega_2 = r_2^2/r_1^2$. Changing the inner cylinder radius from 35 mm to 35.8 mm reduces the marginal stability ratio to 1.95 from 2.04.

A mean profile from Richard's quasi-Keplerian turbulent regime is plotted in the top panel of Figure: 5.2. To facilitate comparison with an optimized flow from our apparatus, the radius and velocity have been normalized. In this plot, the first point measured by Richard occurs at $r = 35.6 \text{ mm}$ indicating that his solid body layer is unresolved. However, fluctuations levels at that radius are higher than the other points in the flow. This could be explained by the presence of the fluctuations due to the an unstable layer within the LDV volume. The cylinder speeds Richard published for this figure apparently contain a typographical error: the speed ratio based on the caption is 2.2: exceeding greatly the Rayleigh criterion.

Plotted in the lower panel of Figure: 5.2 is a comparison of the local value of q.
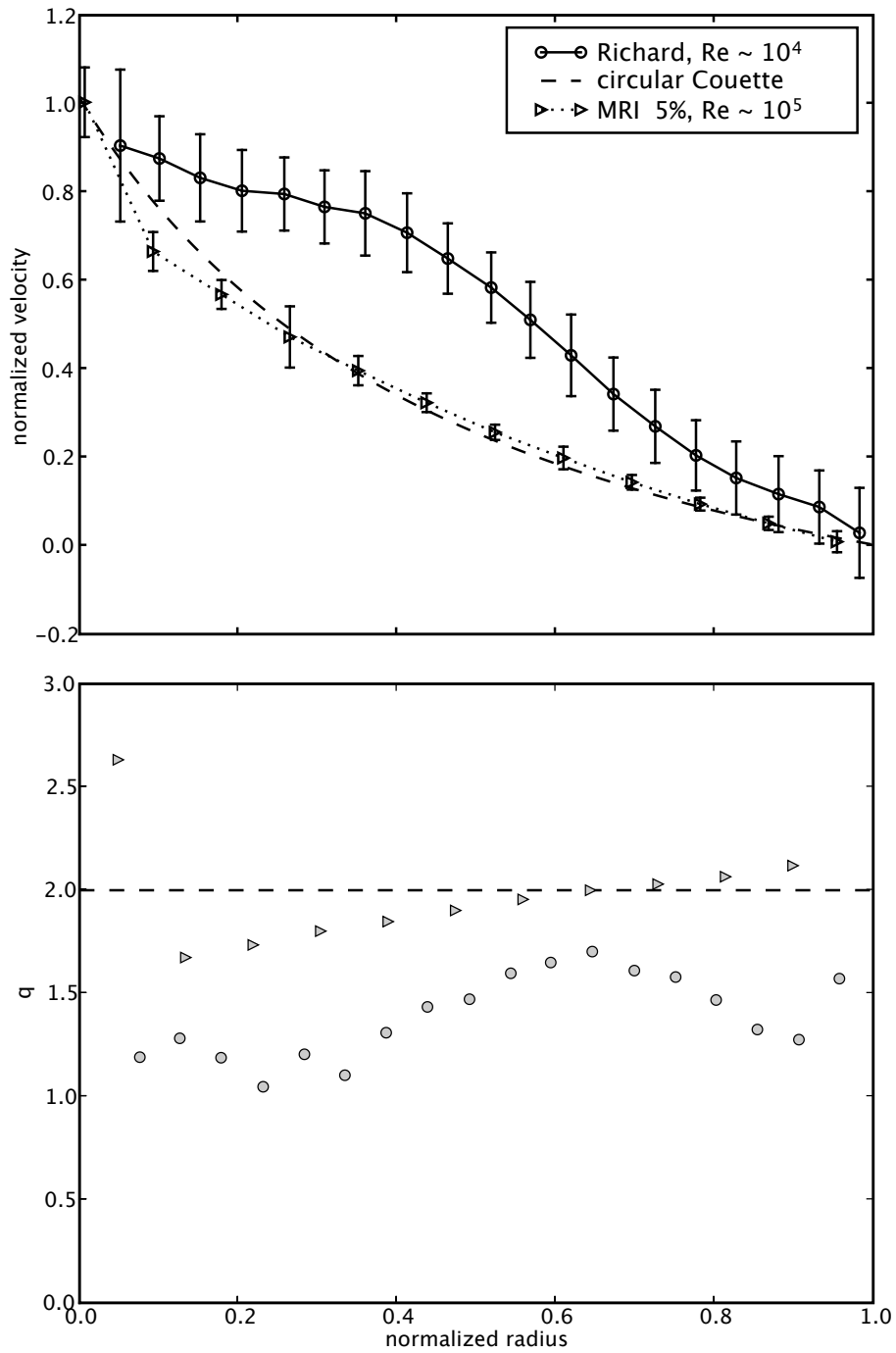
Figure 5.2: Comparison of quasi-Keplerian profiles produced by Richard and us.

5.2.3 Relevance to accretion disks

Reynolds stress measurements in the interval $2 \times 10^4 \leq Re \leq 2 \times 10^6$ do not indicate the presence of a turbulent transition. It is possible that the transition has occurred, but the associated level of transport is too small to be detected with the current technique. It is also possible that we have not reached the critical Reynolds number for transition in our apparatus.

If we rely on the observations of pipe flow we may make an extrapolation to astrophysical scales. In pipe flow the turbulent transition is sub-critical and occurs at a critical Reynolds number $Re^* \approx 2000$. Above Re^* the "friction factor" becomes independent of Reynolds number[Moody, 1944].Moody diagrams such as that reproduced in Figure: 5.3 illustrate this empirical knowledge.

The following argument is due to Lesur and Longaretti[Lesur and Longaretti, 2005]. At Re^* the laminar and turbulent viscosities must be equal, this implies the scaling:

$$\nu_T \sim \frac{1}{Re^*} \tag{5.3}$$

The qualitative idea behind this comes from considering a Kolmogorov energy spectrum for the turbulence. At the transition the inertial range is non-existent and the dissipation and stirring scales are equal. Increasing the Reynolds number causes the inertial range to expand while the dissipation scale remains fixed. Therefore, β in a circumstellar disk with $Re \sim 10^{12}$[Hersant et al., 2005] should be comparable to the value we measured at $Re \approx 2 \times 10^6$: $\beta < 3.4 \times 10^{-6}$.

Hueso and Guillot provide two β estimates for the protoplanetary disks DM Tau and GM Aur[Hueso and Guillot, 2005]. For DM Tau they estimate $2 \times 10^{-5} < \beta < 10^{-4}$. For GM Aur, $2 \times 10^{-6} < \beta < 8 \times 10^{-5}$. Our limit on β eliminates all but the lowest value from these ranges.
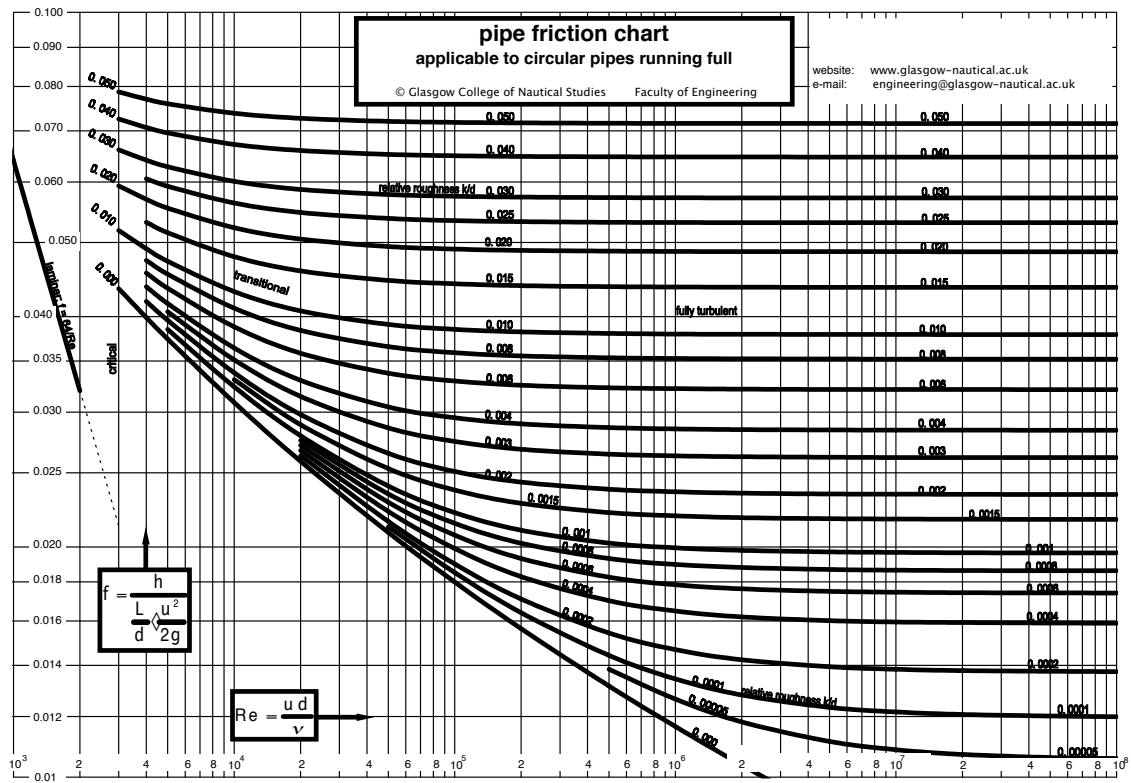
Figure 5.3: Moody Diagram illustrating independence of friction factor on Reynolds number for fully turbulent flow.

5.3   Future work

The surprising result that the `MRI` profile effectively eliminates advective transport from the bulk flow indicate directions for further inquiry. One question that is open is the maximum stable negative angular velocity gradient in the presence of vertical transport. To match the angular momentum of the outer cylinder, the gradient of angular momentum must change sign, thereby forming a shear layer above the outer ring. Is the decrease in angular momentum then dependent on the stability of that shear layer to a Rayleigh or Kelvin-Helmholtz instability?

Both the classical form of the Ekman layer as well as the Kageyama prescription are inadequate to describe the boundary layers of the PRINCETON MRI EXPERIMENT when operating in the `MRI` configuration. To see this, consider the Reynolds number calculated based on the vertical speed differential of the end ring and the bulk flow,

$$Re_{vert} = \frac{2\pi r^2}{\nu} \left| \Omega_{cC} - \Omega_{ring} \right| = \frac{2\pi r^2}{\nu} \left| a + br^2 - \Omega_{ring} \right|. \tag{5.4}$$

is plotted for 10% `Ekman` , `MRI` and `Split` configurations in Figure: 5.4. In the `MRI` configuration, the $Re_{vert} > 10^5$ everywhere except for an annulus near $120 \, \text{mm}$. Clearly it is not possible to describe the bulk flow as an infinitesimal departure from the boundary speed, as in the classical prescription. In the Kageyama prescription, small departures from the bulk flow are used but a viscous boundary layer must be attached to the end rings. A turbulent boundary layer model matching the end ring profile to the bulk flow should employed. Townsend [Townsend, 1980] derives such a model for a turbulent Ekman layer for a uniformly-rotating frame and states that the layer excites an evanescent vertically-propagating wave.

A Kalliroscope [Matisse and Gorman, 1984] image of the PRINCETON MRI

EXPERIMENT is presented in Figure: 5.5. Three 10% flows were imaged to gain some insight into the qualitative structure of the flow. Kalliroscope particles are anisotropic and so align with the local flow shear. In the centrifugally unstable case with the outer cylinder at rest the Kalliroscope shows no large-scale structure, which is consistent with fully-developed, isotropic turbulence. The `Ekman` case shows the influence of the boundary extending vertically throughout the flow, possibly consistent with a boundary layer penetrating deep in to the flow. In the `MRI` configuration the influence of the end caps is localized near the ends of the apparatus. This localization may be indicative of evanescent waves produced by the turbulent Ekman layer, as discussed by Townsend. More experimentation is needed to understand the detailed nature of the boundary layers.

The centrifugally unstable flows of Lewis and Swinney, and Lathrop feature positive angular momentum gradients within the bulk flow. Oscillations then appear to be ubiquitous features of these flows. Does the PRINCETON MRI EXPERIMENT contain similar wave motion in the centrifugally unstable regime? Does the unstable layer, region "E" in Figure: 5.1, excite waves in our quasi-Keplerian flows? The data rates of our LDV apparatus were too low to detect wave motion, in future work the data rates must be increased to allow spectral analysis. If these waves are present, how will they interact with an applied magnetic field? Lewis and Swinney's results show decreasing wave amplitude with a decreasing bulk angular momentum gradient (negative gradients are restricted to shear layers at the walls). When the MRI increases the angular momentum gradient will the radial magnetic field due to the MRI be masked by a corresponding amplification of the waves? The possibility of exciting subcritical hydrodynamic transition in the presence of a magnetic field too weak to produce the MRI needs to be explored.
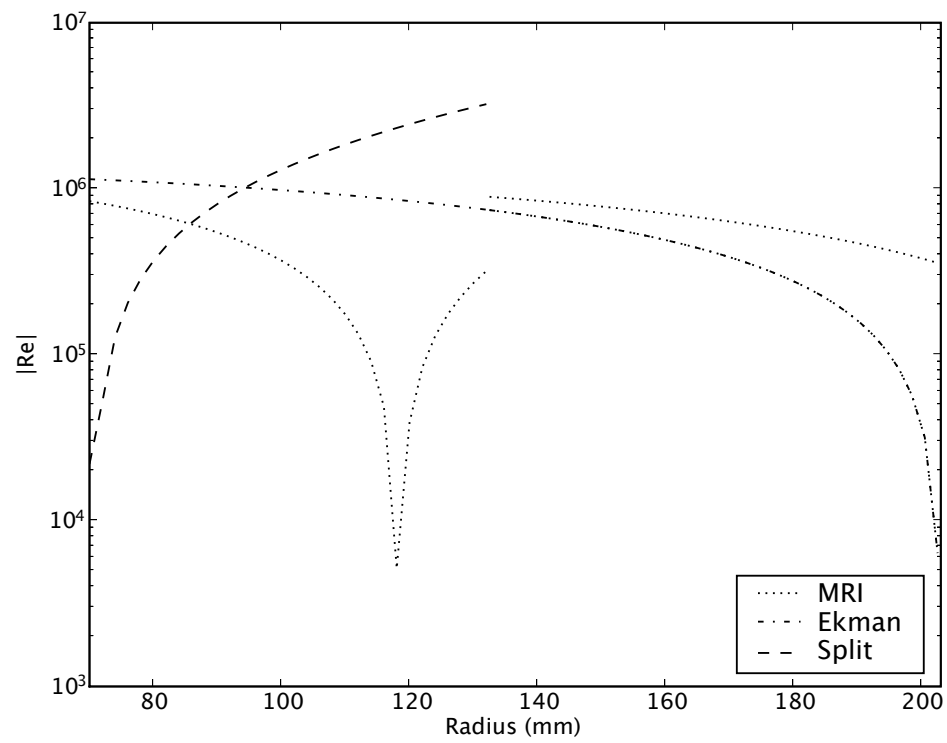
Figure 5.4: Re based on the vertical speed difference between the end rings and ideal circular-Couette flow.
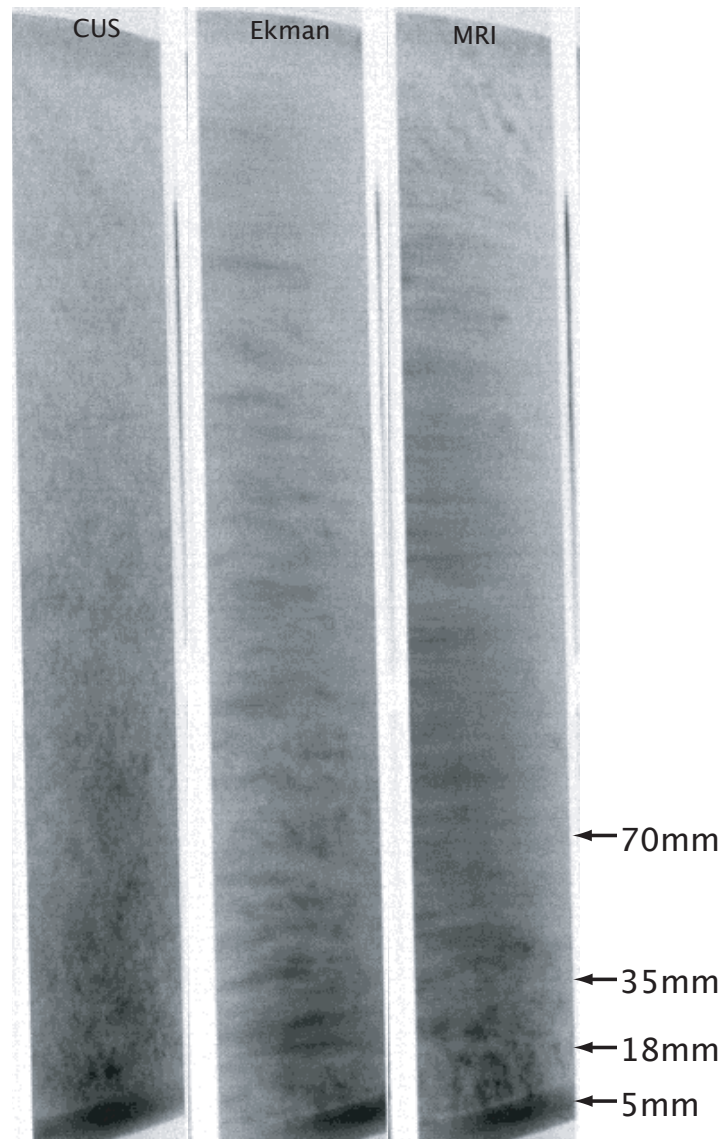
Figure 5.5: Kalliroscope images of three 10% configurations. The leftmost panel is centrifugally unstable, $\Omega_1 = 42 \; \mathrm{rad/s}, \Omega_2 = \Omega_3 = \Omega_4 = 0$. Middle panel is an `Ekman` configuration, and right panel is `MRI`. The apparatus is illuminated from below the outer ring by a flashlight, the color has been inverted to improve the contrast. The Kalliroscope flakes align with the local flow shear: ideal circular-Couette flow the flakes would horizontal banding as seen in the bulk of the `MRI` image. Dark patches near the boundaries in the `MRI` image show that the effects of the boundary are localized to within about 40 mm of the end rings, consistent with the fluctuation measurements of Figure: 4.12.

Finally, we have empirically determined that the quasi-Keplerian profiles most likely to be unstable to the MRI satisfy $\partial q/\partial r = 0$. The global eigenmode analysis [Goodman and Ji, 2002] should be repeated for this profile.

During the summer of 2007 the PRINCETON MRI EXPERIMENT was switched to liquid metal operation. During initial magnetized operation with quasi-Keplerian flows we found that the stainless steel plugs which mask the diagnostic ports of the outer cylinder had a residual magnetizability, probably due to cold working during machining. Also during this time, a seal began to fail and high speed operation was restricted to prevent GaInSn leaks. At this time, operation is suspended while these mechanical issues are addressed. When operation starts up again, the we will work to extend the maximum operational Reynolds number up to the full design speed.

Appendix A

LDV Shot Information, Error Analysis

A.1 Calibrations for Dantec radial measurements

Table A.1: Solidbody calibration shots

Shot	Ω_1	Ω_3	Ω_4	Ω_2	Height (mm)
467	50	50	50	50	11, 141
486	53	53	53	53	76
487	53	53	53	53	76
512	50	50	50	50	76

Table A.2: Dantec Run 2 calibration parameters

y_2 (mm)	y_1 (mm)	intercept (mm)	slope (m/s/mm)
121.30 ± 0.25	4.16 ± 0.16	0.121 ± 0.012	0.004840 ± 0.000045
121.30 ± 0.25	4.16 ± 0.16	$0.114 \pm ?$	$0.004840 \pm ?$

Table A.3: Dantec Run 3 calibration parameters

y_2 (mm)	y_1 (mm)	intercept (mm)	slope (m/s/mm)
-212.20 ± 0.25	-94.03 ± 0.50	0.1406 ± 0.0051	0.005035 ± 0.000084

A.2 Dantec measurement volume

TableA.4 lists the length measurement volume of the Dantec LDV. The laser power is substantially reduced over the original factory value, which rules out using the factory specification. Calculation of c_0 from velocity gradient: For solidbody rotation, the velocity gradient is $\delta v/\delta r = \Omega$. If the standard deviation of the velocity measurement is attributed to the extension of the measurement volume along the velocity gradient, then

$$c_{0,i} = \frac{\sigma_v}{\delta v/\delta r},$$

$$c_0 = \frac{1}{N}\sum_i n_i c_{0,i}. \tag{A.1}$$

Calculation from ratio of length to width: From the Dantec specs, $c_0 = 2.5mm$, $b_0 = 0.119mm$ corresponding to the FWHM along the two directions. From the product of burst transit time τ_{TT}, with velocity an average b_0 at various radii, r_i, can be made:

$$b_0(r_i) = \tau_{TT,i} v_i,$$

and the count-weighted sum is:

$$b_0 = \frac{1}{N}\sum_i b_0(r_i) n_i,$$

where n_i is the number of bursts recorded at radius r_i and $N = \sum n_i$

Table A.4: Length of Dantec Measurement Volume, c_0, run 2.

Source	c_0	Note
Dantec spec.	$2.5mm$	FWHM, air
Dantec spec.	$1.9mm$	water, calculated
Velocity gradient	$2.7mm$	weighted mean
Inner Cyl scan:	$1.7mm$	FWHM, midplane
Length to width ratio:	$1.7mm$	transit time

Table A.5: Length of Dantec Measurement Volume, c_0, run 3.

Source	c_0	Note
Dantec spec.	$2.5mm$	FWHM, air
Dantec spec.	$1.9mm$	water, calculated
Inner Cyl scan:	$1.2mm$	FWHM, midplane
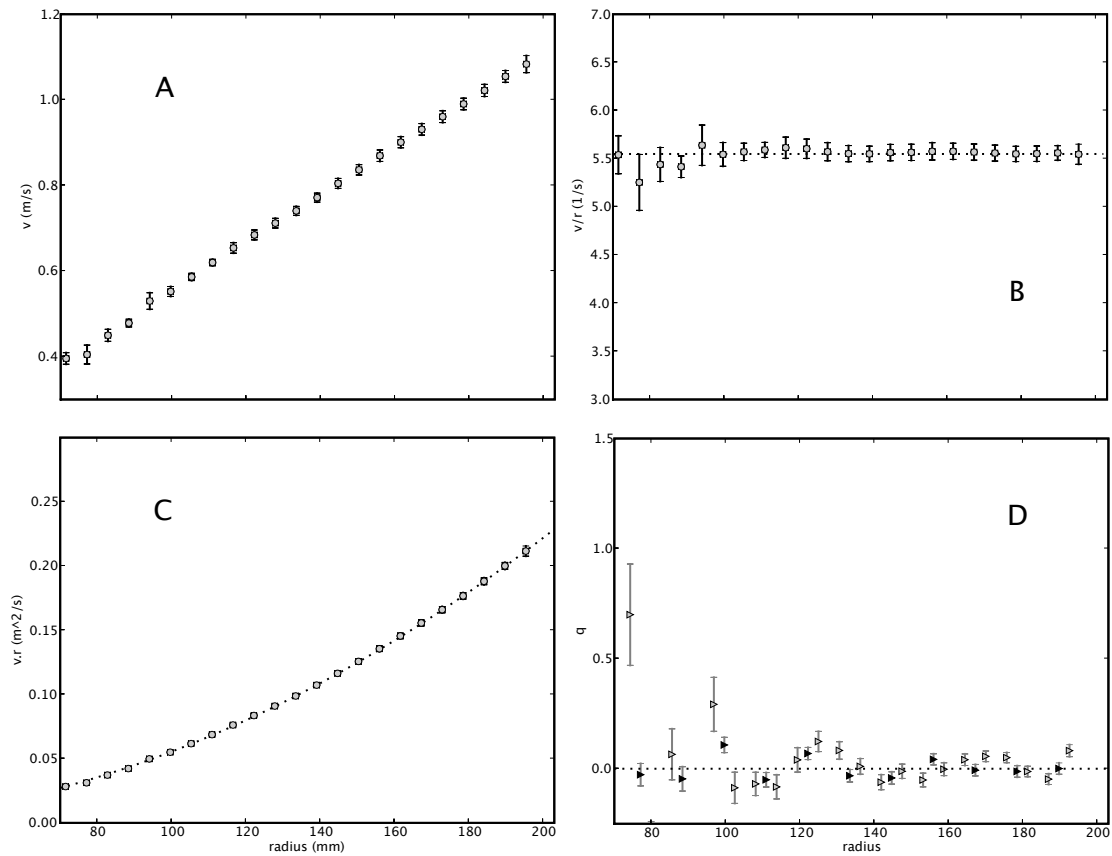
Figure A.1: A. Velocity, B. angular velocity, C. specific angular momentum, D. shear profile, 'q'.

A.3   Flow profile for solidbody rotation

Flow profiles measured at $z = 76mm$ during the October 2005 Dantec run are plotted in Fig:A.1.

Appendix B

Bessel filter amplifier schematic

Figure B.1: Amplifier-filter used to amplify the the pick-up coil signals before transmission to the PC.

Bibliography

Maxim ic. URL `http://www.maxim-ic.com`.

H. E. Albrecht, M. Borys, N. Damaschke, and C. Tropea. *Laser Doppler and Phaser Doppler Measurement Techniques*. Springer-Verlag, 2003.

CD Andereck, SS Liu, and HL Swinney. Flow regimes in a circular Couette system with independently rotating cylinders. *Journal of Fluid Mechanics*, 164: 155–183, 1986.

S. A. Balbus. Enhanced angular momentum transport in accretion disks. *ANNUAL REVIEW OF ASTRONOMY AND ASTROPHYSICS*, 41:555–597, 2003. ISSN 0066-4146.

Steven A. Balbus and John F. Hawley. A powerful local shear instability in weakly magnetized disks. i. linear analysis. *Astrophysical Journal*, 376:214–222, 1991.

Steven A. Balbus and John F. Hawley. Instability, turbulence, and enhanced transport in accretion disks. *Reviews of Modern Physics*, 70, 1998.

H.F. Beckley. *Measurements of Annular Couette Flow Stability at the Fluid Reynolds Number Re=4.4×10^6: The Fluid Dynamic Precursor to a Liquid Sodium $\alpha\omega$ Dynamo*. PhD thesis, New Mexico Institute of Mining Technology, 2002.

M. J. Burin, H. Ji, E. Schartman, R. Cutler, P. Heitzenroeder, W. Liu, L. Morris, and S. Raftopolous. Reduction of ekman circulation within taylor-couette flow. *EXPERIMENTS IN FLUIDS*, 40(6):962–966, Jun 2006. ISSN 0723-4864.

S. Chandrasekhar. *Proceedings of the Royal Society of London, A.*, 216(293), 1953.

S. Chandrasekhar. The stability of non-dissipative couette flow in hydromagnetics. *Proceedings of the National Academy of Sciences of the United States of America*, 46(2):253–257, 1960.

D. Coles. Transition in circular Couette flow. *Journal of Fluid Mechanics Digital Archive*, 21(03):385–425, 2006.

MM Couette. Sur un nouvel appareil pour l'étude du frottement des fluides. *Comptes Rendus*, 107:388–390, 1888.

M. A. Dominguez-Lerma, G. Ahlers, and D. S. Cannell. Effects of 'kalliroscope' flow visualization particles on rotating couette-taylor flow. *Phys. Fluids*, 28 (1204), 1985.

R. J. Donnelly and M. Ozima. Hydromagnetic stability of flow between rotating cylinders. *Phys. Rev. Lett.*, 4(10):497–498, May 1960. doi: 10.1103/PhysRevLett.4.497.

R. J. Donnelly and M. Ozima. Experiments on the stability of flow between rotating cylinders in the presence of a magnetic field. *Proceedings of the Royal Society of London, A.*, 266(1325):272–286, 1962.

B. Eckhardt, T. M. Schneider, B. Hof, and J. Westerweel. Turbulence transition in pipe flow. *ANNUAL REVIEW OF FLUID MECHANICS*, 39:447–468, 2007. ISSN 0066-4189.

J.P. Freidberg. *Ideal magnetohydrodynamics*. Plenum Press New York, 1987.

W. G. Frühand Read P. L. Experiments on a barotropic rotating shear layer. part i. instability and steady vortices. *Journal of Fluid Mechanics*, 383:143–173, 1999.

J. Goodman and H. T. Ji. Magnetorotational instability of dissipative couette flow. *JOURNAL OF FLUID MECHANICS*, 462:365–382, Jul 2002. ISSN 0022-1120.

HP Greenspan. *THE THEORY OF ROTATING FLUIDS*. Cambridge University Press, 1968.

E. Guyon, J.P. Hulin, L. Petit, and C.D. Mitescu. *Physical Hydrodynamics*. Oxford University Press, 2001.

F. Hersant, B. Dubrulle, and J.-M. Huré. Turbulence in circumstellar disks. *Astronomy and Astrophysics*, 429:531–542, 2005.

R. Hide and C. W. Titman. Detached shear layers in a rotating fluid. *Journal of Fluid Mechanics*, 29:39–60, 1967.

R. Hollerbach. Instabilities of the Stewartson layer Part 1. The dependence on the sign of Ro. *Journal of Fluid Mechanics*, 492:289–302, 2003.

R. Hollerbach and G. Rüdiger. *Phys. Rev. Lett.*, 95:124501, 2005.

Rainer Hollerbach and Alexandre Fournier. End-effects in rapidly rotating cylindrical taylor-couette flow. *AIP CONF PROC*, 733:114, 2004.

R. Hueso and T. Guillot. Evolution of protoplanetary disks: constraints from dm tauri and gm aurigae. *Astronomy and Astrophysics*, 442(2):703–725, Nov 2005. ISSN 0004-6361.

H. Ji, J. Goodman, A. Kageyama, M. J. Burin, E. Schartman, and W. Liu. Magnetorotational instability in a short couette flow of liquid gallium. *MHD Couette Flows: Experiments and Models, Proceedings of the conference held 29 February-2 March 2004 in Acitrezza, Catania (Italy). Edited by Robert Rosner, Günther Rüdiger, and Alfio Bonanno. New York: American Institute of Physics*, 733: 21–34, 2004.

H. T. Ji, M. Burin, E. Schartman, and J. Goodman. Hydrodynamic turbulence cannot transport angular momentum effectively in astrophysical disks. *NATURE*, 444(7117):343–346, Nov 2006. ISSN 0028-0836.

Hantao Ji, Jeremy Goodman, and Akira Kageyama. Magnetorotational instability in a rotating liquid metal annulus. *Monthly Notices of the Royal Astronomical Society*, 325(2):L1–L5, 2001. doi: 10.1046/j.1365-8711.2001.04647.x.

A. Kageyama, H. T. Ji, J. Goodman, F. Chen, and E. Shoshan. Numerical and experimental investigation of circulation in short cylinders. *JOURNAL OF THE PHYSICAL SOCIETY OF JAPAN*, 73(9):2424–2437, Sep 2004. ISSN 0031-9015.

VP Lakhin and EP Velikhov. Instabilities of highly-resistive rotating liquids in helical magnetic fields. *Physics Letters A*, 369(1-2):98–106, 2007.

D. P. Lathrop, J. Fineberg, and H. L. Swinney. *Phys. Rev. A*, 46(6390), 1992.

G. Lesur and P.-Y. Longaretti. on the relevance of subcritical hydrodynamic turbulence to accretion disk transport. *Astronomy and Astrophysics*, 444:25–44, 2005.

G.S. Lewis and H.L. Swinney. Velocity structure functions, scaling, and transitions in high-Reynolds-number Couette-Taylor flow. *Physical Review E*, 59 (5):5457–5467, 1999.

D.N.C. Lin and J.C.B. Papaloizou. Theory of accretion disks ii: application to observed systems. *Annual Review of Astronomy and Astrophysics*, 34:703–747, 1996.

W. Liu, J. Goodman, I. Herron, and H. Ji. Helical magnetorotational instability in magnetized Taylor-Couette flow. *Phys Rev E Stat Nonlin Soft Matter Phys*, 74(5 Pt 2):056302, 2006a.

W. Liu, J. Goodman, and H. T. Ji. Simulations of magnetorotational instability in a magnetized couette flow. *ASTROPHYSICAL JOURNAL*, 643(1):306–317, May 2006b. ISSN 0004-637X.

Wei Liu. *Axisymmetric Numerical and Analytical Studies of the Magnetorotational Instability in a Magnetized Taylor-Couette Flow*. PhD thesis, Princeton University, 2007.

P.Y. Longaretti. On the Phenomenology of Hydrodynamic Shear Turbulence. *The Astrophysical Journal*, 576:587–598, 2002.

D. Lynden-Bell and JE Pringle. The evolution of viscous discs and the origin of the nebular variables. *Mon. Not. R. Astron. Soc*, 168(3), 1974.

A. Mallock. Determination of the Viscosity of Water. *Proceedings of the Royal Society of London*, 45:126–132, 1888.

P. Matisse and M. Gorman. Nuetrally bouyant anisotropic particles for flow visualization. *Physics of Fluids, Letters*, 27(4), 1984.

L.F. Moody. Friction factors for pipe flow. *Trans. ASME*, 66(8):671–677, 1944.

N. B. Morley, J. Burris, L. C. Cadwallader, and M. D. Nornberg. Galinstan usage in the research laboratory. *Submitted*, 2007.

E. R. Niblett. *Canadian Journal of Physics*, 36(1509), 1958.

A.V. Obabko, F. Cattaneo, and P. Fischer. Magneto-rotational instability and turbulent angular momentum transport. APS, 48th Annual Meeting of the Division of Plasma Physics, November 2006.

Arnaud Prigent and Olivier Dauchot. Visualization of a taylor–couette flow avoiding parasitic reflection. *Phys. Fluids*, 12:2688, 2000.

Lord Rayleigh. On the dynamics of rotating fluid. *Proc. R. Soc. Lond. A.*, 93: 148–154, 1916.

D. Richard and J-P. Zahn. Turbulence in differentially rotating flows: what can be learned from the couette-taylor experiment. *Astronomy and Astrophysics*, 347: 734–738, 1999.

Denis Richard. *Instabilités Hydrodynamiques dans les Ecoulements en Rotation Différentielle*. PhD thesis, Université Paris 7, 2001.

CB Rogers. The effect of small particles on fluid turbulence in a flat-plate, turbulent boundary layer in air. *Physics of Fluids A Fluid Dynamics*, 3(5):928, 1991.

T. Sano and S. M. Miyama. Magnetorotational instability in protoplanetary disks. i. on the global stability of weakly ionized disks with ohmic dissipation. *ASTROPHYSICAL JOURNAL*, 515:776–786, 1999.

F. Schultz-Grunow. Zur Stabilitat der Couette-Stromung. *Z. Angew. Math. Mech*, 39:101–110, 1959.

N.I. Shakura and R.A. Sunyaev. Black holes in binary systems. observational appearance. *Astron. Astrophys.*, 24:337–355, 1973.

D.R. Sisan, N. Mujica, W.A. Tillotson, Y.M. Huang, W. Dorland, A.B. Hassam, T.M. Antonsen, and D.P. Lathrop. Experimental Observation and Characterization of the Magnetorotational Instability. *Physical Review Letters*, 93(11):114502, 2004.

GP Smith and AA Townsend. Turbulent Couette flow between concentric cylinders at large Taylor numbers. *Journal of Fluid Mechanics Digital Archive*, 123: 187–217, 2006.

C. G. Speziale. Analytical methods for the development of reynolds-stress closures in turbulence. *ANNUAL REVIEW OF FLUID MECHANICS*, 23: 107–157, 1991. ISSN 0066-4189.

F. Stefani, T. Gundrum, G. Gerbeth, and R. Rosner. *Phys. Rev. Lett.*, 97:184502, 2006.

K Stewartson. On almost rigid rotations. *JOURNAL OF FLUID MECHANICS*, 3 (17), 1957.

R. Tagg. The Couette–Taylor problem. *Nonlinear Sci. Today*, 4(3):1–25, 1994.

G.I. Taylor. Stability of a viscous liquid contained between two rotating cylinders. *Philosophical Transactions of the Royal Society of London, A*, 223:289–343, 1923.

GI Taylor. Fluid Friction between Rotating Cylinders. I. Torque Measurements. *Proceedings of the Royal Society of London. Series A, Mathematical and Physical Sciences*, 157(892):546–564, 1936.

AAR Townsend. *The Structure of Turbulent Shear Flow*. Cambridge University Press, 1980.

E. P. Velikhov. Stability of an ideally conducting liquid flowing between cylinders rotating in a magnetic field. *Sov. Phys. JETP*, 36(9):995–998, 1959.

EP Velikhov, AA Ivanov, VP Lakhin, and KS Serebrennikov. Magneto-rotational instability in differentially rotating liquid metals. *Physics Letters A*, 356(4-5): 357–365, 2006.

F. Wendt. Turbulente strömungen zwischen zwei rotierenden konaxialen zylindren. *Ing. Arch.*, 4:577–595, 1933.

YB Zeldovich. On the Friction of Fluids Between Rotating Cylinders. *Proceedings of the Royal Society of London. Series A, Mathematical and Physical Sciences*, 374 (1758):299–312, 1981.